

**Active Structural Control of Single and Multi-Span
Beam Structures Subjected to Transient Loads**

**A thesis submitted in partial fulfilment of the requirements of Liverpool
John Moores University for the degree of Doctor of Philosophy**

by

Lukas Sievert

March 2022

Declaration

Hereby I declare that no portion of the work referred to in the thesis has been submitted in support of an application for another degree or qualification of this or any other university or other institute of learning.

Acknowledgements

I deeply acknowledge the financial support of the Faculty of Engineering and Technology at Liverpool John Moores University. Without that, this research would not have been possible. This includes the PhD scholarship as well as the cost of the highly advanced technical equipment and the costs of two inspiring conferences.

I wish to express my sincere gratitude to my Director of Studies Dr Dan Stancioiu. With his profound knowledge and ideas he guided me into the fascinating fields of vibration and control and always pushed me and this research further towards its boundaries.

I owe a vote of thanks to my second supervisor Dr Christian Matthews. It was only through him that I got the opportunity to take advantage of the scholarship at Liverpool John Moores University.

I would like to thank Paul Wright and his team in the workshop for the technical support and the unproblematic supply of equipment and access to machinery and tools. Further, I am grateful for the support I received through Steve Gotts and his team, who supported me with electrical equipment during the experimental work.

Finally, I wish to dedicate this thesis to my parents and family, who supported me with their love and care. I am grateful for the love and support of Wanda who always believed in me during this intense time.

Abstract

This study directly addresses the problem of active control of beam structures under the action of moving masses. In this regard, experimental implementations of the particular active control solutions are still rarely seen in the literature. The main objective is to experimentally implement and validate active control solutions for two small-scale test stands with the aim to reduce the structural deflection.

The first supporting structure is modelled as an Euler–Bernoulli simply supported beam, acted upon by moving masses of different weights and velocities. The experimental implementation of the proposed optimal controller poses a particular set of challenges as compared with numerical solutions. Specifically, it can include errors due to discretization and the states cannot be directly measured. The resulting limitations of classical optimal observer techniques are stated and consequently the states are estimated by a method utilizing the mode shapes. It is shown both numerically and experimentally that using electromagnetic actuation, a reduced order controller designed using a time-varying algorithm, provides a reduction of the maximum deflection of up to 38% as compared with the uncontrolled structure. Herein an augmented system model is utilised, which includes the moving mass in the system equation. The controller performance and robustness were tested against a representative set of possible moving load parameters. In consequence of the variations in moving mass weight and speed, the controller gain requires a supplementary adaptation. A simple algorithm that schedules the gain as a function of the weight and speed of the moving mass can achieve both a good performance and an adjustment of the control effort to the specific design requirements.

In the second part of this study cubic and linear displacement feedback control approaches are studied experimentally for a simply supported beam as well as for the two-span continuous beam. The two-span beam structure is modelled by approximating the support by spring damper elements of high stiffness and damping coefficient. Piezoelectric macro fibre composites serve as actuators. The control methods are, compared to the previous approach, more straightforward to implement and can handle a stream of moving masses. However, optimality and stability cannot be guaranteed and have to be validated experimentally. The linear displacement feedback shows better performance for low weights of the moving masses whereas the cubic displacement feedback achieves higher deflection reduction for higher weights.

In the last part, constrained model predictive control is studied numerically for both of the structures. This is currently the only control approach which can take into account saturation limits explicitly by quadratic programming. In this way, better performance is achieved for both test structures as compared to the displacement feedback control approaches.

Table of Contents

Declaration	II
Acknowledgements	III
Abstract	IV
List of Figures	IX
List of Tables	XVII
List of Symbols	XVIII
List of Abbreviations	XXIV
1 Introduction	1
1.1 Aims and objectives	2
1.2 Literature Review	2
1.3 Knowledge gap	12
1.4 Methodology and Outline of the Thesis	12
2 The Moving Mass-Structure Interaction Models	15
2.1 The Transverse Vibration of Single and Multi-Span Beams Subjected to Moving Masses	16
2.1.1 Approximation of Mode Shapes of Continuous Two-Span Beams	21
2.1.2 Experimental Validation of the Simply Supported Beam under Moving Loads	26
2.1.3 Experimental Validation of the Two-Span Continuous Moving Load Structure	28
2.2 The Simply Supported Beam Controlled by an Electrodynamic Shaker	33
2.2.1 Numerical Model of a Simply Supported Beam Controlled by an Electrodynamic Shaker	33
2.2.2 Numerical Study of the Beam-Shaker-Moving-Mass Test Structure	36
2.2.3 Simplified Model of the Simply Supported Beam Structure Controlled by an Electrodynamic Shaker	39
2.2.4 Experimental Validation of the Beam-Shaker Structure	41
	VI

2.3	Further Numerical Validation of the Moving Mass Model	43
2.4	Modelling of the Piezoelectric Actuator-Beam Structure	48
2.4.1	The Mathematical Model of the Piezoelectric Beam System	49
2.4.2	Experimental Validation of the Piezo Beam Systems	53
2.5	Concluding Remarks.....	58
3	Optimal Control Approaches Dedicated to the Moving Mass Problem	59
3.1	The Finite Time Optimal Control.....	59
3.2	Step by Step Calculation of the Riccati Equation	61
4	The State Estimation	63
4.1	Optimal Full-State Estimation	63
4.2	State Estimation by Mode Shapes	65
5	Case Study 1: Active Vibration Control of a Simply Supported Beam Acted upon by Moving Masses	66
5.1	Experimental and Numerical Validation of the State Estimation Methods.....	66
5.2	Experimental Results for the Optimal Control Implementation.....	75
5.3	Experimental Results for Variable Control Gain	86
5.4	Experimental Validation of the Optimal Control by an Augmented System	90
5.5	Concluding Remarks.....	94
6	Case Study 2: Proportional Displacement Feedback Control	95
6.1	Simply Supported Beam Controlled by a Piezoelectric Actuator.....	96
6.2	Two-Span Continuous Beam Controlled by Piezoelectric Actuators	102
7	Model Predictive Control for Moving Load Structures	107
7.1	The Control Algorithm.....	107
7.2	Discrete Time Model Predictive Control with Constraints.....	109
7.3	Numerical Examples of the Model Predictive Control for the Beam Structures Controlled by Piezoelectric Actuators.....	112
7.3.1	Numerical Experiment on the Simply Supported Beam	114
7.3.2	Numerical Experiment on the Two-Span Continuous Beam Structure	117

7.4	Concluding Remarks.....	121
8	Conclusions and Future Work	123
9	Appendix	129
	List of References	132

List of Figures

Figure 1.1.	Methodology applied in the project.	13
Figure 2.1.	Model of a simply supported beam subjected to a moving mass m travelling with constant speed v .	16
Figure 2.2.	A stream of masses moving on a two-span beam, intermediate mid-span support modelled as a spring-damper element.	20
Figure 2.3.	Simply supported beam with equal span length l and one centered spring support.	24
Figure 2.4.	Comparison of the first eight modes of the two-span continuous beam approximated (blue continuous) and calculated analytical (red dashed).	25
Figure 2.5.	Experimental set-up, aluminium polymer beam subjected to a moving mass.	26
Figure 2.6.	Schematic drawing of the whole experimental set-up of the simply supported beam actuated by an electrodynamic shaker	27
Figure 2.7.	Time history of the deflections at sensor locations $xs1 - xs3$ of the numerical model (blue continuous) and the experimentally obtained data (red dashed).	28
Figure 2.8.	Experimental set-up of the two-span beam with two piezoelectric actuators.	29
Figure 2.9.	Schematic drawing of the experimental set-up of the two-span continuous beam	29
Figure 2.10.	Time history of the deflection data $wxs2$ $m = 0.261$ kg moving along the two-span beam, comparison of the experimental results (blue continuous), numerical 12 modes (red dashed), numerical 8 modes (black dash dotted) and numerical 6 modes (blue dotted).	30
Figure 2.11.	Time history of the deflections at the sensor locations $xs1 - xs3$ of the numerical data (red dashed) and the experimental data (blue continuous) when a mass $m=0.261$ kg is travelling on the two-span beam.	31

Figure 2.12. Time history of the deflections at sensor location x_{s1} - x_{s3} numerically (red dashed) and experimentally measured (blue continuous).	32
Figure 2.13. Two masses move on the two-span continuous beam, deflection error due to supports (red arrows).	32
Figure 2.14. Schematic drawing of the elements of an electrodynamic shaker and the interaction with a simply supported beam.	34
Figure 2.15. Magnitude of the FRF $H(s)$ of the input force/ input voltage (top) and phase angle (bottom).	37
Figure 2.16. Magnitude of the FRF $H(s)$ with an added mass at $x_m = 0.3$ m.	38
Figure 2.17. Bode diagram of the impedance of the electrodynamic shaker-beam system.	38
Figure 2.18. FRF of the force transmitted to the beam per coil force.	39
Figure 2.19. Bode diagram of the first-order shaker model.	40
Figure 2.20. FRF input force over input voltage for rigid simply supported beam controlled by an electrodynamic shaker.	41
Figure 2.21. Experimental validation between the displacements of masses travelling at different speeds obtained by the numerical model (blue continuous) and the experimental measurements (red dashed).	42
Figure 2.22. Validation of the beam mass system with an active electromagnetic shaker, numerical model (blue continuous), and the experimental measurements (red dashed).	43
Figure 2.23. The time history of the midspan deflection under the effect of a moving mass and a moving load, 3 modes are used, $N=100N$, $v=11.1m/s$ (compare with figure 3b in [26]).	44
Figure 2.24. Numerical validation of the deflection of the beam mass system with an active electromagnetic shaker at sensor location x_{s2} , moving mass system (blue continuous) and numeric moving force system (red dashed).	45
Figure 2.25. Dynamic amplification factor over the speed ratio for the moving force model (blue) and for the moving mass model (red dashed), for mass $m = 0.26$ kg, mass ratio $m/M = 0.81$ (left) and $m = 0.5$ kg, $m/M = 1.56$ (right).	46
Figure 2.26. Time history of the deflection w at sensor location $x_{s2} = 0.75$ m of a two-span beam excited upon a moving mass (blue continuous) or	

moving load (red dashed) travelling with $v = 1.5$ m/s (top) and $v = 3$ m/s (bottom).	47
Figure 2.27. Comparison of the DAF at the midspan of the first span (left) and at the midspan of the second span (right) with mass $m = 0.261$ kg travelling utilising the moving force model (blue continuous) and of the moving mass model (red dashed).	48
Figure 2.28. One piezoelectric actuator located on a beam structure.	50
Figure 2.29. An MFC laminate using the 33-mode of piezoelectricity.	50
Figure 2.30. Experimental set-up of the aluminium beam actuated by piezoelectric actuator.	53
Figure 2.31. Time history of the deflection of the numerical model (red dashed) and the experimental measurements (blue) at sensor locations and $xs3$ (bottom).	54
Figure 2.32. Time history of the deflection at sensor locations $w(xs2)$ and $w(xs3)$ of the numerical model (bluedashed) and the experimental data (redcontinuous).	55
Figure 2.33. Time history of the deflection of the two-span beam structure at sensor locations $xs1$ and $xs2$, measurements (blue continuous), numerical model (red dashed).	56
Figure 2.34. Input voltage $U1$ for piezoelectric actuator MFC 1.	56
Figure 2.35. Time history of the deflections of the two-span continuous beam at sensor locations $xs1 - xs3$, measurements (blue continuous) and numerical model (red dashed).	57
Figure 2.36. Time history of the input voltages $U1$ (top) and $U2$ (bottom).	58
Figure 5.1. Comparison modal coordinates numerical model (black dashed) and the measured signal (blue continuous).	66
Figure 5.2. Comparison of the modal coordinates numerical model (red continuous) and the measured signal (blue dashed).	68
Figure 5.3. Block chart of the time-varying (tv) system with the full-state time-invariant (ti) observer control.	69
Figure 5.4. Mode shapes of the time-invariant controlled system simulated with the ode solver as a continuous system (green continuous), system states (red dashed), observer states (blue dash-dotted) mass $m = 0.501$ kg, speed $v = 0.5$ m/s.	70

- Figure 5.5.** Deflection responses $w(xs2)$ of the controlled discrete system with added measurement noise (blue), the uncontrolled continuous structure (red) (right) and of the discrete observer (left). 71
- Figure 5.6.** Comparison of the mode shapes of the continuously controlled system (green) with the discrete system modes (red dashed) and discrete time observer (blue dash-dotted) for the sampling time $Ts = 5$ ms. 71
- Figure 5.7.** Input voltages u calculated by the discrete time observer for $Ts = 0.2$ ms (left) and $Ts=5$ ms. 72
- Figure 5.8.** Comparison of the deflection history at $wxs2$ for the time-invariant continuous control (green continuous), for the discrete observer (red dashed), for the discrete system (blue dash-dotted) and the continuous uncontrolled structure (black dashed) (left), input voltage of the discrete time-invariant observer (right). 73
- Figure 5.9.** Modal coordinates of the continuous system (green continuous) and the discrete system (red dashed) and the observer (blue dot-dashed) for $Ts=10$ ms and $xa = 0.25$ m. 74
- Figure 5.10.** Numerical deflection of the moving coordinate vt of the mass $m = 0.5$ kg travelling with velocity $v = 0.3$ ms⁻¹, no control (NC), time-invariant control (Ti) and time-varying system control (Tv). 76
- Figure 5.11.** Time history of the deflection response of the simply supported beam, $m = 0.261$ kg, $v = 0.55$ ms⁻¹. 76
- Figure 5.12.** Deflection response mass $m = 0.261$ kg along the moving coordinate of the beam modelled with six modes (red continuous), two modes (blue dash-dotted) and three modes (black dashed). 77
- Figure 5.13.** Relative experimental maximum deflection measured at $xs2$ normalised to the uncontrolled structure (nc) of the time-invariant control (Ti) (a) and the time-varying control (Tv) (b) from using one state to using all states. 78
- Figure 5.14.** Theoretical relative maximum deflection measured at $xs2$ normalised to the uncontrolled structure (nc) of the time-invariant control (Ti) (a) and the time-varying control (Tv) (b) from using one state to using all states. 79
- Figure 5.15.** Deflection response mass $m = 0.261$ kg along the moving coordinate of the beam modelled with all three modes no control (black dotted), time-invariant (red dashed) and time-variant (blue dash-dotted). 79

- Figure 5.16.** Development of the time-varying gains $k_1(t)$ (a), $k_2(t)$ (b) and $k_4(t)$ (c) for the three different masses $m = 0.261$ kg (blue dotted), $m = 0.371$ kg (red dashed) to $m = 0.509$ kg (black continuous) at velocity $v = 0.3$ ms⁻¹. 80
- Figure 5.17.** Time history of the poles of the time-varying controlled system, first and third mode (blue continuous), second and fourth mode (red dashed), poles of the time-invariant system (black crossed), $m = 0.5$ kg, $v = 0.55$ m/s. 81
- Figure 5.18.** Comparison of the first four poles of the time-varying system with the reduced order controller (left) and with the full state controller (right) unstable poles (black asterisks), $m = 0.5$ kg, $v = 5.6$ m/s. 82
- Figure 5.19.** Mass $m = 0.509$ kg moving with $v = 0.3$ ms⁻¹, comparison of the displacement $w(x_{s2})$ for the numerically calculated data (blue continuous) and the experimentally measured data (red dashed), for the case without control (a), with the time-invariant control (b), with the time-varying control (c) and the values of the relative maximum deflection in percent (d). 83
- Figure 5.20.** Time history of the experimentally measured control input at the compactRio (left) and at the electrodynamic shaker (right), time-invariant (blue continuous) and time varying (red dashed). 84
- Figure 5.21.** Mass $m = 0.261$ kg moving with $v = 0.55$ ms⁻¹, comparison of the displacement $w(x_{s2})$ for the numerically calculated data (blue continuous) and the experimentally measured data (red dashed), for the case without control (a), with the time-invariant control (b), with the time-varying control (c) and the values of the relative maximum deflection measured at $xs2$ in percent (d). 85
- Figure 5.22.** Mass $m = 0.261$ kg moving with $v = 0.55$ ms⁻¹, comparison of the velocity (v_{s3}) for the numerically calculated data (blue continuous) and the experimentally measured data (red dashed), for the case without control (a), with the time-invariant control (b), with the time-varying control (c). 86
- Figure 5.23.** Effect of using time-varying gain $\mathbf{k}(m_1)$ (left) and scheduled for each mass specifically (right) $\mathbf{k}(m_1) - \mathbf{k}(m_4)$. 87

- Figure 5.24.** Relative maximum deflection for mass m_2 (a) and mass m_4 (b) using gain $k(m_1)$ (blue) in comparison to using the specific gains $k(m_2)$ or $k(m_1)$ (red). 88
- Figure 5.25.** Principle of 1D interpolation in LabView. 89
- Figure 5.26.** Deflection $w(x_{s2})$, no control action (NC) and with different speeds v (a); time-varying gain $k_1(m_4)$ (b) calculated in real-time (blue dashed) and numerically (red continuous). 89
- Figure 5.27.** Mass $m_1 = 0.261$ kg moving with $v = 0.3$ ms⁻¹, comparison of the displacement $w(x_{s2})$ for the numerically calculated data (blue continuous) and the experimentally measured data (red dashed), for the case without control (a), with the time-variant control (b), with the time-varying augmented control (c) and the values of the relative maximum deflection measured at x_{s2} in percent (d). 92
- Figure 5.28.** Mass $m_4 = 0.509$ kg moving with $v = 0.55$ ms⁻¹, comparison of the displacement $w(x_{s2})$ for the numerically calculated data (blue-continuous) and the experimentally measured data (red dashed), for the case without control (a), with the time-variant control (b), with the time-varying augmented control (c) and the values of the relative maximum deflection measured at x_{s2} in percent (d). 93
- Figure 5.29.** Effect of using time-varying gain $k(m_1)$ (left) and scheduled for each mass specifically (right) $k(m_1) - k(m_4)$ for the augmented control. 93
- Figure 6.1.** Block diagram of the displacement feedback control for the one-span beam. 95
- Figure 6.2.** Mass $m_1 = 0.261$ kg moving on the structure, comparison of the displacement $w_{x_{s2}}$ for the experimentally measured data (blue continuous) and the numerically calculated data (red dashed), for the case without control (a), with the linear displacement feedback control (b) and the cubic displacement control (c). 97
- Figure 6.3.** Mass $m_4 = 0.509$ kg moving on the structure, comparison of the displacement $w_{x_{s2}}$ for the experimentally measured data (blue continuous) and the numerically calculated data (red dashed), for the case without control (a), with the linear displacement feedback control (b) and the cubic displacement control (c). 98
- Figure 6.4.** Time history of the displacement responses experimental (blue continuous) and numerical (red dashed) $w(x_{s1}) - w(x_{s3})$

	comparing the uncontrolled structure with the cubic displacement rule controlled structure (right), mass m_4 , $k = 2$ at $v = 0.28 \text{ ms}^{-1}$.	99
Figure 6.5.	Control input $u_1(t)$ for the cubic control with $k = 2$ and m_4 .	100
Figure 6.6.	Comparison of the reduction of deflection for the linear control (blue) and for the cubic control (red) for masses $m_1 = 0.261 \text{ kg}$, $m_2 = 0.322 \text{ kg}$, $m_3 = 0.371 \text{ kg}$ and $m_4 = 0.509 \text{ kg}$.	100
Figure 6.7.	Gain scheduling approach for the linear displacement control (blue) and for the cubic displacement control (black).	101
Figure 6.8.	Time history of the deflection $w(x_{s1}) - w(x_{s3})$ of the uncontrolled two-span beam (left) and the controlled two-span beam (right), experimentally (blue continuous) and numerically (red dashed).	102
Figure 6.9.	Experimental input values u_1 and u_2 for the piezoelectric actuators with the cubic displacement feedback control.	105
Figure 6.10.	Time history of the deflection data $w(x_{s1})$ cubic displacement feedback control applied to the two span beam with $k=3$	105
Figure 6.11.	Deflection responses $w(x_{s1}) - w(x_{s3})$ of the uncontrolled structure (left) and the cubically controlled structure (right), numerically (red dashed) and experimentally (blue continuous) when two masses $m_3 = 0.371 \text{ kg}$ and $m_4 = 0.509 \text{ kg}$ travel on the beam.	106
Figure 7.1.	Time history of the deflection response $w(0.3 \text{ m})$ of the beam structure with a mass of $m = 0.509 \text{ kg}$ travelling with a speed of $v = 1 \text{ m/s}$, $r_w = 1 \times 10^{-11}$, $N_p = 6$, $N_c = 4$,	115
Figure 7.2.	Time history of the deflection response $w(0.3 \text{ m})$ (left) and of the control Voltage (right) of the MPC controlled simply supported beam, $N_p = 6$, $N_c = 4$, $r_w = 1 \times 10^{-6}$	115
Figure 7.3.	Time history of the deflection response $w(0.3 \text{ m})$ (left) and of the control Voltage (right) of the MPC controlled simply supported beam, $N_p = 6$, $N_c = 1$, $r_w = 1 \times 10^{-11}$	116
Figure 7.4.	Runtime during the control loop over the travelling time.	117
Figure 7.5.	Time history the beam's deflection at the first mid-span location (a) and at the second mid-span (b) of the uncontrolled structure (blue-dashed) and of the MPC constrained controlled structure (red continuous).	118
Figure 7.6.	Time history of the control input variables u_1 and u_2 .	118

- Figure 7.7.** Deflection responses $w(xs1)$ and $w(xs2)$ for MPC control with $N_c=4$ and $N_p=6$. 119
- Figure 7.8.** Comparison of the runtime of the constraint MPC control with $N_p=6$ and $N_c=4, 8$ modes used and the minimal MPC control with $N_p=2$ and $N_c=1$ and 3 modes used. 120
- Figure 7.9.** Deflection responses $w(xs1)$ for the uncontrolled structure (blue dash-dotted), of the MPC controlled structure with 3 modes (red continuous), and the 12 modes structure fed with u of the 3 modes MPC (black dotted). 120

List of Tables

Table 1.1	Literature theoretical and experimental active control of the moving mass	10
Table 2.1.	Non-dimensional parameters λ_i for two equal span continuous beams	23
Table 2.2.	Comparison of the natural frequencies of the analytical method and the approximated method	25
Table 2.3.	Parameter estimates for electrodynamic shaker (Data Physics V4) taken from [84].....	36
Table 5.1.	Relative maximum deflection at x_{s2} for different masses travelling at $v = 0.3 \text{ ms}^{-1}$ in percent.	83
Table 5.2.	Relative maximum deflection measured at x_{s2} for different masses travelling at $v = 0.55 \text{ ms}^{-1}$ in percent.	84
Table 5.3	Relative maximum deflection at x_{s2} for different masses travelling at $v = 0.3 \text{ ms}^{-1}$ in percent for the uncontrolled system	91
Table 5.4	Relative maximum deflection at x_{s2} for different masses travelling at $v = 0.55 \text{ ms}^{-1}$ in percent	91
Table 6.1.	Maximum experimental deflection at $w(x_{s1})$ open-loop (NC), cubic feedback, and difference dw between NC and cubic, theoretical linear control for reference	103
Table 6.2.	Maximum experimental (ex) and theoretical (th) deflections at $w(x_{s3})$ open-loop (NC), cubic feedback and linear control, difference dw (ex) between NC (ex) and cubic (ex), difference dw (th) between NC (th) and linear control (th) for reference.....	104
Table 6.3.	Maximum positive deflection at $w(x_{s3})$ open-loop (NC), cubic feedback, and difference dw	104

List of Symbols

Latin Symbols

a	Acceleration
A	Section area
A_a	Accelerance of the electrodynamic actuator
A_0	Accelerance of the beam
\mathbf{A}	System matrix
\mathbf{B}	Input matrix
\mathbf{B}_f	Disturbance input matrix
C_0	Specific piezoelectric constant
c	Damping coefficient
c_p	Correction factor piezoelectric actuator
c_s	Damping coefficient of the shaker
\mathbf{C}	Modal damping vector
\mathbf{D}	Damping matrix
\mathbf{D}_a	Damping matrix actuator
$\Delta\mathbf{D}$	Time-varying damping matrix
d_{31}	Piezoelectric constant, elongation lateral to the applied electric field
d_{33}	Piezoelectric constant, elongation parallel to the applied electric field

E	Electric field
E_b	Young's modulus beam
E_p	Young's modulus piezoelectric material
\mathbf{E}, \mathbf{F}	Matrices describing the general objective function of a constraint problem
f	Control force
f_{3dB}	Cut-off frequency
F	Force transferred to the beam
F_c	Coil force
\mathbf{F}	Terminal cost matrix
\mathbf{F}, Φ	Pair of matrices used in the prediction equation $\mathbf{Y} = \mathbf{F}\mathbf{x}(k_i) + \Phi\Delta\mathbf{U}$
g	Gravitational acceleration
g_a	Gain amplifier
H_0	Mobility of the beam
H_a	Mobility of the electrodynamic shaker
H_{mod}	Mobility of the modified structure
h	Height of the beam
h_p	height piezoelectric actuator
I	Moment of Inertia
$I(s)$	Electric current
J	Performance index
k	Sampling step

k	Stiffness constant
k_i	i -th element of the gain vector \mathbf{k}
k_s	Stiffness suspension electrodynamic shaker
\mathbf{K}	Stiffness matrix
\mathbf{K}_a	Stiffness matrix actuator
\mathbf{K}_p	Stiffness matrix piezoelectric actuator
$\Delta\mathbf{K}$	Time-varying stiffness matrix
\mathbf{k}	Gain vector
L	Total Length of the beam structure
L_e	Distance between two electrodes
l	Span -length
\mathbf{L}	Observer gain matrix
m	Mass of the moving load
m_s	Moving mass of the electrodynamic shaker
M	Mass of the structure
M_p	Moment applied by piezoelectric actuator
\mathbf{M}	Mass Matrix
$\mathbf{M}, \boldsymbol{\gamma}$	Pair of matrix and vector used in the inequality constraint ($\mathbf{M}\mathbf{x} \leq \boldsymbol{\gamma}$)
\mathbf{M}_p	Mass matrix piezoelectric actuator
$\Delta\mathbf{M}$	Time-varying mass matrix
N	Normal Force
N_a	Number of supports

N_c	Control horizon
N_p	Prediction horizon
P	Riccati matrix
q_j	j -th modal coordinate
q	Modal coordinates vector
Q	State weighting matrix
R	Resistance
R	Control weighting matrix
R_n	Error covariance matrix
$\bar{\mathbf{R}}$	Tuning matrix for the model predictive control approach
s	Laplace variable
t	Time instant
t_f	Leaving time of the mass
t_{ob}	Actual time instant mass is travelling on the beam
T_s	Sampling time
u_{max}	Positive boundary input value
U	Voltage
$\Delta \mathbf{U}$	Future control trajectory vector
v	velocity
v_{cr}	Critical velocity
w	Transverse motion of the beam

w_l	Displacement of the moving mass
\mathbf{w}_d	State disturbance vector
\mathbf{w}_n	Sensor disturbance vector
x	Position of the mass
x_1, x_2	Start and end location of the piezoelectric actuator
x_a	Position actuator
x_s	Location of the displacement sensors
\mathbf{x}	State vector
$\hat{\mathbf{x}}$	Estimated state vector
\mathbf{y}	Measurement vector
\mathbf{Y}	Future output matrix
z	Distance to the neutral axis

Greek Symbols

α, β, γ	Constants defining the first order electrodynamic shaker model
β_i	Constant defined by boundary conditions of the beam
ϵ_{33}	Strain in the x -direction
ζ	Damping ratio
λ	Lagrange multiplier vector
ρ	Density

σ_{33}	Stress in the x direction
ψ_j	j -th mode shape of a structure
Ψ	Vector of mode shapes
Ψ	Matrix of mode shapes
ω_i	i -th natural frequency

Operators and Indexing

d	Differential operator
diag	Diagonal matrix
\mathbb{E}	Expected value
\mathcal{H}	Hamiltonian
\mathbf{I}_{ij}	Identity matrix
∂	Partial Differential Operator
δ	Dirac Delta-Distribution
δ_{ij}	Kronecker delta index
$(\cdot \dot{\cdot})$	Derivation in time
(\cdot')	Derivation in space

List of Abbreviations

ADC	Analogue-to-Digital Converter
amp	Amplifier
CPU	Central Processing Unit
DAF	Dynamic Amplification Factor
EMF	Electromotive Force
ex	Experimental
FE	Finite Element
FRF	Frequency Response Function
GPC	General Predictive Control
HVA	High Voltage Amplifier
IDE	Interdigitated Electrodes
LQG	Linear Quadratic Gaussian
LQR	Linear-Quadratic Regulator
MFC	Micro Fibre Composites
MIMO	Multi Input Multi Output
MPC	Model Predictive Control
MS	Mode Superposition
NC	No Control
PD	Proportional Derivative
PZT	Lead Zirconium Titanate
SISO	Single Input Single Output

ti	Time-invariant
tv	Time-varying
th	Theoretical

1 Introduction

Active control of structures subjected to moving and therefore transient loads plays a crucial role in a large variety of engineering applications such as, vehicle/pedestrian –bridge interaction, overhead cranes, linear robots, maglev guideways and railway catenary-pantographs [1–7]. Lighter and more slender structures, arising from more efficient use of resources, optimised geometries and aesthetic considerations, are more susceptible to excessive vibration levels.

In particular the problem of moving loads in relation to bridge-structure interaction has been studied extensively both analytically and experimentally [8,9]. For structural engineers, it is not only the modelling that is of particular interest, but also the improving of the dynamic response of the supporting structure to specific moving loads, which in the case of a bridge could be the effects of different traffic loads. An example of pedestrian induced vibration affecting the serviceability of a structure was the initial operation of the millennium bridge in London in June 2000 [10]. Longitudinal vibrations were caused by a near resonance of one or more modes, induced by the frequencies of the human load. Passive vibration control had to be installed afterwards to ensure the serviceability. A number of studies can be found in the research literature that put forward passive methods designed to address this specific problem. The passive approach is attractive as it offers a low cost solution [11–14], but it is less efficient when the structure is subjected to loads with random variations in parameters such as moving speed and weight.

Active vibration control methods offer greater efficiency by reducing broadband frequencies and by allowing a higher and flexible actuation [15] which in the context of a moving mass structure means that the control could adapt actively to different weights and speeds. In addition, active vibration control is becoming increasingly important in the design of handling devices and flexible robots, as lightweight structures reduce inertia and increase the mobility of the moving parts [16,17]. Traditional technologies like structural optimization and passive damping can only be applied up to certain limits. Here the application of new actuator technologies such as macro fibre composite (MFC) piezoelectric actuators is of particular interest, as they can offer high flexibility, small geometries and strong actuation forces [18–24].

1.1 Aims and objectives

In recent years, much research has been done in the field of theoretical and numerical investigation of active control of moving load structures [2,25–27]. In contrast, there are only a few studies dealing with the experimental implementation and validation of the active control of structures under this particular type of excitation [16,17].

The aim of this study is the experimental implementation of active vibration control approaches for a simply supported beam and a two-span continuous beam, acted upon by a stream of moving masses. Optimal control approaches include the system model and the moving load in the control synthesis and can theoretically guarantee optimality and stability. Therefore, these will be studied in the first part of this study. The extension consists in the numerical study of the model predictive control approach as it is able to take into account the saturation limits of the actuator. In addition, linear and nonlinear feedback control approaches are implemented as they provide an intuitive method for implementation. The first studies will be carried out with an electrodynamic actuator as this is widely used in research institutions and industry. Later, the novel piezoelectric MFC actuators will be attached to the beam, modelled and used to control the test-structures.

Parts of this study are published in [28], where reduced order active control by an electrodynamic shaker is applied to reduce the deflection of a simply supported beam subjected to moving loads.

The next section reviews the scientific literature, including theoretical and experimental work in the field of active vibration control of moving load structures.

1.2 Literature Review

The literature review covers different areas relevant to the active structural control of simply supported and two-span continuous beams. First the most relevant studies for the closed solution of the general moving mass problem are presented. Then the particularities of modelling multi-span continuous structures are reviewed in the literature. Followed by the numerical and experimental studies covering the active control of moving load beam structures in modal coordinates. The literature covering displacement feedback control is

reviewed afterwards. Finally, the potential of applying the novel MFC actuator technology is examined as well as the literature relevant in terms of applying the model predictive control approach in active structural control.

The General Moving Mass Problem

With an increasing mass ratio, defined as the ratio between moving mass and the supporting structure, and increasing moving speeds, the inertia effects of the load have to be considered in the modelling of the moving load structure [25,26,29]. An accurate and computationally efficient model of the system is important to design a stable controller as well as to simulate the moving load structure. Therefore, a compromise must be found between sufficient accuracy of the results and computationally efficient algorithms. Modal coordinate transformations can offer these properties. It may take over hundreds degrees of freedom in a finite element (FE) model to represent the system dynamics accurately whereas in modal coordinates this may be modelled by ten modes to represent the frequency range of interest [30]. This is of special importance to realise fast real-time capable model-based control algorithms for the later active control of slender structures.

Fryba [8] studied different load cases for beam structures, from the perspective of train-bridge vibrations. He presents the derivation of the moving force problem in different scenarios as well as the closed-form solutions of vibrations on modal coordinates of an Euler-Bernoulli beam crossed by a continuous moving load. The theoretical results were validated with experiments, e.g. for the continuous load by a train moving on a 56.56 m long bridge [31]. Ouyang [2] presents the derivation of a point wise mass moving on a simply supported beam with additional applications, e.g. wood saws and machine tools. Further theoretical studies for the general moving load problem are plentiful and may be found in [27,32–34] for example.

Modelling of Multi-Span Structures

The mode shapes of multi-span structures are difficult to derive numerically [35]. Boundary conditions of a previous span must be applied to the next span, and the mode expressions vary with each span. A possible control algorithm would have to switch to different mode shapes for each span. The exact mode shapes for a continuous two-span beam can be found

in [36] where it is used in the vibration analysis of continuous maglev guideway of a magnetic levitation system. Yang [35] presented exact modes shapes in the vibration analysis of two-span and four-span continuous beam structures. For a more complex four-span plate structure with two rails, Yang [5,34,35] modelled the supporting structure using mode shapes determined by the FE-method. This model was then used to calculate the structural response by mode superposition in MATLAB. The FE-model can be updated by the experimentally measured natural frequencies. Stancioiu et. al [37] derived the mode shapes for a four-span flexible beam structure acted upon by one or two steel balls. The numerically obtained results showed a good match with experimentally measured displacement data for low speeds of the moving mass, when the permanent contact of the load can be assured.

Several studies approximated the mode shapes of multi-span structures by adding springs with adequate stiffness at the support locations [38–41]. For vibration control this method is preferred as the mode shapes of a single-span beam can be utilised for the whole structure. A drawback could be that a relatively high number of modes must be used to approximate the mode shapes of multi-span beam structures with sufficient accuracy.

General Active Structural Control

Preumont [42] presents a detailed introduction into the field of active vibration control of structures. It comprises modelling of the structural system and the design of control systems in state space as well as frequency based single-input-single-output control systems. Important studies regarding the general active control of flexible system go back to of Balas [43] and Goh et. al. [44]. In [43] the controller was designed in state space with an additional Luenberger observer. He examined the control and observation spillover, where higher unmodelled modes get excited by the controller. Goh et. al [44] introduces the positive position feedback (PPF), which can handle the spill over effect and increases the damping of the system. Several researchers extended this concept further [45–47]. Extensions of the concept are the positive velocity feedback controller [48] acceleration feedback control [49]. Korkmaz [3] presents in his review an overview of feasible applications of active control structures in engineering and its computing challenges , which are greatest when there is no closed form of solution for control commands. This is the case for nonlinear structures

Active Control of Moving Mass Beam Structures in Modal Coordinates

Several studies have investigated the active control of a structure subjected to a moving mass, numerically modelling the structure in modal coordinates. Sung [50] presented the dynamic modelling and the time-invariant optimal control of a simply supported beam under a moving mass. He used two piezoelectric actuators, and their locations were determined by an optimal quadratic cost functional.

Deng et al. [51,52] used a linear-quadratic Gaussian (LQG) modal controller for a time-varying structure including identification and control update in real-time. The numerical model, which alters due to structural changes, is updated in the observer. The method was validated numerically. The time-varying nature of the system was taken into account in [26] where Nikkhoo et. al proposed a method based on solving the Riccati equation at every time-step. In [26,29] it is shown that for a high travelling speed, and for certain locations and numbers of actuators, time-varying control shows a significant improvement compared to the time-invariant control. Rofooei and Nikkhoo [53] studied numerically the application of a classical closed-loop control of a number of piezo patches bonded on a thin rectangular plate under the excitation of a moving mass. It was shown that higher frequency vibrational modes must be included to obtain the correct system response for large values of moving mass weight and velocity for this type of structure. The desired deflection responses were achieved with moderately low levels of input voltage to the actuators. Nikkhoo [25] derived the equations of motion for a single and a multi-span beam in which a number of piezoelectric patches are bonded to it modelled by the Hamiltonian principle. The classical linear optimal control approach based on displacement-velocity and velocity-acceleration feedback is applied to the beams under the influence of a moving load and a moving mass. Stancioiu et al. [29] cast the problem into a terminal-time optimal control framework [54] and further presented a numerical study for synthesis of time-varying control solutions. This study also introduced an augmented system, which took into account the effect of the moving mass in the control synthesis problem. A drawback of the study was that it assumed full knowledge of the state-variables, which have to be estimated for experimental studies. A combination of sliding mode control and positive position feedback for a beam subjected to a moving mass was presented in [55]. The sliding mode controller, used when the mass moves along the beam, is robust to parameter uncertainties and the positive position feedback control is efficient in suppressing the free vibration of the supporting structure after the mass leaves the beam. To increase the damping in the system, the positive position feedback control introduced by Goh & Caughy [56] and further studied in [45,57] can be

applied. However, for the moving load problem this approach does not reduce the deflection response but could be applied when the mass is leaving the structure. Liu et. al. [58] devised a finite-time optimal regulator for an uncertain beam-mass system. The distributed material parameters were discretised for representative points and the regulator calculated with the probability density equation method.

Despite a large number of studies dedicated to numerical solutions, only a few studies approached the problem of experimental implementation and validation of vibration control of moving masses. One of the main difficulties in the experimental implementation of the controller is that the states are not directly accessible when the dynamic equations are set up in modal space. Therefore, an observer or state-estimator needs to be considered. This in turn leads to high computational time which counteracts the real-time ability of the controller.

Shelley et al. [59] implemented and studied, on a 80 m long highway bridge, the feasibility of an independent modal space control which used electromagnetic proof mass actuator for control. This type of actuator does not need an external mount. The adaptive modal filter used here simplifies the response of a complicated structure to the response of an individual single-mode system [30,59]. The method proved its robustness against changes in temperature, sensor failure and changes of dynamic characteristics due to simultaneous destruction tests.

Frischgesell et. al. [16] studied a time-varying discrete observer for a moving mass system equipped with a force actuator. The aim was to minimise the maximum traverse deflection. The time-varying system and observer matrix were calculated offline at specific times due to the high computation time required. Reckmann and Popp [17] extended this work with an adaptation method and a discrete time optimal controller designed to achieve a lower deflection of the flexible structure. Bleicher et. al [60] implemented a multimodal and multivariable active vibration control on a 13 m long stressed ribbon footbridge. A Kalman filter estimated the modal states, and the velocity feedback control was designed in the modal state space representation. The aim was to control the first three vertical modes of the bridge which coincide with pedestrian induced vibration. Pisarski [61] studied numerically and experimentally the semi-active control of a structure subjected to a moving load. In this study, an open-loop optimal bang-bang controller was used. The study considered the moving speed and weight of the mass and it was shown that the controlled system outperforms the passive case by up to 21% in terms of the maximum structural deflection. This work was extended in [62] where a closed-loop adaptive control was proposed. The

control gains were calculated offline for a constant speed and mass of the load with the ability to adapt online to the actual mass parameters.

The first part of this study presents an experimental approach to the problem of active control of a structure under moving loads. The solution is based on an optimal time-varying control algorithm and relies on a state-feedback controller. A new method to estimate the states of the system (modal coordinates and modal velocities) is proposed based on the inverse of the matrix of modal shape vectors and measured displacements. This simpler algorithm allows fast sampling times and proves to be robust against structural changes. This method of state estimation was first presented by the authors in [63], where a suboptimal controller was implemented to reduce the deflection of the beam at given locations. Although the time-varying nature of the system is taken into account in the control approach, an objective function based on deflection responses requires an adaptation of the control effort to the mass and velocities of the load acting on the supporting structure. The feasibility of a simple gain scheduling procedure is investigated and shows a good performance for a control effort adjusted to the dynamic parameters of the problem.

Displacement Feedback Control for Structures Subjected to Moving Loads

As the previous literature illustrated, many studies of active vibration control are formulated in modal space. This approach can guarantee stability and can handle multi-input-multi-output (MIMO) systems. In addition, the time-varying nature of the system can be compensated by the controller. On the other hand, this approach requires the estimation of the modal coordinates which are not directly measurable. A discrete time observer requires fast sampling time to estimate the states of the continuous system accurately. Multi-span beams, where the supports are approximated by stiff springs require a high number of modes to represent the dynamic response accurately. These factors complicate the application of optimal control approaches for multi-span continuous structures. Displacement feedback methods may be more straightforward to implement, although stability cannot be guaranteed and has to be simulated or verified experimentally.

In [64] Sloss et al. solve a min max problem for a displacement feedback control of beams under moving loads. The control objective was to find a constant gain where the maximum deflection of the beam does not exceed a given value. Stancioiu et. al [41] applied a negative displacement feedback and cubic displacement to a four-span beam structure acted upon multiple moving loads. As actuators, electrodynamic shakers were chosen. Each span was

viewed as a single-input-single-output (SISO) system, and compensators were added to increase the system's stability margins. It was shown numerically and experimentally that, by both methods, the vibration response of the structure under moving masses can be reduced effectively. The nonlinear cubic displacement feedback provides a better control action for heavier masses.

The second control approach in this study uses MFC actuators with negative displacement feedback similar to the method used in [41] for a single and a two-span beam structure. Numerical results are validated with experimental data.

Piezoelectric Macro Fibre Composite Actuators in Active Structural Control

Piezo ceramics offer attractive properties in active vibration control as they are light weight, low-cost and easy to implement. In these devices, an electric potential is converted into mechanical strain. Most often 31-mode actuators, where the numbers symbolize the directions of polarization and elongation in Cartesian coordinates (more details are presented in section 2.4.1), are used in bending applications e.g. in [25,42,65].

In contrast Macro Fibre Composites (MFC) actuators can use the 33-piezoelectric mode, where the strain constant is 50% to 100% larger compared to those of the 31-mode [66]. With the concept of interdigitated electrodes first presented by Hagood and Bent [67,68], the 33-mode actuator can be utilised for larger scale actuation and sensing. The concept of Macro Fibre Composites, developed by researchers at the NASA Langley Research Center [69], is based on interdigitated electrodes with piezoelectric fibres of rectangular cross section. With them it is possible to overcome drawbacks of limited interactions between fibres and electrodes. First applications of MFCs in actuation and sensing were presented by Sodano and Inman [20]. Modal testing of an inflated torus, structural health monitoring of bolted joints, self-sensing vibration control of a beam were presented and the effectiveness shown. Song et al. [22] presents a review of applications of the vibration control using piezo ceramics in civil structures, stating also the limits of piezoelectric actuation which are the relatively small displacement and limited actuation force. Due to the higher actuation forces MFC actuators can be considered as a step towards the realisation of real life applications for this type of smart structure.

Despite a rich literature which utilises piezoelectric actuators for the general active vibration control problem [19,65,70–72] only a few numerical and experimental studies can be found

which utilise them for the vibration control of moving load structures [25,53,73]. Zhao and Wu [73] modelled a robotic arm with an moving end as a rotating beam with a moving mass. The equations were derived with Lagrange's equation, and linear classical optimal control was applied. Numerical examples were used to evaluate the control performance.

Zeki et al. [74] studied proportional displacement feedback control of a clamped fixed beam acted upon moving loads applied by a robotic air nozzle. The feedback system was derived by FE method in ANSYS. 31-mode Lead Zirconium Titanate (PZT) transducer were used. Numerical results were validated by experiments, where the residual vibration could be reduced. The numerical model consisted of nearly 500 elements. A similar model in modal coordinates could be modelled by only 6 modes with high accuracy, which illustrates the numerical efficiency of the modelling in modal coordinates. Eldali and Baz [75,76] successfully applied feedforward control to a cylindrical shell under a transient pressure pulse propelling a moving mass. The experimental study utilises piezoelectric stack actuators to damp radial and circumferential vibrations measured by using a high-frequency strain gage system.

Model Predictive Control of Structures Subjected to Moving Loads

When applying piezoelectric actuation, saturation limits have to be considered. Model predictive control is described as presently the only control method able to handle process constraints explicitly on an algorithmic level [77,78]. This is of special concern when applying piezoelectric actuators as exceeding the operational voltage leads rapidly to depolarization and failure. In practice these bounds can be implemented by limiting the maximum control voltage but this introduces nonlinearities to an otherwise linear controller which can affect stability and performance [77]. With the dual-mode paradigm, stability can be ensured and operational bounds are enforced through active set methods [77].

The model predictive control approach originated from applications in process and chemical industry [79,80]. It has the advantage that current and future set-points, disturbances and constraints can be included into the optimal control approach.

Recent developments in hardware technologies allow the application of MPC in systems which require fast sampling times such as active structural control [81–85]. MPC without constraint handling does not require online optimization, thus implementation at a high sampling rate is less problematic. Richelot et al. [83] studied experimentally the general predictive control (GPC) approach for clamped beam equipped with piezoelectric actuators.

The GPC approach is robust against model uncertainties. Stability is considered by collocation of the sensor-actuator pair. The first vibrational mode was damped actively. Hassan et al. [84] experimentally applied the MPC approach to a MIMO system with multiple piezo actuators controlling a one-link actuator and demonstrated that the control is well suited for this case. Wills et al. [85] implemented an MPC to fixed free beam considering the saturation limits by quadratic programming. It was shown that the online optimization could be calculated on inexpensive hardware in less than $150 \mu s$. Stability guarantees were not considered. In contrast Takacs and Rohal'-Ilkiv [77] studied different optimal and suboptimal MPC-algorithms which guarantee feasibility and stability on a fixed-free beam test structure. The sub-optimal stable MPC is recommended for vibration attenuation purposes. The authors further implemented an adaptive infinite horizon dual mode constrained MPC [86] using an extended Kalman filter for the estimation of system states and model parameters. Oveisi et. al [87] applied an MPC scheme based on orthonormal Laguerre Functions to a lightly damped structure, which reduces the computational cost. Feasibility and stability can be guaranteed, and system uncertainties are incorporated by system identification.

Table 1.1 summarises the previously presented studies regarding the active control of the moving load problem. The theoretical and experimental studies are listed with their control approach, the utilized actuator and the corresponding structure.

Table 1.1. Literature theoretical and experimental active control of the moving mass

Theoretical Studies	Control Approach	Actuator	Structure
Deng et al. [51,52]	LQG	Not defined	Time-varying pendulum
Nikkhoo et al. [26,39]	Optimal Control	Piezoelectric Patches	Single and multi-span beams
Rofooei et al. [53]	Optimal Control	Piezoelectric Patches	Rectangular plate
Stancioiu et al. [29]	Optimal Control, Boundary value control	General force	Simply supported

Pi et al. [55]	PPF, Sliding mode control	General boundary control torques	Multi-span
Liu et al.[58]	Optimal Control with handling of uncertainties	Force actuator	Simply supported
Sloss [64]	Displacement Feedback	General force	Simply supported beam
Zhao and Wu [73]	Optimal Control	Rotating Beam (Robot)	Piezoelectric Actuators
Experimental studies			
Shelley et al. [30,59]	Independent modal control	Electromagnetic proof mass actuator	Simply supported beam (highway bridge)
Frischgesell et al. [16]	Pole Placement with Luenberger Observer	Force Actuator	Simply supported beam
Reckmann and Popp [17]	Discrete Optimal Control with Observer, Adaptive Control	Force Actuator	Simply supported beam
Bleicher et. al[60]	Optimal Control	pneumatic muscle actuators	flexible stress ribbon footbridge
Pisarski [61,62]	Semi-active control	magneto-rheological rotary dampers equipped	Simply supported beam
Stancioiu et al. [41]	Negative Displacement Feedback	Electro dynamic actuator	Four span beam structure
Zeki et al. [74]	Displacement Feedback	Piezoelectric Patches	Fixed-free beam
Eldali and Baz [75,76]	Feedforward	Piezoelectric Stack	Cylindrical Shell

1.3 Knowledge gaps

In this section the main knowledge gaps are summarized. Despite the study of Reckmann [17] no studies were found which experimentally implemented the optimal control approach for the active control of simply supported beams subjected to moving masses. To the best knowledge of the author no experimental study was found implementing an optimal active structural control by an electrodynamic shaker. Furthermore, no experimental study has been found on the application of 33-mode MFC actuators in the active control of a simply supported beam or a two-span continuous beam acted upon by a single or multiple moving masses.

Despite the large body of literature using MPC in the general application of active vibration control, to the best knowledge of the author no study was found which applies the MPC approach to the moving load problem.

1.4 Methodology and Outline of the Thesis

Figure 1.1 outlines the methodology applied in this project to achieve the aims and objectives presented previously. The boxes/tasks presented herein will be presented in the different chapters.

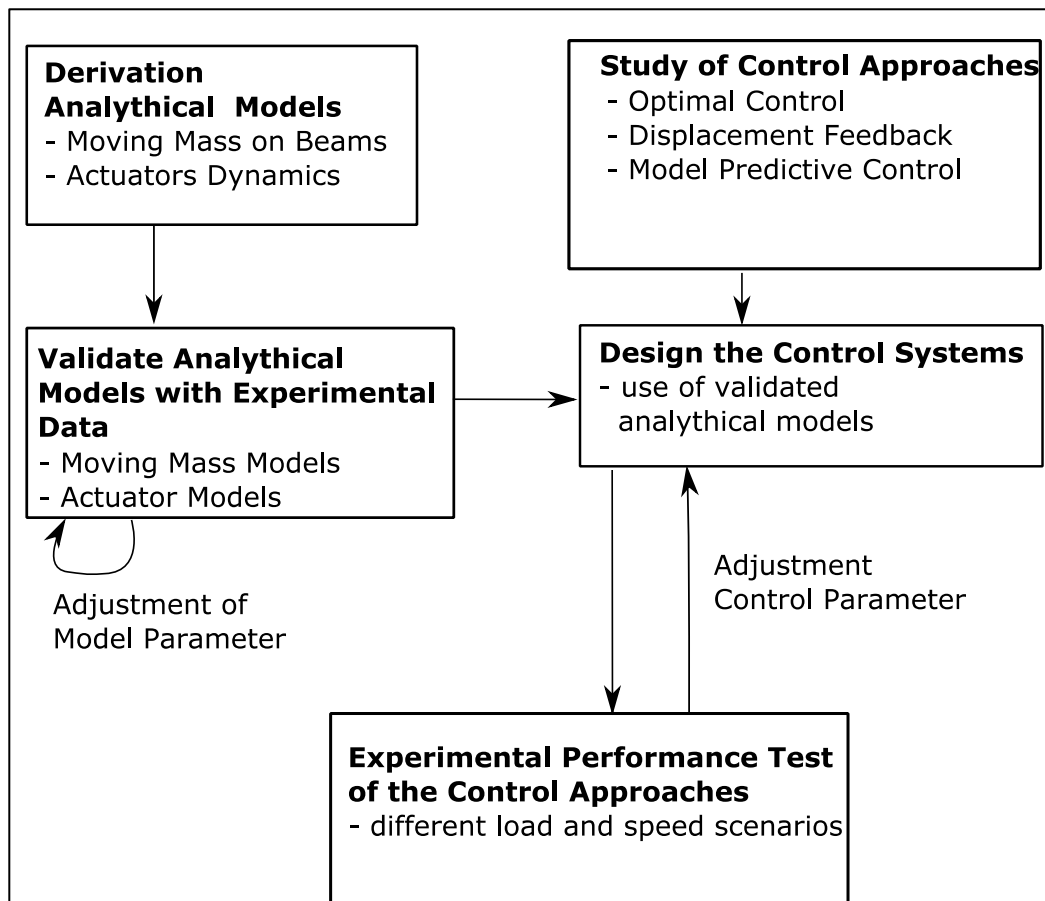


Figure 1.1. Methodology applied in the project.

In chapter 2 the theoretical model for the moving mass problem in modal space will be derived. The multi-span beam dynamics can be approximated by modelling the supports as spring-damper elements with high stiffness and damping coefficients. The approximated mode shapes will be validated numerically by comparing with the exact mode shapes. Experimental deflection data from the test structures will validate the accuracy of the numerical models. Two numerical models for the electrodynamic shaker will be studied, a detailed model in the frequency domain and a first order model approximation. The effect of dynamic amplification will be considered numerically for the test structures. The theoretical model of the MFC actuator controlling the beam structures will be derived and validated against experimental deflection data.

In chapter 3 the theoretical background for the finite-time optimal control algorithm is presented. In that the Riccati differential equation is solved backward with the terminal condition. A slightly different approach is the described using a step-by-step solution of the Riccati equation which mimics the linear quadratic regulator problem.

The particular problem inherent to the optimal control approach in structural control is the estimation of the modal states. Different methods will be studied in chapter 3.2. First the classical state observer approach and secondly the state estimation by a novel method utilizing the mode shapes. This method is straightforward to implement and offers promising real-time abilities.

In chapter 5 a detailed experimental validation of the finite-time control of a simply supported beam acted upon different moving masses and controlled by an electrodynamic shaker is presented. This includes experimental results for the estimation of the states using the analytical mode shapes. Due to the discretisation errors that occur in the full state estimator the estimation by mode shapes is preferred and a reduced state controller will be utilised. It is shown how the mass and speed dependent gains influence the control performance. A real-time gain adaptation to compensate for moving mass speed is implemented. With the augmented system, where the travelling mass can be included in the system equation, superior control performance can be achieved.

Chapter 6 presents results obtained for the negative displacement feedback control utilised on a simply supported and two-span continuous beam acted upon moving masses and regulated by MFC actuators. Herein the cubic displacement rule proves more efficient for heavier masses whereas the linear approach offers higher deflection reduction for small masses.

Special caution to control input saturation limits must be applied when utilizing piezoelectric actuators. The MPC control approach can handle these constraints in the optimal control approach by quadratic programming. It is presented and theoretically utilised on the test-structures in chapter 7.

Finally chapter 8 presents the conclusions of the work and directions of future work are recommended.

2 The Moving Mass-Structure Interaction Models

In this chapter, the theoretical model for the moving mass-structure interaction will be derived to fully understand its complex dynamics, resulting from the inertia effect of the moving mass. This is achieved by modelling the supporting structure as a simply supported beam and by using the method of Modal Superposition (MS). If the number of modes is high enough this model can be used to approximate the dynamics of multi-span structures as well, where the intermediate supports are modelled as spring elements with adequate high stiffness and damping. Both the simply supported beam and the two-span continuous beam are validated against experimental data.

For actuation, two different solutions are chosen in this study, first an electrodynamic shaker and secondly piezoelectric MFC actuators. For the beam-shaker model two numerical models are presented in section 2.2, a detailed representation in the frequency domain and a simplified first order model. Numerical simulations show the frequency response function (FRF) of the beam actuator structure. The first-order model is validated against experimental deflection data.

In section 2.3 the numerical moving mass model is validated against an example from the literature. The difference to the more straightforward moving force model is demonstrated. It is shown for which speeds and mass ratios it is crucial to use the exact moving mass model presented.

The theoretical model of the 33-mode piezoelectric actuators followed by an experimental validation is presented in section 2.4. To the best knowledge of the author this is the first experimental study which utilises 33-mode macro fibre composites (MFC) to actuate a simply supported and a two-span continuous beam acted upon moving masses.

2.1 The Transverse Vibration of Single and Multi-Span Beams Subjected to Moving Masses

If the mass and especially the travelling speed of the moving load are high in relation to the structure, its inertia has to be considered and the moving force problem becomes a moving mass problem [2,26]. The supporting structure is modelled as an Euler-Bernoulli simply supported beam of mass per unit length ρA and flexural rigidity $E_b I$ [2,29,88,89]. It is subjected to the action of a mass m moving at constant speed v as illustrated in Figure 2.1. The speed v and the preload $N = mg$ of the mass m are assumed to be constant over the travelling time t at this stage. Further the friction between the moving mass and the beam is neglected and it is assumed that the beam vibrates only in the y -direction. It is also assumed that the mass does not lose contact with the beam structure.

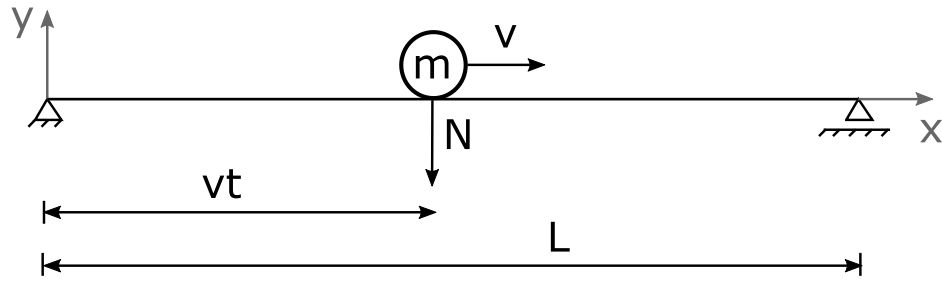


Figure 2.1. Model of a simply supported beam subjected to a moving mass m travelling with constant speed v .

With the Euler-Bernoulli beam approach, the equation of transverse motion $w(x,t)$ for this simple model is:

$$\rho A \frac{\partial^2 w}{\partial t^2} + c \rho A \frac{\partial w}{\partial t} + E_b I \frac{\partial^4 w}{\partial x^4} = - \left(N + m \frac{d^2 w_l}{dt^2} \right) \delta(x - vt) \quad (2.1)$$

where w_l is defined as the vertical displacement of the moving mass m . The term, $c \rho A$ describes the damping of the beam. The following relation holds for the Dirac delta function $\delta(x - x_0)$ [2,8]:

$$\int_0^L f(x)\delta(x - x_0)dx = f(x_0) \quad (2.2)$$

$\delta(x - vt)$ concentrates the force at the moving coordinate vt . On the right-hand side of equation (2.1) the mass is located at a moving coordinate, which is the instantaneous spatial location vt . With the assumption, that the mass does not separate from the beam during the horizontal travel the velocity and its derivatives are:

$$w_l(t) = w(x, t), \quad \frac{dw_l}{dt} = \frac{\partial w}{\partial t} + v \frac{\partial w}{\partial x}, \quad (2.3)$$

$$\frac{d^2 w_l}{dt^2} = \frac{\partial^2 w}{\partial t^2} + 2v \frac{\partial w}{\partial t} \frac{\partial w}{\partial x} + v^2 \frac{\partial^2 w}{\partial x^2}$$

The equation of motion becomes:

$$\rho A \frac{\partial^2 w}{\partial t^2} + c \rho A \frac{\partial w}{\partial t} + E_b I \frac{\partial^4 w}{\partial x^4} + m \left(\frac{\partial^2 w}{\partial t^2} + 2v \frac{\partial w}{\partial t} \frac{\partial w}{\partial x} + v^2 \frac{\partial^2 w}{\partial x^2} \right) \delta(x - vt) \quad (2.4)$$

$$= -N \delta(x - vt)$$

The solution of equation (2.4) can be found using the method of separation of variables also called modal superposition as:

$$w(x, t) = \sum_{n=1}^{\infty} \psi_n(x) q_n(t) \quad (2.5)$$

where $q_n(t)$ is the modal coordinate for the n -th mode $\psi_n(x)$ of the undamped simply supported beam, which is (see Appendix 1):

$$\psi_n(x) = \sin\left(\frac{n\pi x}{L}\right); \quad (n = 1, 2, 3, \dots) \quad (2.6)$$

Other boundary conditions could be used easily as well, for example a fixed-free beam, relevant for aerodynamic loads. However the orthogonality condition for equation (2.6) is:

$$\int_0^L \psi_i(x) \psi_j(x) dx = \delta_{ij} \frac{L}{2} \quad (2.7)$$

and

$$\int_0^L \psi_i''''(x)\psi_j(x)dx = \delta_{ij} \frac{L}{2} \beta_i^4, \quad (i, j = 1, 2, 3 \dots), \quad (2.8)$$

Where δ_{ij} is the Kronecker delta index ($\delta_{ij} = 1$ if $i = j$, $\delta_{ij} = 0$ if $i \neq j$), β_i is a constant depending on the boundary condition of the beam, (see Appendix 1 and [89]). The dashes in ψ'''' define the total derivative with respect to x and the dot in \dot{q} defines the total time derivative in the following. Substituting equation (2.5) in equation (2.4) multiplying the resultant with $\psi_i(x)$ and integrating it over the beams length L results in:

$$\begin{aligned} \rho A \int_0^L \psi_i \psi_j dx \ddot{q}_j + \rho A c \int_0^L \psi_i \psi_j \dot{q}_j + E_b I \int_0^L \psi_i \psi_j'''' q_j \\ + m \sum_{n=1}^{\infty} \psi_n(vt) \psi_i(vt) \ddot{q}_n + 2vm \sum_{n=1}^{\infty} \psi_n'(vt) \psi_i(vt) \dot{q}_n \\ + mv^2 \sum_{n=1}^{\infty} \psi_n''(vt) \psi_i(vt) q_n = -N \psi_i(vt); \quad (i, j = 1, 2, 3, \dots) \end{aligned} \quad (2.9)$$

On the right hand side the property of equation (2.2) of the dirac delta function is used. Including the boundary conditions (2.7) and (2.8) leads to:

$$\begin{aligned} \frac{\rho AL}{2} \delta_{ij} \ddot{q}_j + \frac{\rho AcL}{2} \delta_{ij} \dot{q}_j + \frac{E_b I \beta_i^4 L}{2} \delta_{ij} q_j + m \sum_{n=1}^{\infty} \psi_n(vt) \psi_i(vt) \ddot{q}_n \\ + 2vm \sum_{n=1}^{\infty} \psi_n'(vt) \psi_i(vt) \dot{q}_n + mv^2 \sum_{n=1}^{\infty} \psi_n''(vt) \psi_i(vt) q_n \\ = -N \psi_i(vt); \quad (i, j = 1, 2, 3, \dots); \end{aligned} \quad (2.10)$$

Writing equation (2.9) in the state space representation for a mass moving at constant speed in the time t within the interval $[0, t_f]$ with $t_f = L/v$ results in

$$(\mathbf{M} + \Delta\mathbf{M}(t))\ddot{\mathbf{q}} + (\mathbf{D} + \Delta\mathbf{D}(t))\dot{\mathbf{q}} + (\mathbf{K} + \Delta\mathbf{K}(t))\mathbf{q} = -N\boldsymbol{\psi}(vt) \quad (2.11)$$

with

$$\begin{aligned} \mathbf{M} &= \rho A \int_0^L \boldsymbol{\psi}(x) \cdot \boldsymbol{\psi}(x) dx; \\ \mathbf{D} &= \rho AC \int_0^L \boldsymbol{\psi}(x) \cdot \boldsymbol{\psi}(x) dx; \\ \mathbf{K} &= EI \int_0^L \boldsymbol{\psi}(x) \cdot \boldsymbol{\psi}''''(x) dx \end{aligned} \quad (2.12)$$

and

$$\begin{aligned} \Delta\mathbf{M}(t) &= m\boldsymbol{\psi}(vt)\boldsymbol{\psi}^T(vt); \\ \Delta\mathbf{D}(t) &= 2vm\boldsymbol{\psi}(vt)\boldsymbol{\psi}'^T(vt) \\ \Delta\mathbf{K}(t) &= mv^2\boldsymbol{\psi}(vt)\boldsymbol{\psi}''^T(vt) \end{aligned} \quad (2.13)$$

where $\boldsymbol{\psi}(vt)$ is the modal shape vector. $\mathbf{C} = \mathbf{diag}(2\zeta_1\omega_1, 2\zeta_2\omega_2, \dots, 2\zeta_i\omega_i)$ describes the modal damping. The diagonal matrix $\mathbf{diag}(a_{11}, a_{22}, \dots, a_{ij})$ is defined as $a_{ij} = 0$ if $i \neq j$. Mechanical engineering structures have damping ratios ζ in the range of $\zeta \cong 0.01 - 0.02$ [42]. Later ζ will be approximated by fitting the numerical model and the experimental deflection data. The time t_f represents the time the mass leaves the beam. From this instant of time, the beam vibrates freely and the system governing the motion is linear-time invariant. The system equations for $t > t_f$ changes from (2.11) to:

$$\mathbf{M}\ddot{\mathbf{q}} + \mathbf{D}\dot{\mathbf{q}} + \mathbf{K}\mathbf{q} = \boldsymbol{\psi}(x_a)f \quad (2.14)$$

where the initial conditions are the values of the states at the instant of time t_f . Figure 2.2 illustrates a two-span beam where a stream of masses of different weights is moving with

different speeds. The intermediate support can be represented by spring and damper elements. The span length is l .

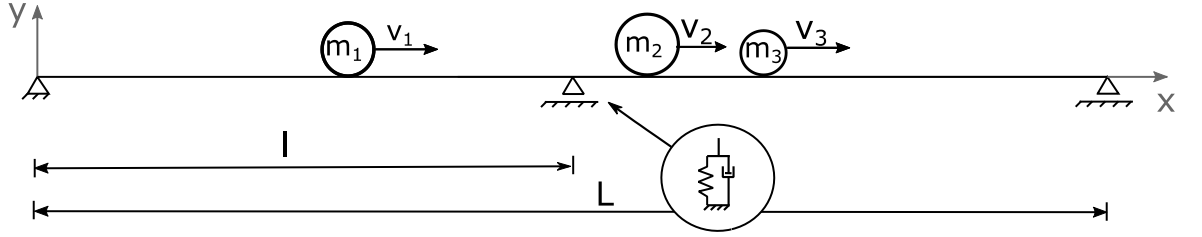


Figure 2.2. A stream of masses moving on a two-span beam, intermediate mid-span support modelled as a spring-damper element.

Considering the stream of n moving masses on the beam with multiple supports equation (2.11) changes to

$$\begin{aligned}
 (\mathbf{M} + \Delta\mathbf{M}_s(t))\ddot{\mathbf{q}} + (\mathbf{D} + \Delta\mathbf{D}_s(t) + \mathbf{D}_a)\dot{\mathbf{q}} + (\mathbf{K} + \Delta\mathbf{K}_s(t) + \mathbf{K}_a)\mathbf{q} \\
 = - \sum_{i=1}^n m_i g \boldsymbol{\psi}(x_i)
 \end{aligned} \tag{2.15}$$

with

$$\begin{aligned}
 \Delta\mathbf{M}_s(t) &= \sum_{i=1}^n m_i \boldsymbol{\psi}(v_i t) \boldsymbol{\psi}^T(v_i t); \\
 \Delta\mathbf{D}_s(t) &= \sum_{i=1}^n 2v_i m_i \boldsymbol{\psi}(v_i t) \boldsymbol{\psi}'^T(v_i t) \\
 \Delta\mathbf{K}_s(t) &= \sum_{i=1}^n m_i v_i^2 \boldsymbol{\psi}(v_i t) \boldsymbol{\psi}''^T(v_i t)
 \end{aligned} \tag{2.16}$$

The N_a supports of a multi span beam are modelled as spring damper elements at the location x_j .

$$\mathbf{K}_a = \sum_{j=1}^{N_a} k_j \boldsymbol{\Psi}(x_j) \boldsymbol{\Psi}^T(x_j)$$

$$\mathbf{D}_a = \sum_{j=1}^{N_a} c_j \boldsymbol{\Psi}(x_j) \boldsymbol{\Psi}^T(x_j)$$
(2.17)

The spring coefficient k_j and the damping coefficient c_j have to be chosen to be sufficiently high to represent the stiff supports of the multi span beam. For example Nikkhoo [90] defined the spring coefficient as $k_j = 10^5 \frac{EI}{l}$ without including additional damping c_j .

For long span beams the deceleration a_i of the mass must be considered as well. This decaying speed is defined as $v_{di} = v_i - a_i t$ and can be replaced with v_i in equation (2.16). Also, the mass location changes from $x_i = v_i t$ for constant speed to the quadratic function $x_i = v_i t + \frac{1}{2} a_i t^2$.

2.1.1 Approximation of Mode Shapes of Continuous Two-Span Beams

The equation of motion for the simply supported beam can be solved with the mode shape function described by equation (2.6). To solve the dynamic equation (2.15) for beams with multiple supports, the modes shape vector $\boldsymbol{\Psi}(x_i)$ for the beam with multiple supports is needed. The analytical derivation of this mode shapes is difficult. The mode expression varies with each span and the initial conditions for the next span depend on the previous span [35]. The analytical solution of the last span becomes more difficult with an increasing number of spans.

The modes of a continuous beam with multiple spans can be approximated by the modes of the beam without the supports. Yang [35] used, for his specific example, fourteen mode shapes of a simply supported beam to represent the first eight modes of a two-span

continuous beam. The accuracy of this approximated method is higher with a larger number of modes [91]. The error of the i -th natural frequency ω_i will be small if $i+1$ modes are used, see also Figure 2.4 where eight modes are used and the first seven modes are represented sufficiently accurately.

Considering a simply supported beam (Figure 2.2) with n springs representing the supports, and without the moving masses, the equation of motion can be written as [35,91]:

$$\ddot{\mathbf{q}}(t) + \mathbf{diag}(\bar{\omega}_1^2 \dots \bar{\omega}_m^2)\mathbf{q}(t) = - \sum_{i=1}^n k_i \bar{\Psi}(x_i) \bar{\Psi}(x_i)^T \mathbf{q}(t) \quad (2.18)$$

where $\bar{\omega}_m$ is the m -th natural frequency of the simply-supported beam without the springs and $\bar{\Psi}(x_i)$ is its vector of m mode shapes normalised with respect to the beam's mass per unit length $\bar{\psi}_j = \sqrt{\frac{2}{\rho AL}} \sin\left(\frac{j\pi x}{L}\right)$; ($j = 1,2,3, \dots, m$). $\mathbf{q}(t)$ is the vector of general coordinates.

Introducing the relationship:

$$q_j(t) = p_j e^{i\omega_j t}; \quad (j = 1,2,3, \dots, m) \quad (2.19)$$

Where p_j is a coefficient and ω_j is the j -th natural frequency of the simply supported beam with springs, one gets:

$$\left[\mathbf{diag}(\bar{\omega}_1^2, \bar{\omega}_2^2, \dots, \bar{\omega}_m^2) + \sum_{i=1}^n k_i \bar{\Psi}(x_i) \bar{\Psi}(x_i)^T - \mathbf{diag}(\omega_1^2, \omega_2^2, \dots, \omega_m^2) \right] \mathbf{p} = \mathbf{0} \quad (2.20)$$

Where \mathbf{p} is the $m \times 1$ vector containing m elements of p_j . After solving the eigenvalue problem of eq. (2.20), where $\mathbf{diag}(\omega_1^2, \omega_2^2, \dots, \omega_m^2)$ and \mathbf{p} are the unknown, one can obtain the modes of the n -span continuous supported beam as:

$$\psi_j(x) = \sum_{k=1}^m \bar{\psi}_k(x_i) p_k^{(j)} \quad (2.21)$$

where $p_k^{(j)}$ is the element of the eigenvector $\mathbf{p}^{(j)}$ corresponding to the eigenvalue ω_j^2 . This approximation method can be applied to a beam with any boundary condition with several supports. $\bar{\psi}_k$ would become the k -th mode shape corresponding to the end supports.

The analytical mode shapes and frequencies of the two-span continuous supported beam can be found by treating each span as an individual beam and applying appropriate boundary conditions [88]. The natural frequencies are:

$$\omega_i = \sqrt{\frac{EI}{\rho A}} \left(\frac{\lambda_i}{l}\right)^2 \quad (2.22)$$

Where λ_i is determined by applying suitable boundary conditions to the i -th mode shape of the continuous beam. The analytical modal shapes of the first span ψ_{li} and of the second span ψ_{ri} can be expressed respectively as [88]:

$$\psi_{li}(x) = \sin\left(\frac{\lambda_i}{l}x\right) - \left(\frac{\sin(\lambda_i)}{\sinh(\lambda_i)}\right) \sinh\left(\frac{\lambda_i}{l}x\right), x \in [0, l], \quad i = 1, 2, 3 \dots \quad (2.23)$$

$$\psi_{ri}(x) = A_2 \sin\left(\frac{\lambda_i}{l}x'\right) + B_2 \left[\cos\left(\frac{\lambda_i}{l}x'\right) - \cosh\left(\frac{\lambda_i}{l}x'\right)\right] + C_2 \sinh\left(\frac{\lambda_i}{l}x'\right), \quad (2.24)$$

$$x' = \left(x - \frac{l}{2}\right), \in [0, l]$$

with

$$A_{2i} = \frac{\sinh(\lambda_i) \cos(\lambda_i) - 2 \sin(\lambda_i) \cosh(\lambda_i) + \sin(\lambda_i) \cos(\lambda_i)}{\sinh(\lambda_i) - \sin(\lambda_i)}$$

$$B_{2i} = \sin(\lambda_i)$$

$$C_{2i} = \cos(\lambda_i) - \frac{\sin(\lambda_i)}{\sinh(\lambda_i)} \cosh(\lambda_i) - A_{2i}$$

The non-dimensional parameters λ_i can be calculated by applying the boundary conditions of the continuous beam to eq. (2.23) and eq. (2.24). Table 2.1 displays these parameters for the first eight modes for a continuous beam with two equal spans.

Table 2.1. Non-dimensional parameters λ_i for two equal span continuous beams.

Mode	1	2	3	4	5	6	7	8
λ	3.1416	3.9266	6.2832	7.0686	9.4248	10.2102	12.5664	13.3518

The analytical method is of higher complexity than the approximated method, which leads to higher computational cost. Also, the approximated method is much easier applicable to continuous beams with more than two spans.

To verify the accuracy of the approximated method a simply supported beam with one equidistant support shown in Figure 2.3 is considered. The span length is defined as $l = 0.6$ m.

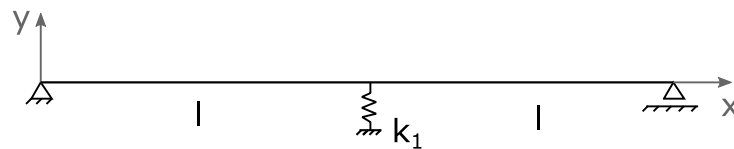


Figure 2.3. Simply supported beam with equal span length l and one centered spring support.

The parameters of the numerical model are defined, as flexural rigidity $EI = 12.11 \text{ Nm}^{-2}$ and $\rho A = 0.5411 \text{ kgm}^{-1}$. These are the parameters of the experimentally verified structure used later in section 2.1.3. Eight modes are used for the approximated method. Figure 2.4 illustrates the comparison of the first eight normalised mode between the approximated method and the analytical exact method. It is noticed that modes 1, 2, 3, 5 and 7 can be approximated with very high accuracy. Modes 4 and 6 have a slight difference between the analytical and the approximated method. Mode 8 cannot be approximated in a proper way.

Table 2.2 displays a comparison of the natural frequencies obtained by the analytical method and the approximate method. If one takes out the obviously faulty result for mode 8 in the approximated method the other highest errors are found for mode 4 and 6. These are 1.06% and 2.43 % respectively and may be considered to be acceptably low. In the numerical calculation, the error of the last mode should be taken care of. The influence on the structural responses is lower for higher modes. A compromise must be found between using enough modes to achieve sufficient accuracy while maintaining an acceptable computational cost.

In the following section, experimental results will be used to validate the mathematical model.

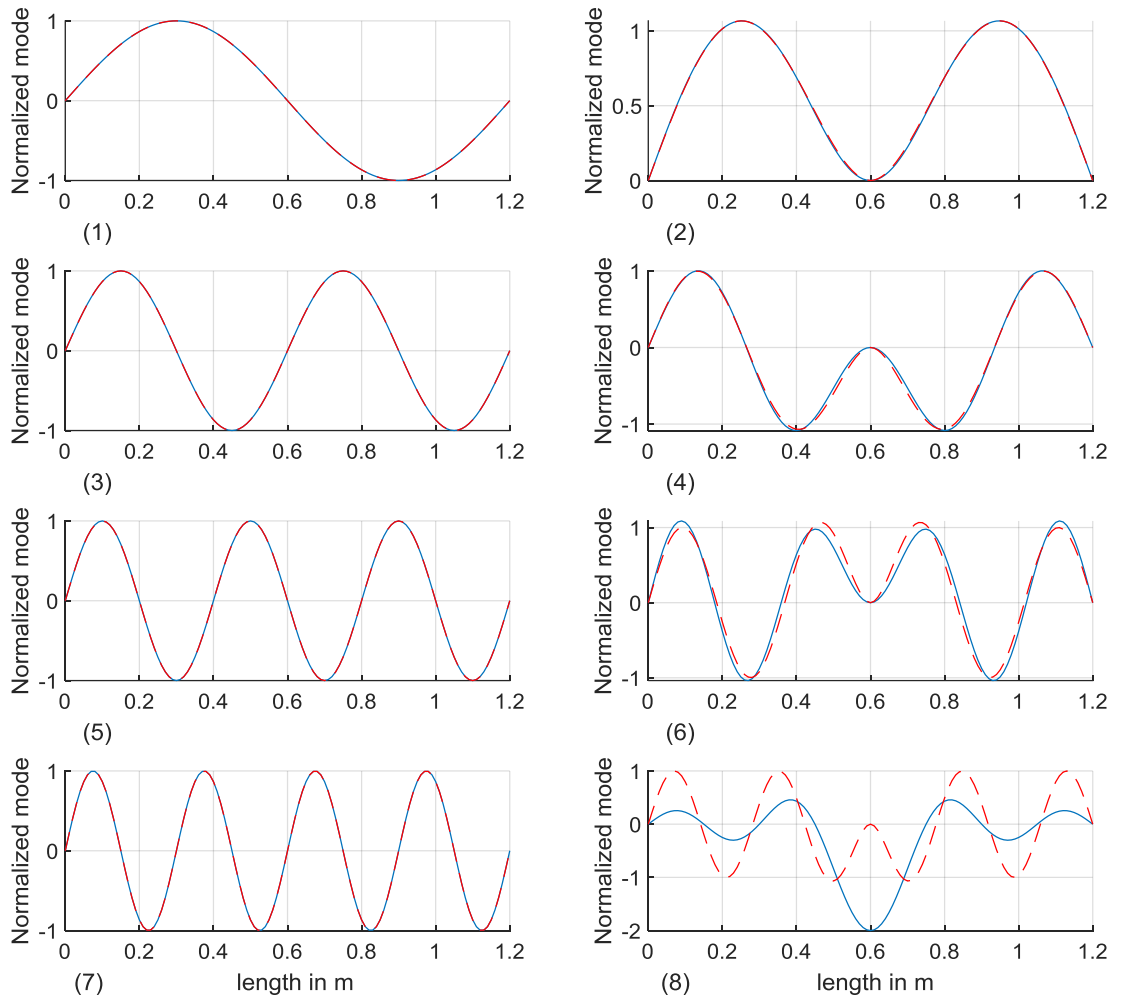


Figure 2.4. Comparison of the first eight modes of the two-span continuous beam approximated (blue continuous) and calculated analytical (red dashed).

Table 2.2. Comparison of the natural frequencies of the analytical method and the approximated method.

Mode	1	2	3	4	5	6	7	8
Analytical f	20.387	31.849	81.550	103.212	183.488	215.343	326.2	368.249
Approx. f	20.387	31.951	81.550	104.304	183.487	220.577	326.198	100660
Error in %	0.00	0.322	0.00	1.06	0.00	2.43	0.00	273240

2.1.2 Experimental Validation of the Simply Supported Beam under Moving Loads

Figure 2.5 shows the first experimental set-up. Different steel balls with known masses m are accelerated by a ramp and move over the simply supported beam structure at nearly constant speed. The geometrical characteristics of the aluminium beam are: span length $L = 0.6$ m and cross section $A = 0.06$ m \times 0.002 m. By adding polymer guiding rails, the flexural rigidity and the damping coefficient are increased. A schematic illustration of the entire experimental set-up is shown in Figure 2.6. Three laser displacement sensors (LDS) measure the deflection at $x_{s1} = 0.15$ m, $x_{s2} = 0.25$ m and $x_{s3} = 0.35$ m. At x_{s1} an LDS Micro-Epsilon optoNCDT 1600-4 is installed. LDS optoNCDT 1710-10 sensors are located at x_{s2} and x_{s3} . The last number of the part numbers denotes the measurement range in mm . The placement of sensors at the mode nodes is avoided. The data acquisition and control are accomplished in National Instruments software LabView on a CompactRio (or cRIO) embedded controller, which is controlled by the Host-PC. For the validation there is no actuator added to the structure. For later experiments it will be connected to the structure at the location x_a . Two induction sensors located in the ramp detect when the masses pass and thus the exact velocity of each ball can be determined.

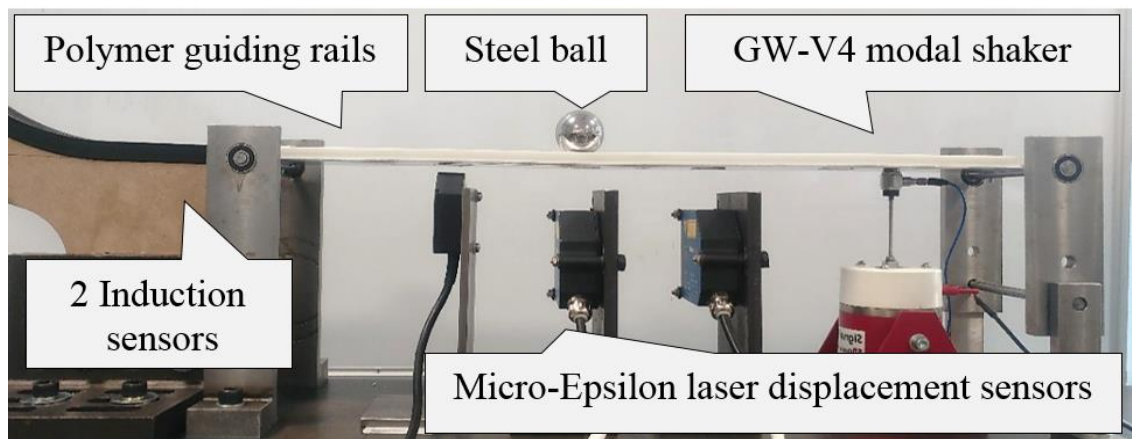


Figure 2.5. Experimental set-up, aluminium polymer beam subjected to a moving mass.

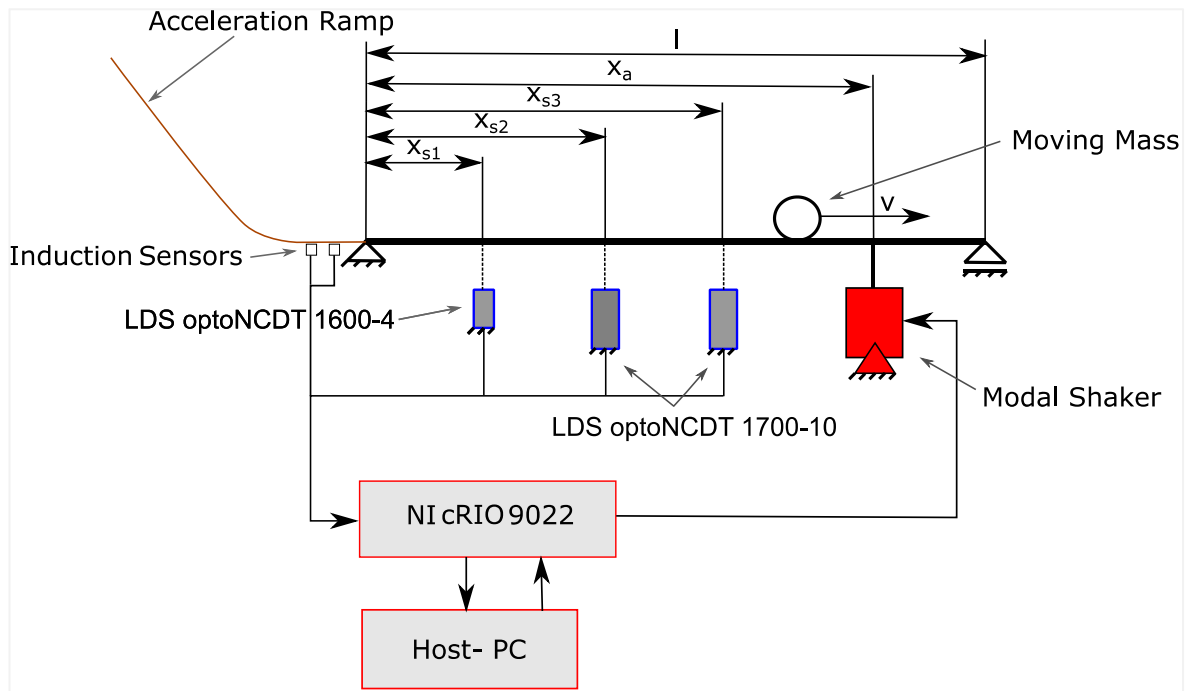


Figure 2.6. Schematic drawing of the whole experimental set-up of the simply supported beam actuated by an electrodynamic shaker

Figure 2.7 shows the deflection response $w(x_{s_i}, t)$, numerically estimated (blue line) at three sensor locations ($i = 1, 2, 3$) when 6 balls are launched along the beam, against the experimentally measured deflections (red line). The balls are collected in a container after they leave the structure. Between the time of 11 s and 14 s, two balls are moving simultaneously on the structure. For this case a higher deceleration is noticed, which might be because of the higher deflection of the beam and the resulting increased downhill force. The parameters of the numerical beam model are defined as mass per unit length $\rho A = 0.535 \text{ kgm}^{-1}$ and flexural rigidity $EI = 11.68 \text{ Nm}^{-2}$. Due to the polymer guiding rail the numerical model height is changed to 3.3 mm and a constant modal damping ratio $\zeta = 0.03$ is assumed throughout. The size of the damping rate determines how quickly the system returns to its equilibrium position after a disturbance. This value was chosen by adjusting the decaying behavior for the free vibration after mass is leaving the beam of the analytical model towards the one of this measured data. With these adjustments the deflections of the experimental data are in good agreement with the numerical model. Three modes are used in the numerical model. Numerical investigations in [26,32] have shown that the dynamic can be approximated using only the first three modes. No fundamental change in the deflection data is noticed as well in the example shown in Figure 2.7, when using a higher

number of modes. This has to be investigated from case to case. The structure equipped with the modal shaker and the two-span continuous beam structure might need a higher number of modes to be utilised in the numerical model for accurate results.

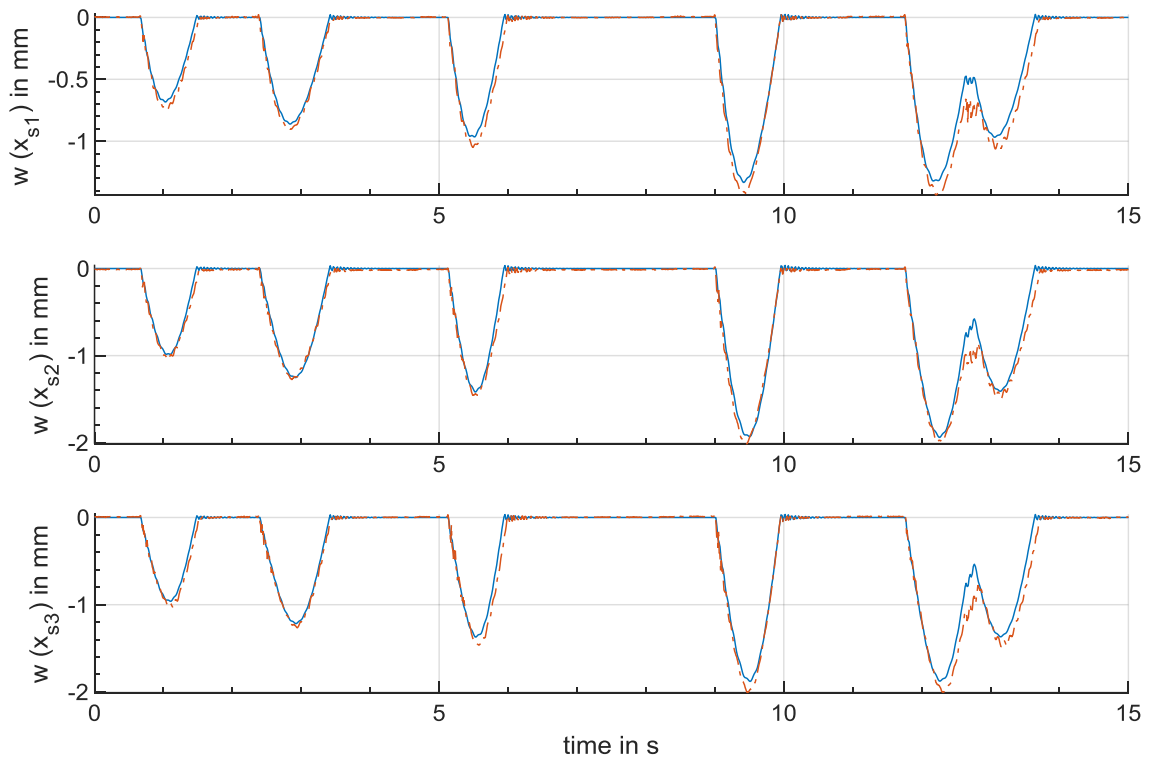


Figure 2.7. Time history of the deflections at sensor locations $x_{s1} - x_{s3}$ of the numerical model (blue continuous) and the experimentally obtained data (red dashed).

2.1.3 Experimental Validation of the Two-Span Continuous Moving Load Structure

Figure 2.8 portrays the experimental set-up for the two-span continuous beam. Figure 2.9 shows an additional schematic drawing of its the experimental set-up. For simplicity, the ramp, the Real-time controller and the Host-PC are not illustrated. Actuators and sensor are connected to the compactRio similar as shown in Figure 2.6. The span length is $l=0.6$ m, giving a total length of $L=1.2$ m. The sensor locations are $x_{s1}=0.25$ m, $x_{s2}=0.75$ m and $x_{s3}=0.85$ m. The cross section is defined as $A = 0.1 \text{ m} \times 0.002 \text{ m}$. $x_1 - x_4$ describe the start and ending locations of the active area of the piezoelectric actuators repectively, which are utilized for control later.

accurately. With less modes used the deflection response becomes noticeably different, see Figure 2.10.

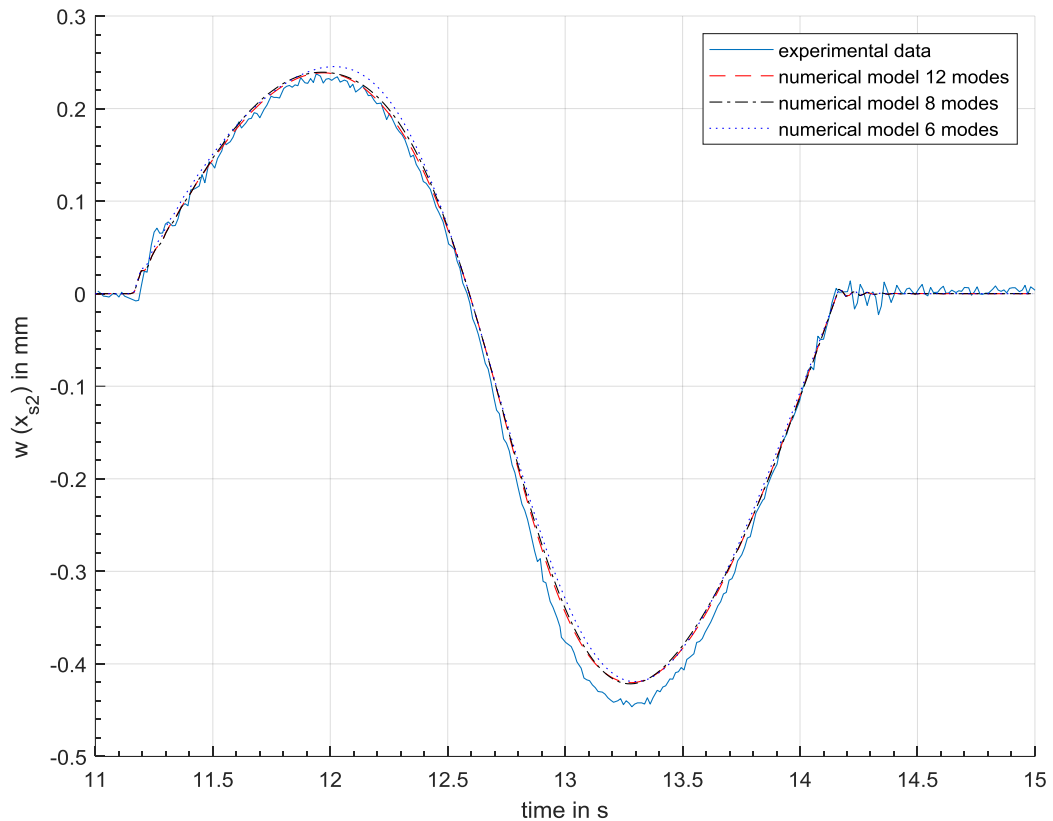


Figure 2.10. Time history of the deflection data $w(x_{s2})$ $m = 0.261$ kg moving along the two-span beam, comparison of the experimental results (blue continuous), numerical 12 modes (red dashed), numerical 8 modes (black dash dotted) and numerical 6 modes (blue dotted).

Figure 2.12 illustrates the deflection at the three sensor locations of the numerical model (red continuous) and of the experimentally obtained data when four masses m between 0.261 kg and 0.509 kg travel on the two-span beam. It is noticed that the deflections $w(x_{s2})$ and $w(x_{s3})$ measured experimentally at the second span have a higher deflection compared to the numerical data, especially between 91 s and 92 s when three masses travel on the beam at the same time.

This effect might be due to the construction of the supports, see Figure 2.8 and Figure 2.13. The supports consist of a long lever which might move the beam slightly downwards under higher loads. Also, the view of mass $m = 0.509$ kg travelling on the second span from 98 s-99.5 s shows a misalignment at all three sensor locations, which indicates that the whole

structure moved downwards by approximately 0.1 mm. Although smaller, this effect is also noticed for mass $m = 0.261$ kg in Figure 2.11 between 12.5 s and 14.2 s.

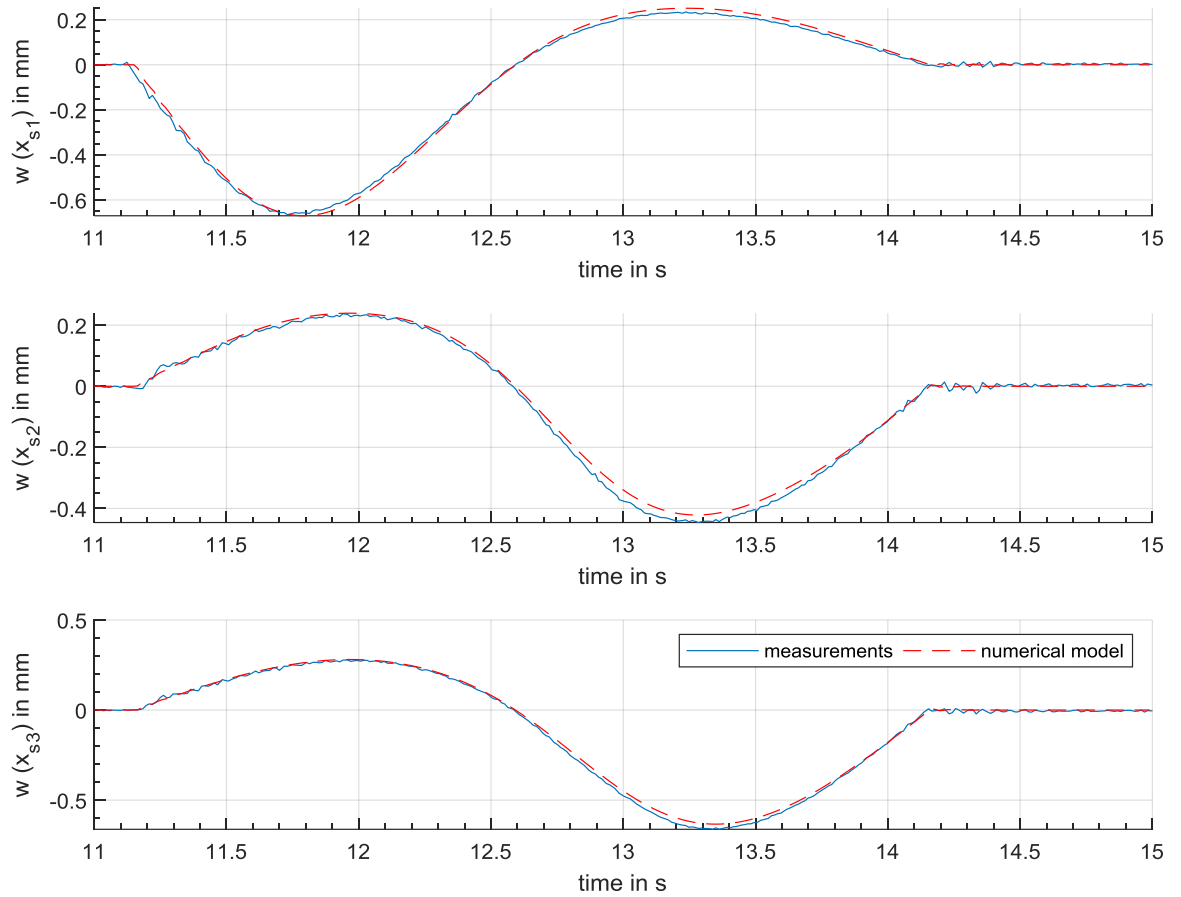


Figure 2.11. Time history of the deflections at the sensor locations $x_{s1} - x_{s3}$ of the numerical data (red dashed) and the experimental data (blue continuous) when a mass $m=0.261$ kg is travelling on the two-span beam.

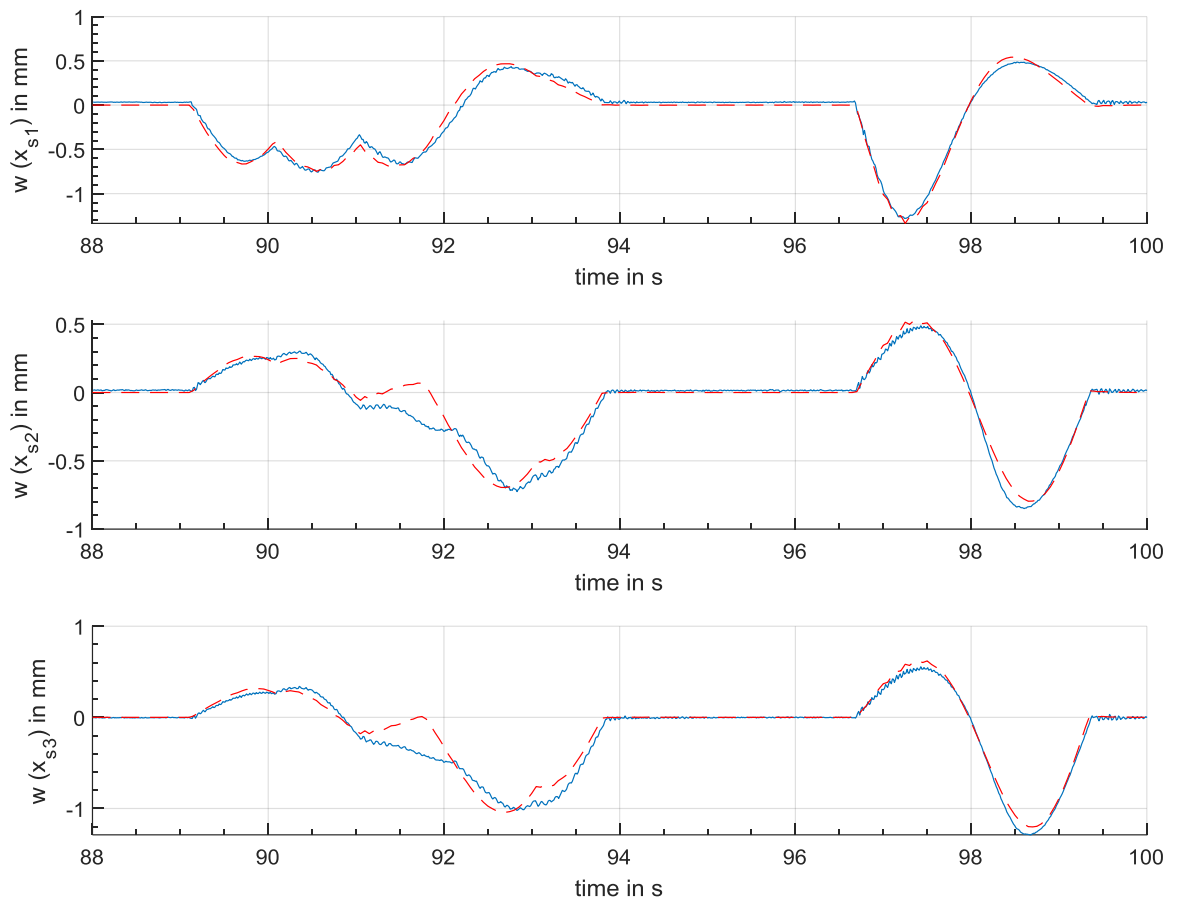


Figure 2.12. Time history of the deflections at sensor location x_{s1} - x_{s3} numerically (red dashed) and experimentally measured (blue continuous).

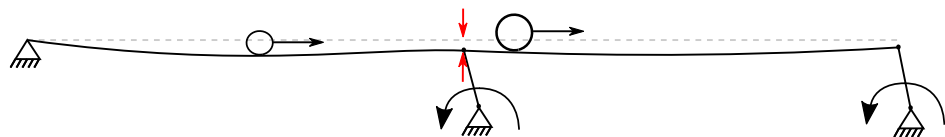


Figure 2.13. Two masses move on the two-span continuous beam, deflection error due to supports (red arrows).

In conclusion it can be said that especially for the one-span beam a good match between the experimentally data and the numerical model data is obtained. For the two-span beam a slight difference between numerically determined and experimentally measured deflection data is noticed at the second span. This might be due to the specific construction of the supports. In the following section, numerical models of an electrodynamic actuator are presented.

2.2 The Simply Supported Beam Controlled by an Electrodynamic Shaker

The dynamic equation of the structure controlled by k actuators at positions $x_{a1}, x_{a2}, \dots, x_{ak}$ is modified to

$$(\mathbf{M} + \Delta\mathbf{M}(t))\ddot{\mathbf{q}} + (\mathbf{D} + \Delta\mathbf{D}(t))\dot{\mathbf{q}} + (\mathbf{K} + \Delta\mathbf{K}(t))\mathbf{q} = - \sum_{i=1}^k \boldsymbol{\psi}(x_{ai})\mathbf{u}_i - N\boldsymbol{\psi}(vt) \quad (2.25)$$

The structure is actuated by an electrodynamic shaker. Although this shaker is mainly used for excitation of test objects with specified input signals in vibration testing applications like spectral and modal analysis, its wide availability in research institutions predestines them to be used as actuators in experimental active vibration control. Electromagnetic shakers are characterised by a high operational frequency bandwidth. However, they are not suitable for heavy duty applications. Although high test-input accelerations are possible at high frequencies, displacement and velocity excitations are limited to low and medium values [92]. Also the force performance is classified as low to intermediate [93]. In real applications hydraulic actuators with higher force actuation might be used.

In section 2.1.1 the precise model in the frequency domain for the specific beam shaker mass system is presented. It is followed by a numerical study in section 2.2.2. A simplified model, capable to be included in the state space representation is presented in section 2.2.3, followed by an experimental validation in section 2.2.4.

2.2.1 Numerical Model of a Simply Supported Beam Controlled by an Electrodynamic Shaker

Walters [94] studied the dynamics of an electrodynamic actuator, which reveals complex dynamics especially when it interacts with a flexible structure [95]. The electrical impedance of the shaker coil can be modelled as a resistor R in series with the inductor L_I , coupled to the shaker through back electromagnetic forces (EMF):

$$\frac{U(s)}{I(s)} = (R + s L_1) + K_v K_f \frac{H_0}{1 + \frac{H_0}{H_a}} \quad (2.26)$$

where K_v is the back EMF voltage constant and K_f is the electromagnetic force constant, see Figure 2.14. s represents the Laplace variable.

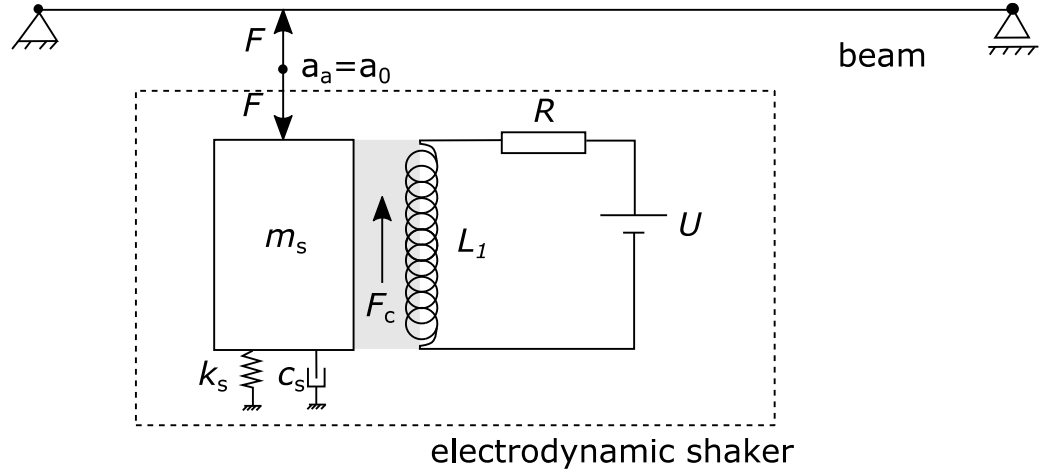


Figure 2.14. Schematic drawing of the elements of an electrodynamic shaker and the interaction with a simply supported beam.

The last term of eq. (2.26) consists of the mobility of the modified structure H_{mod} composed of the beam mobility H_0 and the electrodynamic shaker mobility H_a [93,96]

$$H_{mod} = \left(1 + \left(\frac{H_0}{H_a} \right) \right)^{-1} H_0 \quad (2.27)$$

The electrodynamic shaker mobility is defined as

$$H_a = \frac{A_a}{s} = \frac{s}{s^2 m_s + s c_s + k_s} \quad (2.28)$$

where m_s , c_s and k_s are the moving mass, the damping coefficient and the suspension stiffness of the shaker respectively. A_a is the shakers accelerance, thus equation (2.26) could easily be represented by accelerances or reacceptances as well [94]. The beam mobility H_0 is defined with the terms of equation (2.12) as,

$$H_0(s) = \boldsymbol{\Psi}(x_s) s(\mathbf{M}s^2 + \mathbf{C}s + \mathbf{K})^{-1} \boldsymbol{\Psi}(x_a)' \quad (2.29)$$

where x_s is the sensing location and x_a is the actuation location on the beam.

One approximation method of the moving load problem is to retain only the vertical component of the acceleration in equation (2.3), as suggested in [26,97]. To get an idea how the system behaves with an added mass m at a fixed location x_m the mass is defined as $\Delta\mathbf{M}(x_m) = m\boldsymbol{\Psi}(x_m)\boldsymbol{\Psi}^T(x_m)$. This mass is not moving in time. The transfer function can be written as

$$H_0(s) = \boldsymbol{\Psi}(x_s) s[(\mathbf{M} + \Delta\mathbf{M})s^2 + (\mathbf{C})s + (\mathbf{K})]^{-1} \boldsymbol{\Psi}(x_a)' \quad (2.30)$$

The description of the moving load problem in the frequency domain might be challenging as the terms $\Delta\mathbf{M}(t)$, $\Delta\mathbf{D}(t)$ and $\Delta\mathbf{K}(t)$ depend on time and the Laplace transformation must be performed on them as well. The overall FRF of the coil force over the input voltage is

$$H_s(s) = \frac{F_c(s)}{U(s)} = K_f \left(\frac{U(s)}{I(s)} \right)^{-1} \quad (2.31)$$

If one assumes the same accelerations will occur at the connection points of the actuator and the beam $a_a = a_0$, with the subscripts a and 0 describing the actuator and the structure respectively, the accelerations can be written in the frequency domain as

$$a_a(s) = A_a(s)(F_c(s) - F(s)) \quad (2.32)$$

$$a_0(s) = A_0(s)F(s)$$

where A_0 is defined as the beams accelerance in the driving point. From (2.32) the input force transferred to the beam F is related to the coil force F_c as [94,98,99]

$$\frac{F(s)}{F_c(s)} = \frac{A_a(s)}{A_a(s) + A_0(s)} \quad (2.33)$$

This results in the FRF of the force transmitted to the beam

$$H(s) = \frac{F(s)}{U(s)} = K_f \left(\frac{U(s)}{I(s)} \right)^{-1} \frac{A_a(s)}{A_a(s) + A_o(s)} \quad (2.34)$$

In the following section the FRFs of the electrodynamic shaker connected to a specific beam will be shown numerically.

2.2.2 Numerical Study of the Beam-Shaker-Moving-Mass Test Structure

In the previous section, the detailed transfer functions of the electrodynamic shaker system were presented. In addition, the actuator interacts with the flexible structure as shown in equation (2.31). In this section the FRF of the input force over the input voltage will be shown numerically for the utilised electrodynamic shaker and test structure.

In this study an electrodynamic shaker (Data Physics V4) is attached to the structure at $x_a = 0.5$ m. The sensor location may be $x_s = 0.5$ m. The mechanical and electrical parameter of this device are listed in Table 2.3. These parameters might change for a later application with a different amplifier setting.

Table 2.3. Parameter estimates for electrodynamic shaker (Data Physics V4) taken from [94].

Parameter	Value
Suspension stiffness, k_s	9700 Nm ⁻¹
Damping coefficient, c_s	0.55 Nsm ¹
Moving mass shaker, m_s	0.02 kg
Resistance, R	0.82 Ω
Inductance, L_1	5.0 × 10 ⁻⁵ H
Electromagnetic force constant, K_f	4.2 NA ⁻¹
Back EMF voltage constant, K_v	4.2 Vsm ⁻¹

The properties of the investigated Aluminium one-span beam were described in section 0. Figure 2.15 illustrates the Bode plot of the numerically calculated transfer function (2.38) of the input force with respect to the actuator voltage. Four modes are considered and no mass is added. Up to a frequency of 11 Hz the magnitude of $H(s)$ has a constant value of 2.5 N/V. At the frequencies 21 Hz, 84 Hz, 189 Hz and 340 Hz antiresonances, also called force drops, occur. A resonance is noticed at 27 Hz with a magnitude of 10 N/V.

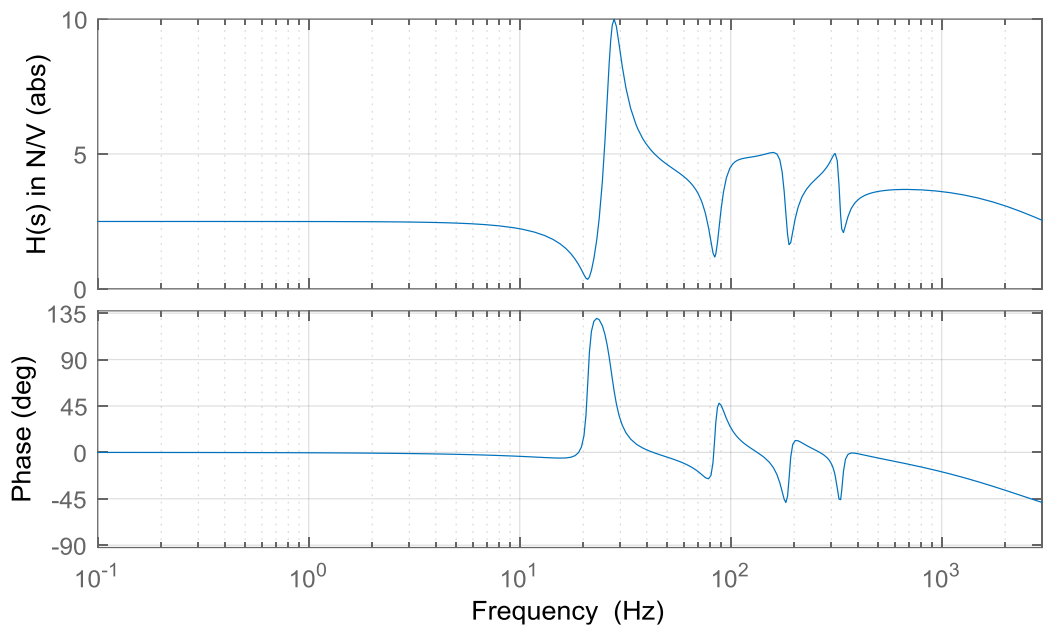


Figure 2.15. Magnitude of the FRF $H(s)$ of the input force/ input voltage (top) and phase angle (bottom).

Figure 2.16 shows the magnitude of the transfer function of the actuator-beam system with a mass of 0.5 kg added at the middle of the beam $x_m = 0.3\text{m}$. An additional antiresonance can be noticed at 13 Hz. Also the resonance at 27 Hz increased from 10 N/V to 32.5 N/V.

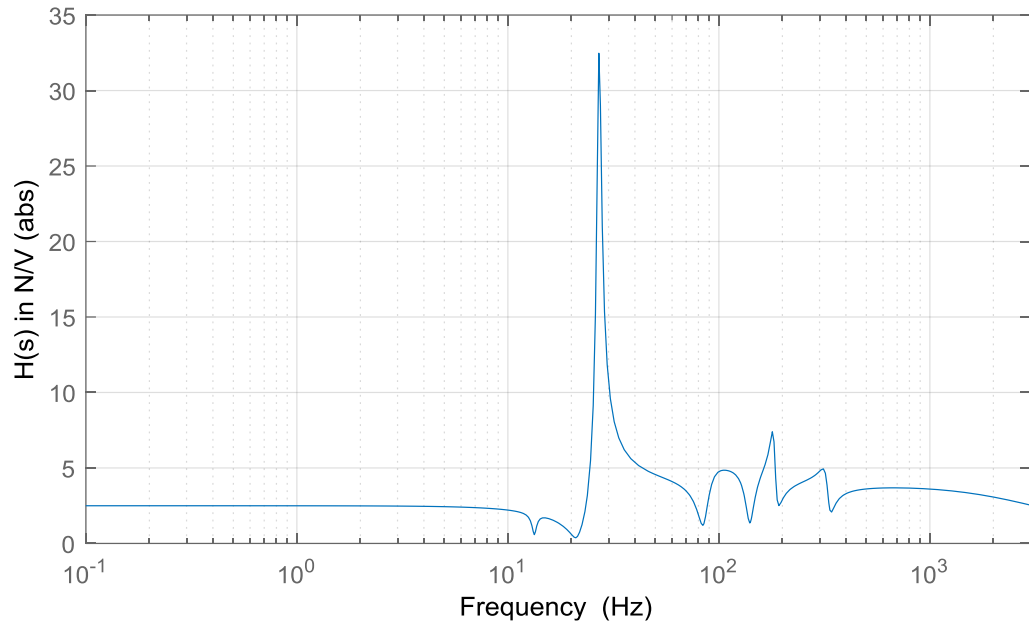


Figure 2.16. Magnitude of the FRF $H(s)$ with an added mass at $x_m = 0.3$ m.

Some antiresonances in Figure 2.15 and Figure 2.16 might be caused by the increased impedance (Figure 2.17) occurring at the systems resonances. The back-EMF term increases at the resonances in eq. (2.26). Note that in equation (2.31) the inverse of the FRF (2.26) is taken to calculate the FRF for the coil force.

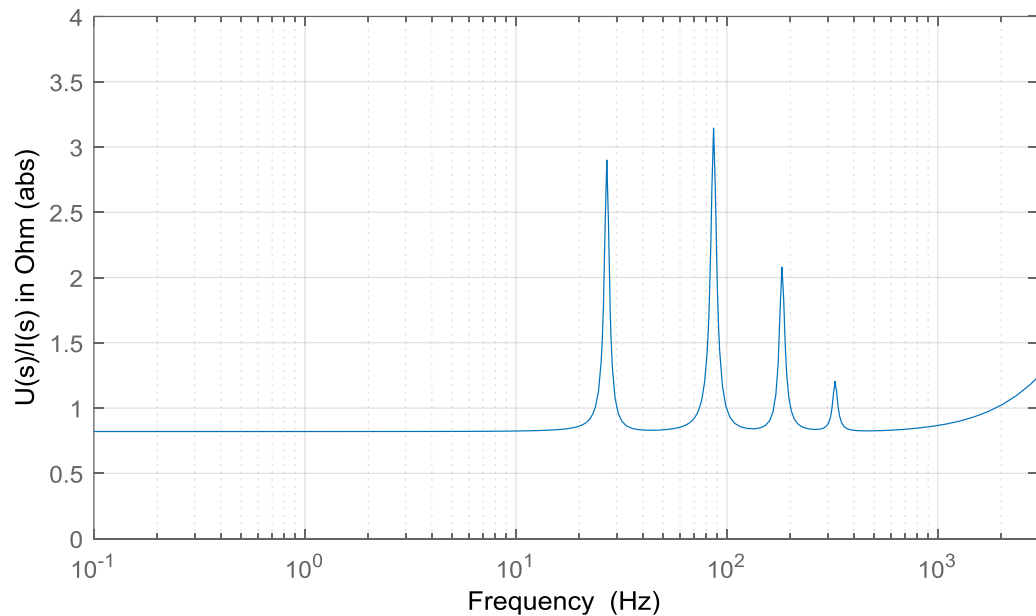


Figure 2.17. Bode diagram of the impedance of the electrodynamic shaker-beam system.

The resonance at 27 Hz in Figure 2.15 and Figure 2.16 is mainly caused by FRF (2.33) of the force transferred to the beam per coil force displayed in Figure 2.18. Especially, this resonance should be taken care of, to avoid instabilities in the control of the structure.

It might be advantageous to use a separate feedback control for the electrodynamic shaker to generate a precise input force above a frequency of 10 Hz.

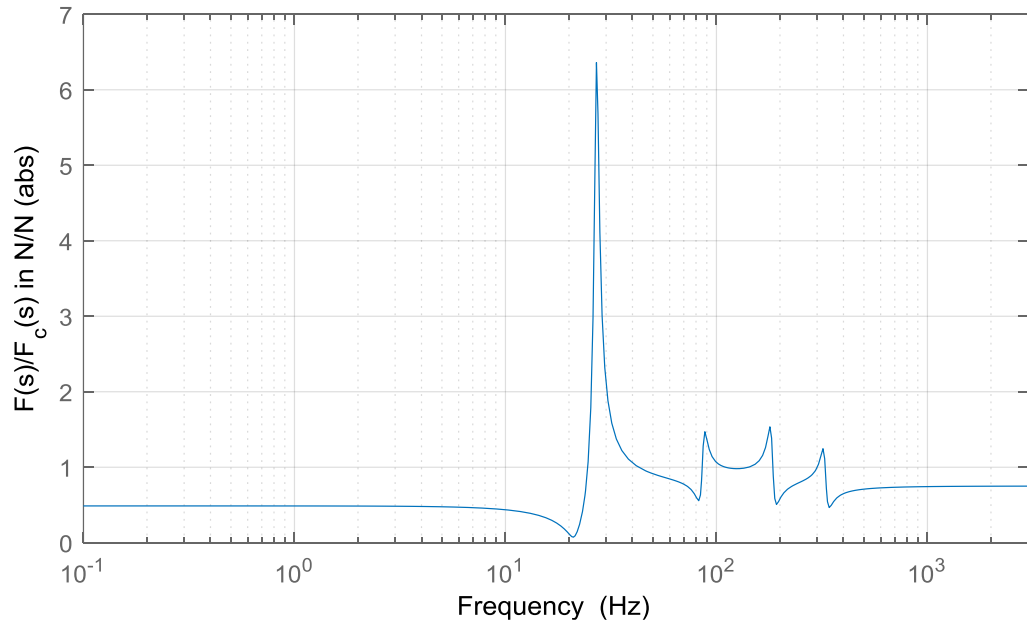


Figure 2.18. FRF of the force transmitted to the beam per coil force.

2.2.3 Simplified Model of the Simply Supported Beam Structure Controlled by an Electrodynamic Shaker

A straightforward dynamical model of the electrodynamic actuator is a first order state space system from the input voltage u to the output force f [40]:

$$\dot{z} = -\alpha z + \beta u \quad (2.35)$$

$$f = \gamma z$$

Figure 2.19 illustrates the bode plot of the system (2.35) with $\alpha = 10000$, $\beta=10000$ and $\gamma = 4.6$. The cutoff frequency is at 1591.5 Hz.

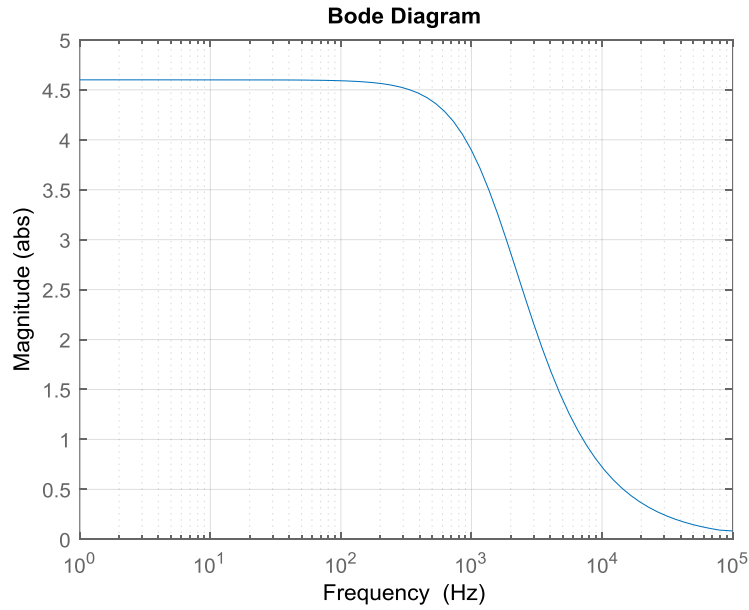


Figure 2.19. Bode diagram of the first-order shaker model.

The advantage of this approach is the possibility of integrating the shaker model in the moving-load structure model. In state-space representation, considering n modes the system matrices are:

$$\begin{aligned}
 \mathbf{A}_m(t) = & \begin{bmatrix} \mathbf{0}_{n \times n} & \mathbf{I}_{n \times n} & \mathbf{0}_{n \times 1} \\ -(\mathbf{M} + \Delta\mathbf{M}(t))^{-1}(\mathbf{K} + \Delta\mathbf{K}(t) + \mathbf{K}_a) & -(\mathbf{M} + \Delta\mathbf{M}(t))^{-1}(\mathbf{D} + \Delta\mathbf{D}(t) + \mathbf{D}_a) & \gamma(\mathbf{M} + \Delta\mathbf{M}(t))^{-1}\boldsymbol{\psi}(x_a) \\ \mathbf{0}_{l \times n} & \mathbf{0}_{l \times n} & -\alpha \end{bmatrix}; \\
 \mathbf{B}_m = & \begin{bmatrix} \mathbf{0}_{n \times 1} \\ \mathbf{0}_{n \times 1} \\ \beta \end{bmatrix}; \quad \mathbf{B}_f(t) = \begin{bmatrix} \mathbf{0}_{n \times 1} \\ -(\mathbf{M} + \Delta\mathbf{M}(t))^{-1}\boldsymbol{\psi}(vt) \\ 0 \end{bmatrix}; \quad (2.36)
 \end{aligned}$$

The state vector becomes $\mathbf{x}^T(t) = [\mathbf{q}(t) \dot{\mathbf{q}}(t) z(t)]$. Equation (2.35) can be viewed as an approximation of actual input force/input voltage model if the beam structure is much less mobile than the electrodynamic shaker. To illustrate this observation, Figure 2.20 shows the magnitude of the FRF obtained by equation (2.34) for the simply supported beam with the geometrical characteristics: height $h = 64$ mm, flexural rigidity of $EI = 1.022 \times 10^5$ Nm⁻¹ and $\rho A = 11.016$ kgm⁻¹. The length stays unchanged with $l = 0.6$ m. The magnitude is similar to the magnitude illustrated in Figure 2.19.

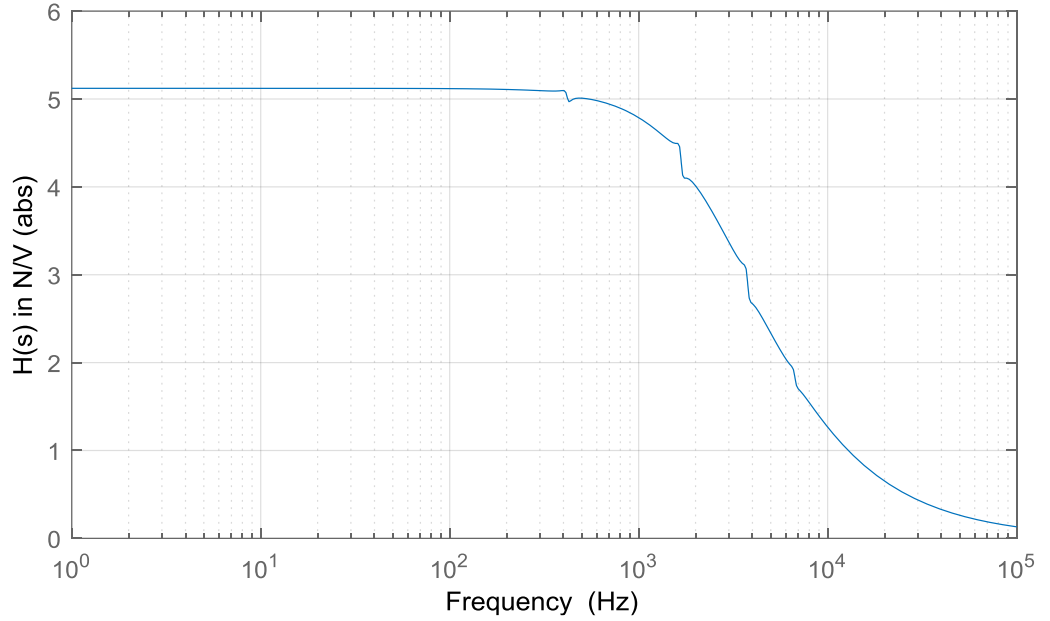


Figure 2.20. FRF input force over input voltage for rigid simply supported beam controlled by an electrodynamic shaker.

If the simplified model of equations (2.35) and (2.36) with a constant transfer value γ is used, this is appropriate for low frequencies of up to 10 Hz. In cases where the beam is significantly less mobile, then the shaker equation (2.33) and the magnitude in Figure 2.18 become one and the first order model is applicable for a wider frequency range.

2.2.4 Experimental Validation of the Beam-Shaker Structure

Figure 2.21 shows the numerically estimated (blue line) deflection response $w(x_{si}, t)$, at three sensor locations ($i = 1, 2, 3$) against the experimentally measured deflections (red line). In this experiment seven balls are launched along the beam by rolling from the acceleration ramp. For the last run two balls are moving at the same time on the structure. The parameters of the numerical beam model are defined as mass per unit length $\rho A = 0.535 \text{ kgm}^{-1}$ and flexural rigidity $EI = 11.68 \text{ Nm}^{-2}$. Due to the polymer guiding rail the height is changed to 3.3 mm and a constant modal damping ratio $\zeta = 0.03$ is assumed throughout. No control action is involved. The influence of the electrodynamic actuator is modelled as a spring-

damper system with a damping coefficient of $c_a = 80 \text{ Nsm}^{-1}$ and a stiffness of $k_a = 12000 \text{ Nm}^{-1}$. k_a was selected in that way, that the difference of the analytical and the experimental deflection data during the time the mass is on the beam is minimal. With the selected d_a the decay rate of the free vibration when the mass is leaving matches between the analytical and the experimental data.

The beam-shaker system was validated using an active shaker with and without the action of the moving mass. Therefore, the shaker's stiffness changes to $k_a = 3500 \text{ Nm}^{-1}$ and $\gamma = 4.6$ in equation (2.35). Numerical investigations have shown that the dynamics of the beam can be accurately approximated using only the first three modes.

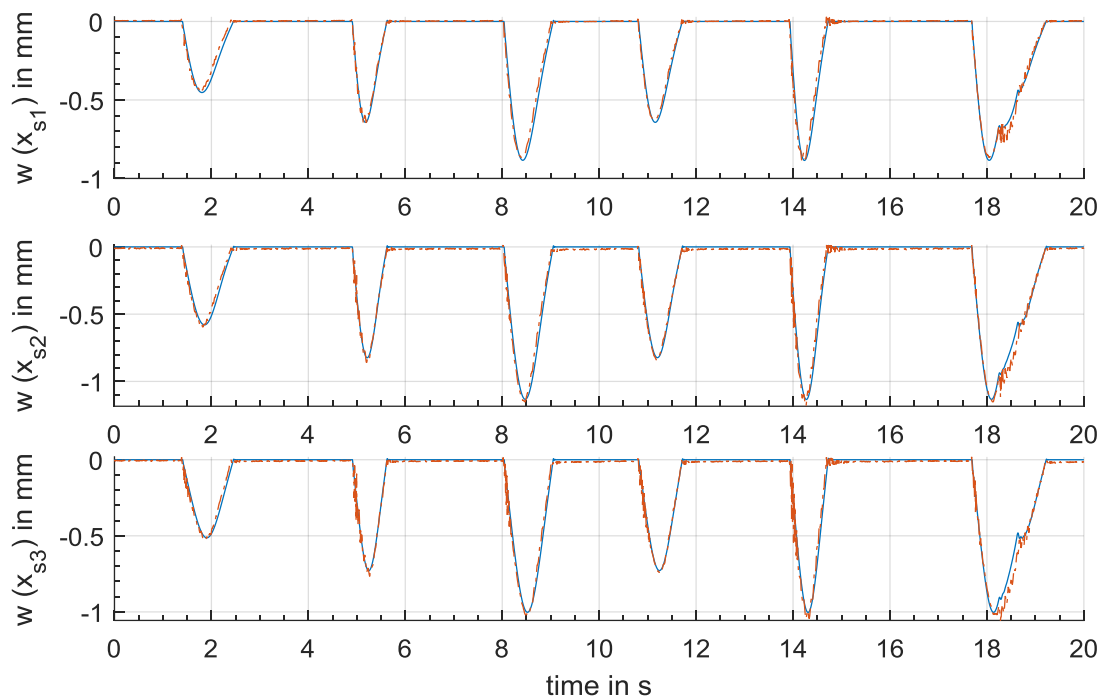


Figure 2.21. Experimental validation between the displacements of masses travelling at different speeds obtained by the numerical model (blue continuous) and the experimental measurements (red dashed).

Figure 2.22 shows a comparison between the experimental data and the numerical model simulation for time deflection response at sensors locations when four masses are launched at different speeds along the beam and the shaker's input is fed with a prescribed voltage. In this case the voltage supplied was a combination of sinusoidal functions of frequencies between 2 Hz and 4 Hz.

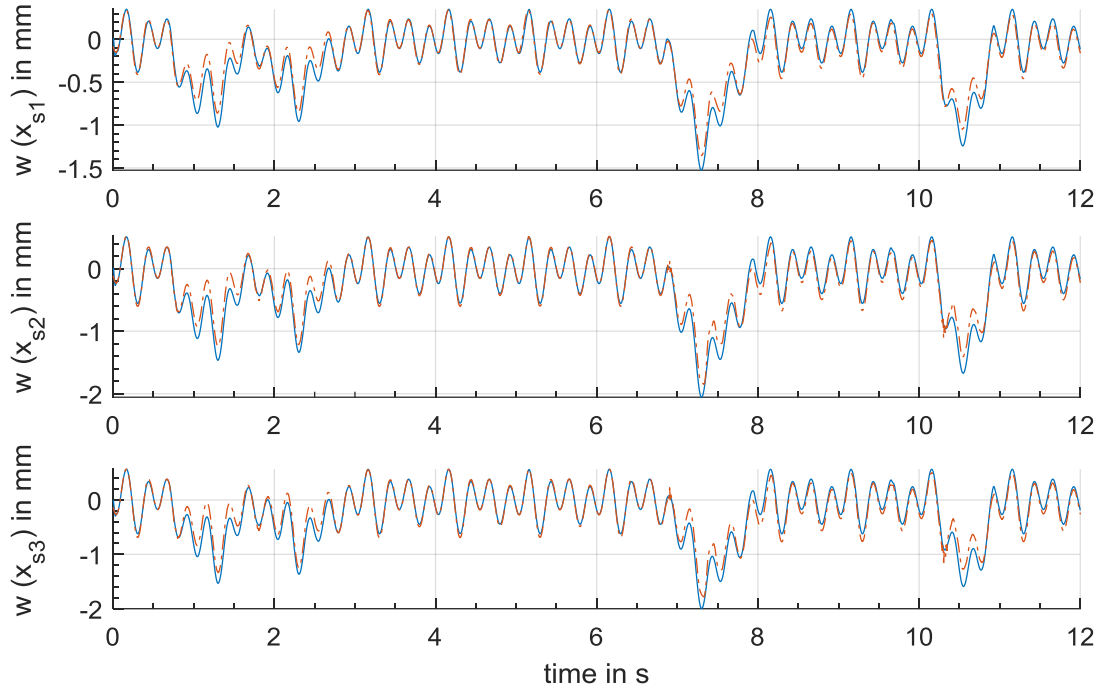


Figure 2.22. Validation of the beam mass system with an active electromagnetic shaker, numerical model (blue continuous), and the experimental measurements (red dashed).

2.3 Further Numerical Validation of the Moving Mass Model

In section 2.1 the exact moving mass model was derived to model the beams dynamics correctly at high mass/structure ratio and at high travelling speeds. A more straightforward model is the moving force model

$$\rho A \frac{\partial^2 w}{\partial t^2} + c \rho A \frac{\partial w}{\partial t} + EI \frac{\partial^4 w}{\partial x^4} = -N \delta(x - vt) \quad (2.37)$$

Here the inertia is neglected. The time-varying terms of equation (2.13) do not appear.

In a first step, the derived model will be validated against the numerical example presented in [26]. Further the necessity of using the exact moving mass model will be shown for a one-span and a two-span beam. In [26] a 60 m long uniform simply supported Euler Bernoulli

beam is considered. The flexural rigidity EI is equal to $5 \times 10^5 \text{ Nm}^2$, and the mass per unit length ρA is 1 kg/m . Figure 2.23 shows the exact same deflection over time at the mid-span as Nikkhoo et. al calculated in [26] for their moving load model and the exact moving mass model. The moving force model results in an amplitude up to three times higher in a 180° phase shift compared to the moving mass model after the load has left the beam. The time-varying terms of equation (2.13) depend on the moving loads weight and velocity. Also Nikkhoo et al. [26] state that any increase in weight and speed will increase the inertial effect. The lowest resonant speed, also called critical speed, is defined as [2]

$$v_{cr} = \frac{L\omega_1}{\pi} \quad (2.38)$$

with ω_1 the first fundamental frequency. Nikkhoo et al. define for their case another critical velocity $v'_{cr} = 0.4 v_{cr}$. Under this value the centripetal and Coriolis accelerations are negligible.

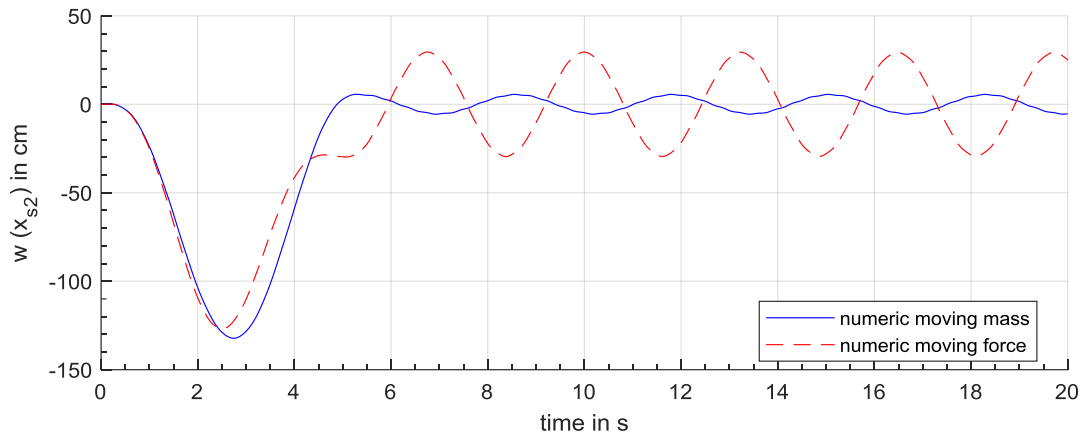


Figure 2.23. The time history of the midspan deflection under the effect of a moving mass and a moving load, 3 modes are used, $N=100\text{N}$, $v=11.1\text{m/s}$ (compare with figure 3b in [26]).

In the next step, the difference between the moving force model and the exact moving mass model for the studied structure will be shown numerically. The numerical model with its properties depicted in section 0 is used. The inactive shaker has a stiffness of $k_a = 12000 \text{ N/m}$. The first critical velocity is $v_{cr1} = 24.03 \text{ m/s}$. Figure 2.24 illustrates the deflection of the beam mass shaker system at sensor location $x_{s2} = 0.25 \text{ m}$. The actuator is located at $x_a = 0.5 \text{ m}$. The shaker's input is fed with a prescribed voltage of combined sinusoidal functions. The mass $m = 0.509 \text{ kg}$ moves with a speed of $v = 0.9 \text{ m/s}$. Although this speed is only $0.04 v_{cr}$, the travelling time has to be high enough to control the structure

appropriately in the later study. Consequently, only a very small difference between the moving mass and the moving force model of around 0.04 mm at the highest deflection is noticed.

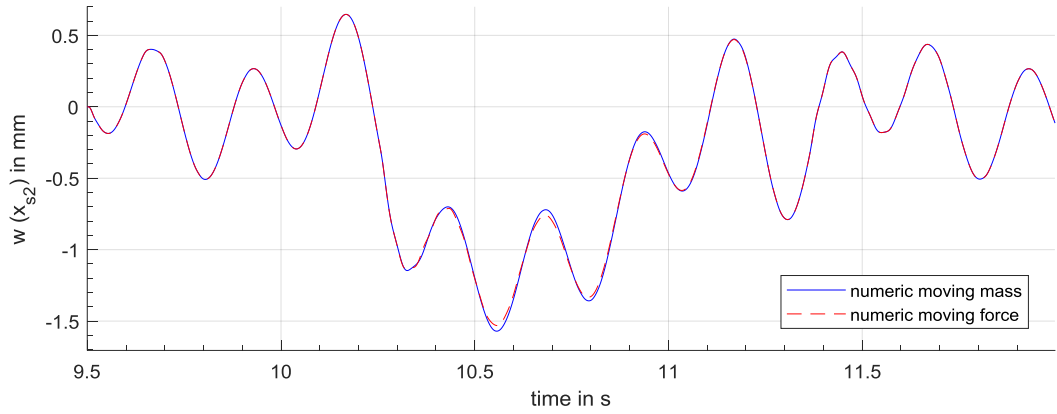


Figure 2.24. Numerical validation of the deflection of the beam mass system with an active electromagnetic shaker at sensor location x_{s2} , moving mass system (blue continuous) and numeric moving force system (red dashed).

In [26,35] the Dynamic Amplification Factor (DAF) is defined as the ratio of the maximum dynamic deflection to the maximum static deflection at the midspan. Figure 2.25 shows the DAF over the speed ratios v/v_{cr1} for two different masses $m_1 = 0.261$ kg (left) and $m_2 = 0.5$ kg (right). It can be noticed that only for a small speed ratio of up to $0.1 v/v_{cr1}$ the maximum deflection of the moving mass model and of the moving force model are similar. For higher velocities the correct moving mass model has to be used. The dynamic amplification factor increases to a certain value when the moving mass and the mass's velocity increase. For mass m_1 the DAF is nearly 2 at $0.5 v/v_{cr}$ for the moving mass model compared to a DAF = 1.6 at $0.7 v/v_{cr}$ for the moving force model. For mass m_2 the DAF reaches a value of 2.2 at $0.75 v/v_{cr1}$ for the moving mass model, where the moving force model is similar to the one of m_1 .

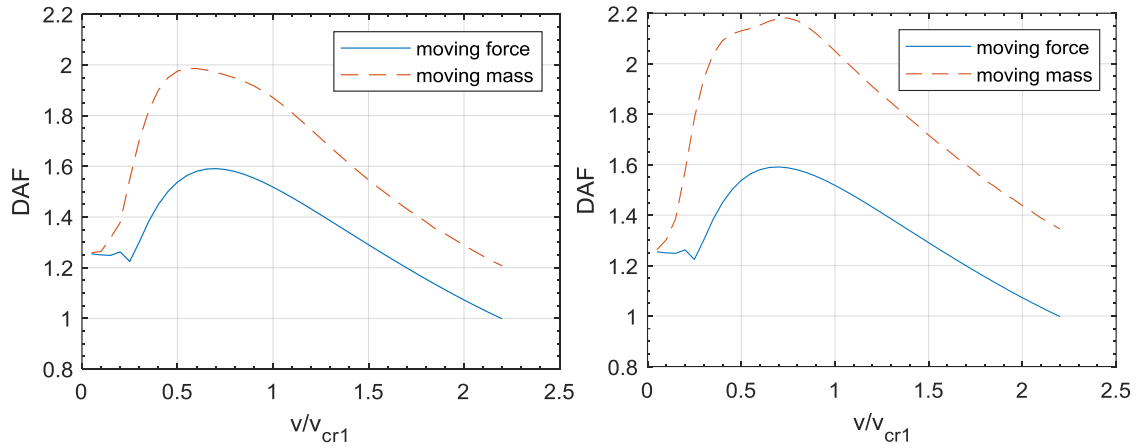


Figure 2.25. Dynamic amplification factor over the speed ratio for the moving force model (blue) and for the moving mass model (red dashed), for mass $m = 0.26$ kg, mass ratio $m/M = 0.81$ (left) and $m = 0.5$ kg, $m/M = 1.56$ (right).

Next, for the later experimentally investigated two-span structure the same comparison between moving force and moving mass model is undertaken. The structure has a total length of $L = 1.2$ m, EI and ρA stay unchanged. Following [36,100], the calculation of the mode shapes for a continuous two-span beam and with it of the critical velocity is more complicated compared to the simply supported beam. The first and second resonant frequency are at $\omega_1 = 128$ rad/s and $\omega_2 = 200.22$ rad/s respectively. Following [35] the calculation of the first critical velocity is similar to equation (2.38). The second mode exists in two cycles over the beam's length. The critical velocity is calculated as

$$v_{cr2} = \frac{L\omega_2}{2\pi} \quad (2.39)$$

$v_{cr1} = 48.95$ m/s and $v_{cr2} = 38.24$ m/s. It can be noticed in Figure 2.26 that for very low travelling speeds of $0.04 v_{cr}$ the moving force and the moving mass model give similar results. For higher travelling speeds of 3 m/s, which is around $0.08 v_{cr2}$ the inertia cannot be ignored for control of the dynamic response. Although the maximum deflection might be similar in Figure 2.26, the moving mass model's deflection comes with a phase lag, caused by the inertial effect of the mass acting on the beam. A comprehensive structural control approach has to include the inertial effect for the two-span beam structures when the mass is moving with a certain speed, in this case 3 m/s.

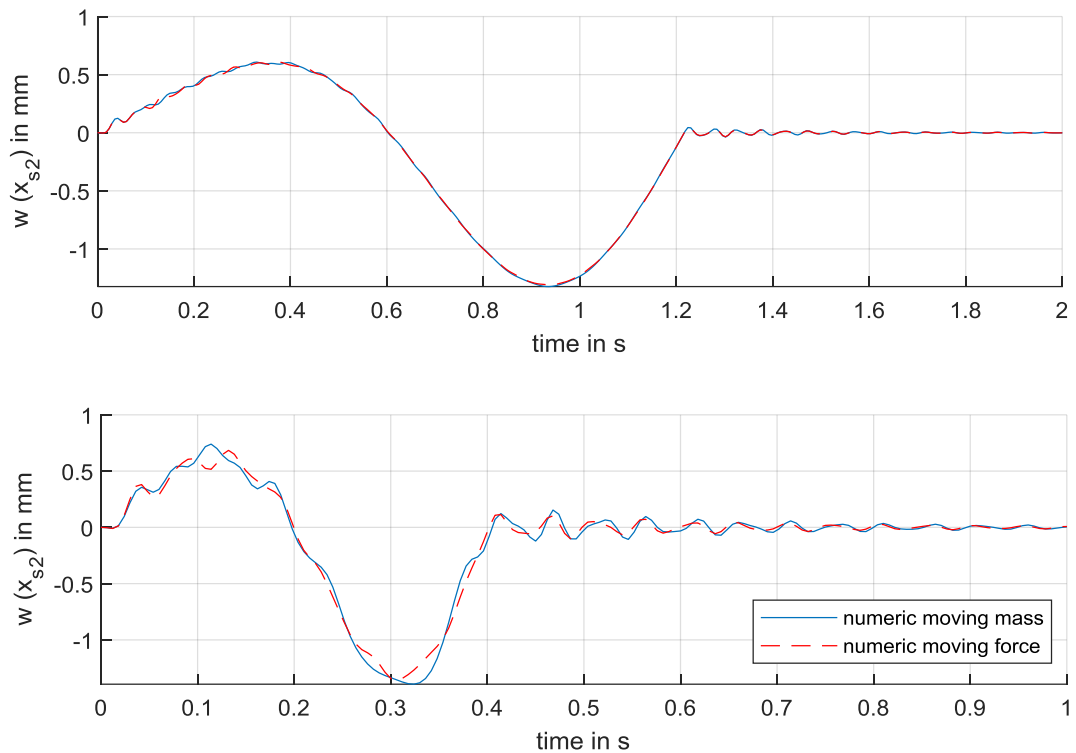


Figure 2.26. Time history of the deflection w at sensor location $x_{s2} = 0.75$ m of a two-span beam excited upon a moving mass (blue continuous) or moving load (red dashed) travelling with $v = 1.5$ m/s (top) and $v = 3$ m/s (bottom).

Yang shows in his moving force example [35] (figure 3.8) that this DAF can be 3.25 at the second span compared to 1.5 at a simply supported beam. This implies that for continuous multi-span beams the exact moving mass model has to be used even more. Figure 2.27 illustrates a higher DAF of 4.5 at $0.45 v/v_{cr1}$ at the second span midspan when a mass of 0.261 kg is travelling compared to 3.6 at the first midspan. A second peak of a DAF of 5 is noticed at $1.75 v/v_{cr1}$ at the second midspan. Again, the moving force model is applicable for small speed ratios v/v_{cr1} below 0.05.

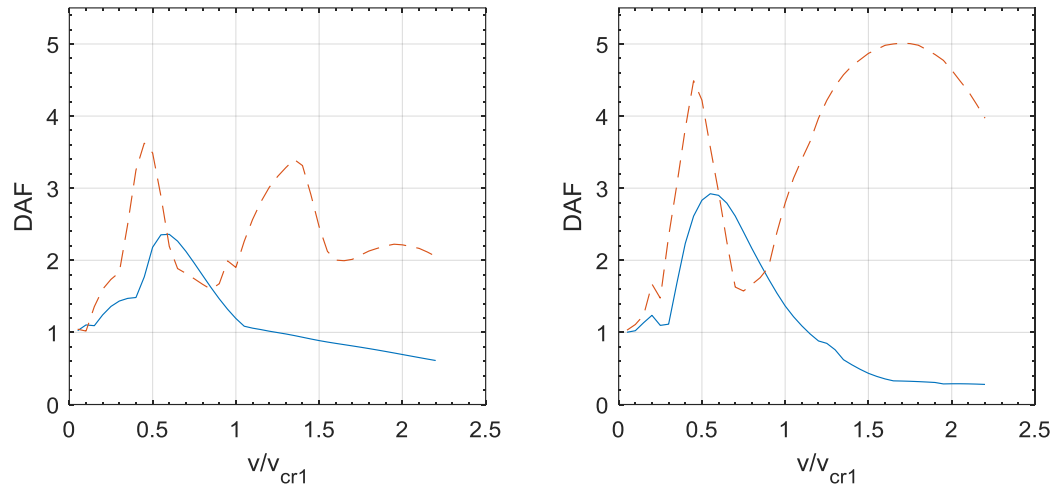


Figure 2.27. Comparison of the DAF at the midspan of the first span (left) and at the midspan of the second span (right) with mass $m = 0.261$ kg travelling utilising the moving force model (blue continuous) and of the moving mass model (red dashed).

In conclusion can be said, that for the studied simply supported beam the exact moving mass model has to be utilised for speed ratios higher than $0.1 v/v_{cr}$. The dynamic amplification increases with the increase of moving weight and with the higher travelling speeds. At the two-span beam a lag is noticed between the moving force and the moving mass model. This is the reason why, in order to control multi-span beams, the moving mass model has to be used even at lower speeds. The moving force model is applicable only for small speed ratios below 0.05. The use of a two-span continuous beam increases the dynamic amplification and by that the difference in results between the straightforward moving force model and the exact moving mass model.

2.4 Modelling of the Piezoelectric Actuator-Beam Structure

Piezoelectric actuators offer very attractive properties to active vibration control applications. They can transduce high forces or moments from a small geometry. Furthermore, they do not need a supporting structure and new actuators as the macro fibre composites (MFC) can be attached to complex geometries. A main drawback is that they operate at high voltages of about 1500 V, which makes the amplifiers costly for wider

applications [69]. In the following section, the dynamic model for the studied MFC actuators bonded to the simply supported beam structure is derived. In addition, the numerical model for the two-span beam actuated by two MFC actuators is presented. The numerical models will be validated against experimental results.

2.4.1 The Mathematical Model of the Piezoelectric Beam System

Piezoelectric actuators are used for bending actuation most often by the 31-mode with uniform electrodes [25,42]. In this study Macro fibre composites (MFC) are utilised. They use interdigitated electrodes (IDEs) with rectangular piezoelectric fibres. The 33-mode piezoelectric strain constant d_{33} is 50% to 100% larger than the d_{31} piezoelectric constant [66]. This offers much higher actuation capabilities compared to the d_{31} mode actuators. The two subscript numbers symbolize the polarization direction and the elongation direction respectively in Cartesian coordinates. Considering the area of the piezoelectric patch that extends on the beam from x_1 to x_2 (Figure 2.28), with its height much smaller than the beam height, $h_p \ll h$, following [42][66] the stress inside this area in the x -direction is defined as

$$\sigma_{33} = E_b \epsilon_{33} + E_p \epsilon_{33} - e_{33} E \quad (2.40)$$

Where E_b and E_p is the Young's Modulus of the beams and the piezoelectric material respectively, ϵ_{33} is the strain in the x - direction, $e_{33} = d_{33} E_p$ is the piezoelectric stress constant. In Figure 2.28 b_p is defined as the width of the piezoelectric patch. The electric field is defined by $E = \frac{V}{L_e}$, where V is the applied voltage and L_e is the distance between the electrodes. Figure 2.29 shows a schematic illustration of the piezoelectric actuator, which uses the d_{33} -effect. The polarization and the applied electric field coincide with the strain axis (the x -direction).

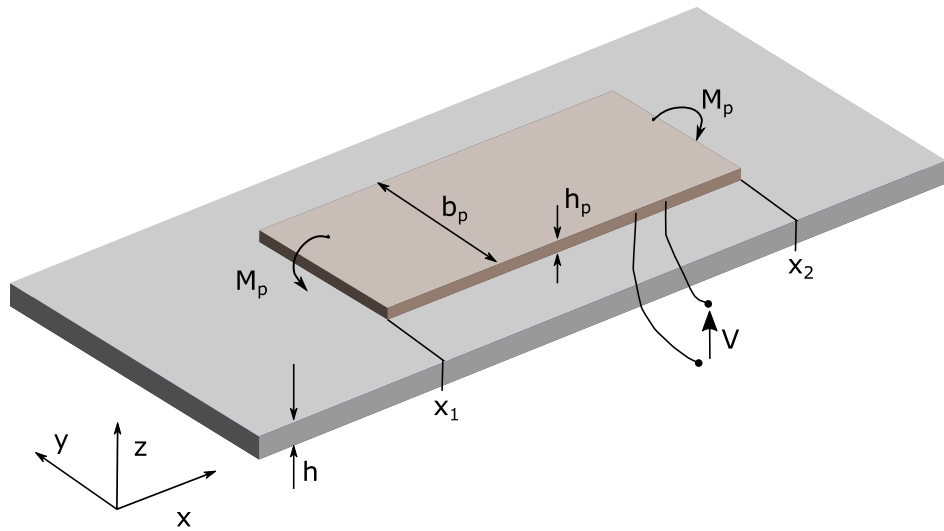


Figure 2.28. One piezoelectric actuator located on a beam structure.

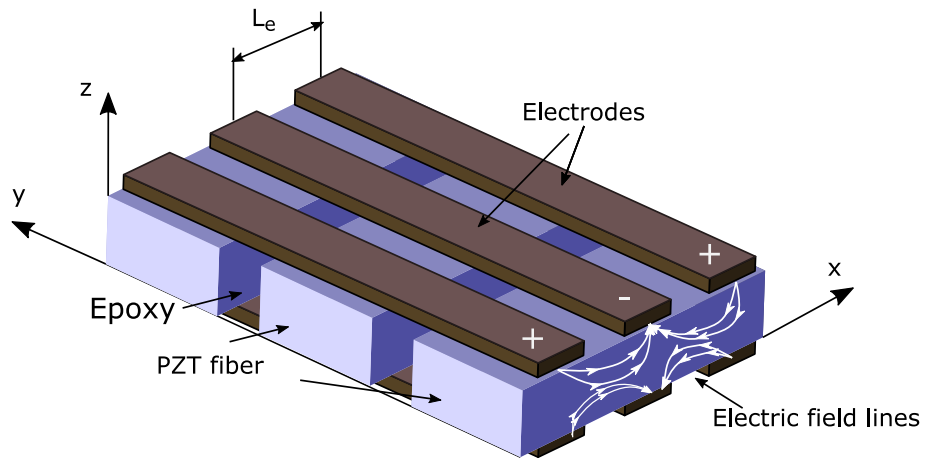


Figure 2.29. An MFC laminate using the 33-mode of piezoelectricity.

Following the Euler-Bernoulli assumption the axial deformation and the curvature are related by

$$\epsilon_{33} = -z \frac{\partial^2 w}{\partial x^2} \quad (2.41)$$

where z is the distance to the neutral axis. Inserting this into equation (2.40) and integrating over the cross section one gets the sum of moments

$$\begin{aligned}
M &= \int_A \sigma_{33} z dA = E_b I \frac{\partial^2 w}{\partial x^2} + E_p I_p \frac{\partial^2 w}{\partial x^2} + \int_A d_{33} E_p \frac{V}{L_e} \frac{h}{2} dA \\
&= E_b I \frac{\partial^2 w}{\partial x^2} + E_p I_p \frac{\partial^2 w}{\partial x^2} + d_{33} E_p \frac{V}{L_e} \frac{h}{2} h_p b_p
\end{aligned} \tag{2.42}$$

In (2.42) the constant moment M_p applied at the edges x_1 and x_2 of a piezoelectric film with constant width is defined as

$$M_p = d_{33} E_p \frac{V}{L_e} \frac{h}{2} h_p b_p = C_0 V \tag{2.43}$$

The equation of motion of a beam equipped with a piezo actuator can be written as

$$\begin{aligned}
\rho A \frac{\partial^2 w}{\partial t^2} + EI \frac{\partial^4 w}{\partial x^4} + \rho_p A_p \frac{\partial^2 w}{\partial t^2} + E_p I_p \frac{\partial^4 w}{\partial x^4} \\
= -M_p (\delta'(x - x_1) - \delta'(x - x_2))
\end{aligned} \tag{2.44}$$

where ρ_b, A_b, E_b, I_b are dedicated to the beam and ρ_p, A_p, E_p and I_p are dedicated to the piezo actuator. x_1 and x_2 are the start and end location of the actuator. Again, using the method of separation of variables of equation (2.5) multiplying by $\psi(x)$ and integrating over the beams length the solution of the ordinary differential equation can be found. The first derivative of the Dirac delta function has the property [31]:

$$\int_0^L \psi(x) \delta'(x - x_1) dx = -\psi'(x_1); \quad x \in (0, L) \tag{2.45}$$

As shown in the previous section 2.1 the solution can be written in matrix form as

$$(\mathbf{M} + \mathbf{M}_p) \ddot{\mathbf{q}} + (\mathbf{K} + \mathbf{K}_p) \mathbf{q} = -M_p c_p (-\Psi'(x_1) + \Psi'(x_2)) \tag{2.46}$$

with

$$\mathbf{M}_p = \rho_p A_p \int_{x_1}^{x_2} \Psi(x) \cdot \Psi(x) dx \quad (2.47)$$

$$\mathbf{K}_p = E_p I_p \int_{x_1}^{x_2} \Psi(x) \cdot \Psi''''(x) dx \quad (2.48)$$

c_p is an additional correction factor, which will be applied later to match the experimental deflection data with the deflection data obtained by the numerical model. It compensates possible model uncertainties. For example a perfect bonding is assumed between the actuator and the beam, but the utilized epoxy glue always has some flexibility and structural damping. That why not all of the bending moment might be transferred onto the beam. Also the utilized beam will be equiped with a guiding rail, which stiffens the structure. The deflection resulting from the actuator moment is reduced, compared to the deflection of a simular structure without the guiding rail. If n piezoelectric actuators are located on the beam equation (2.46) can be written as

$$(\mathbf{M} + \mathbf{M}_{pm}) \ddot{\mathbf{q}} + (\mathbf{K} + \mathbf{K}_{pm}) \mathbf{q} = \sum_{i=1}^n M_{pi} (-\Psi'(x_{2i-1}) + \Psi'(x_{2i})) \quad (2.49)$$

with

$$\mathbf{M}_{pm} = \sum_{i=1}^n \rho_{pi} A_{pi} \int_{x_{2i-1}}^{x_{2i}} \Psi(x) \cdot \Psi(x) dx \quad (2.50)$$

$$\mathbf{K}_{pm} = \sum_{i=1}^n E_{pi} I_{pi} \int_{x_{2i-1}}^{x_{2i}} \Psi(x) \cdot \Psi''''(x) dx \quad (2.51)$$

Easily additional matrix terms for multiple masses of equation (2.16) and multiple support of equation (2.17) can be added.

2.4.2 Experimental Validation of the Piezo Beam Systems

The numerical model of the beam equipped with a piezoelectric actuator (2.46), will be validated with the displacement data acquired from an experimental test structure. Figure 2.30 shows the experimental set-up. Different steel balls can be accelerated by a ramp and move over the simply supported beam. The beam has a length of $l = 0.6$ m and a cross section area $A = 0.1$ m x 0.002 m. The d_{33} piezoelectric actuator called Macro Fiber Composite (MFC) 8557-P1 of the company smart-material is utilised at the middle of the beam, the starting location is $x_1 = 0.2575$ m and end location is $x_2 = 0.3425$ m, similar to the first span in Figure 2.9. The active area is 85×57 mm². Sensor location x_{s1} - x_{s3} are identical to the set-up in section 0. These might change for control purposes, to have a collocated control system. A High Voltage Amplifier HVA 1500 amplifies the input voltage by a factor of 200 from -2.5 V – 5 V to -250 V – 1500 V.

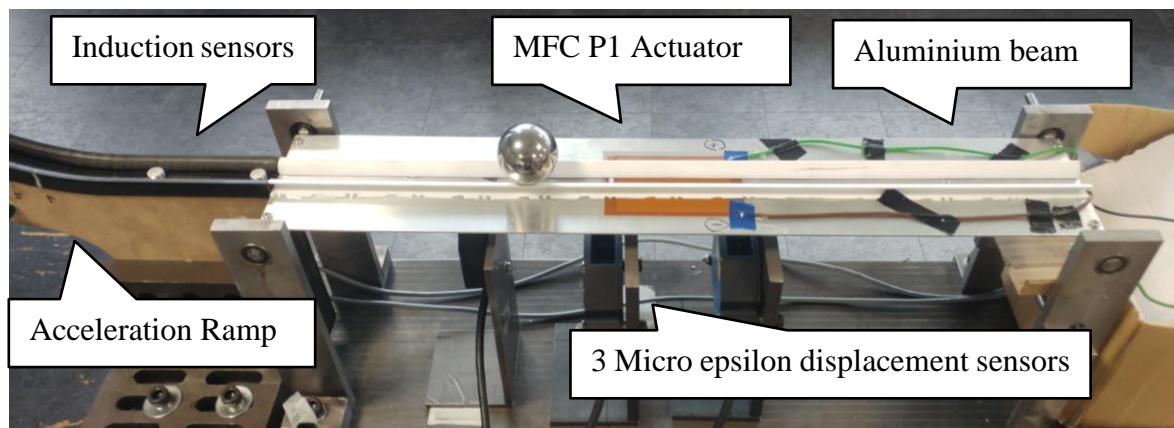


Figure 2.30. Experimental set-up of the aluminium beam actuated by piezoelectric actuator.

Figure 2.31 shows the deflection response $w(x_{si}, t)$ at the sensor locations $x_{s3} = 0.35$ m when mass $m = 0.509$ kg and 0.377 kg move over the beam. The parameters of the numerical beam model are defined as mass per length $\rho A = 0.812$ kgm⁻¹ and flexural rigidity $EI = 13.211$ Nm⁻². The height is changed to 2.83 mm to take into account the added stiffness of the polymer guiding rail. With these adjustments, a good approximation between the numerically calculated deflection and the experimentally obtained data is accomplished. It is noticed that this structure is more flexible compared to the previously studied structure,

which comprises additional stiffness added by the electrodynamic actuator (compare with Figure 2.21).

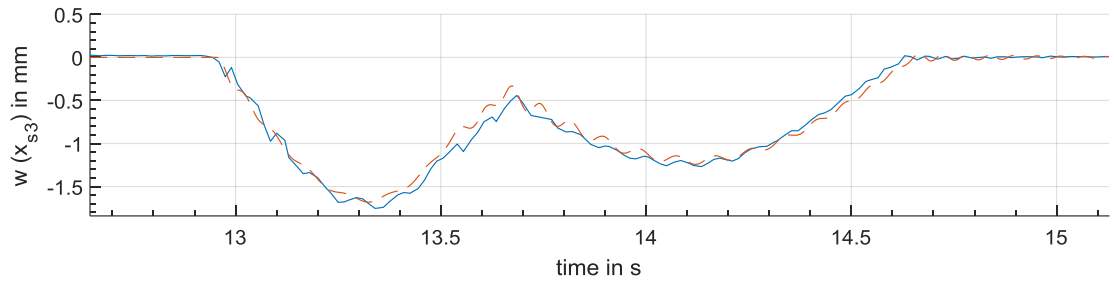


Figure 2.31. Time history of the deflection of the numerical model (red dashed) and the experimental measurements (blue) at sensor locations and x_{s3} (bottom).

The piezoelectric actuator has the piezoelectric constant $d_{33} = 460$ pm/V, a Young modulus of $E_p = 30.336$ GPa [101] a height of $h_p = 0.3$ mm and an electrode distance of $L_e = 407.18$ μ m [66]. This results in a specific piezoelectric constant $C_0 = 8.292 \times 10^{-4}$ Nm/V in equation (2.43).

Figure 2.32 illustrates a comparison between the numerical simulation (red dashed) and the experimental obtained deflection (blue continuous). The correction factor $c_p = 0.32$ is applied in equation (2.46). This correction factor compensates the experimentally applied smaller piezoelectric moment on one side. Losses may be due to the bonding of the actuator onto the structure and model uncertainties. On the other side, the beam becomes more rigid by adding the polymer guiding rail, which is considered in the numerical beam model only to a certain extend by changing the height h . c_p was determined by minimizing the error between the experimental and the analytical deflection data.

Four masses are launched and the piezo element is supplied with prescribed voltage, which is a sum of sinusoidal functions. Good matches between the experimentally measured data and the numerical model deflections are accomplished.

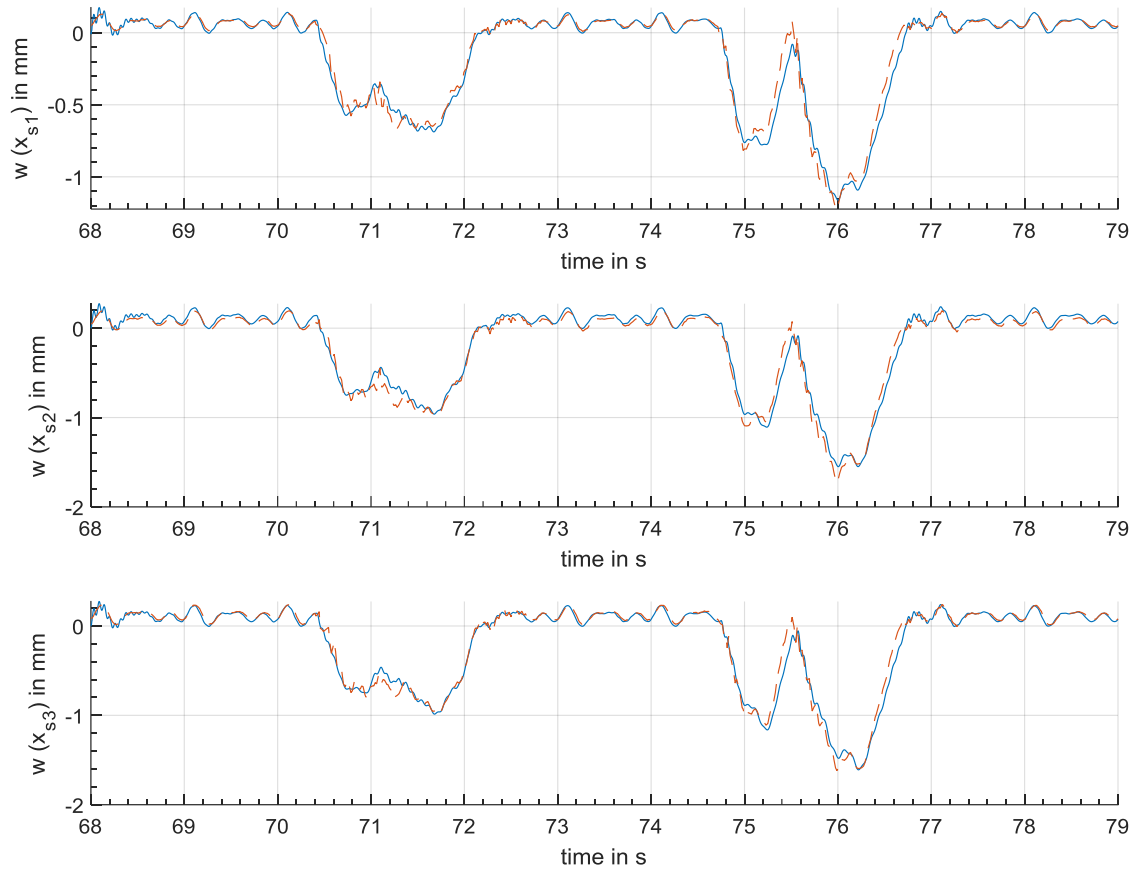


Figure 2.32. Time history of the deflection at sensor locations $w(x_{s2})$ and $w(x_{s3})$ of the numerical model (blue dashed) and the experimental data (red continuous).

Validation of the Two-Span Continuous Beam structure actuated by the Piezoelectric Actuators

In the following the two-span continuous beam structure equipped with two piezoelectric actuators, and three laser displacement sensors, see Figure 2.8, will be validated against the numerical model. The sensor locations are described in section 2.1.3. The MFC 8557 P1 actuators are located in the middle of each span, with its start and end locations $x_1 = 0.2575\text{m}$, $x_2 = 0.3425\text{m}$, $x_3 = 0.8575\text{m}$ and $x_4 = 0.9425\text{m}$ respectively, see Figure 2.9. Ten modes are used in the simulation.

Before the polymer rail is added to the structure, the numerical model is validated with experimental results of the two-span continuous structure actuated by two MFC actuators.

The height in the numerical model equals the height of the structure. The correction factor $c_p = 0.68$, was determined by minimizing the error between the experimental and the analytical deflection data. It is a higher value compared to the previously case. Without the guiding rail the structure is less rigid. Figure 2.33 displays the deflection response at sensor locations x_{s1} and x_{s2} when actuator 1 is fed with a sinusoidal input voltage U_1 , see Figure 2.34. MFC 2 is supplied with a constant input voltage $U_2=500V$.

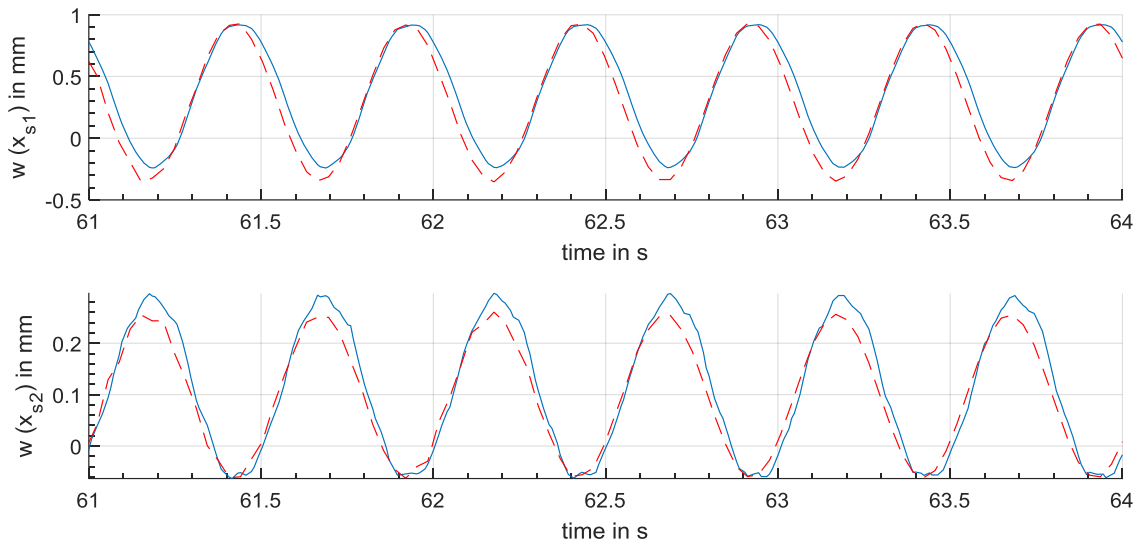


Figure 2.33. Time history of the deflection of the two-span beam structure at sensor locations x_{s1} and x_{s2} , measurements (blue continuous), numerical model (red dashed).

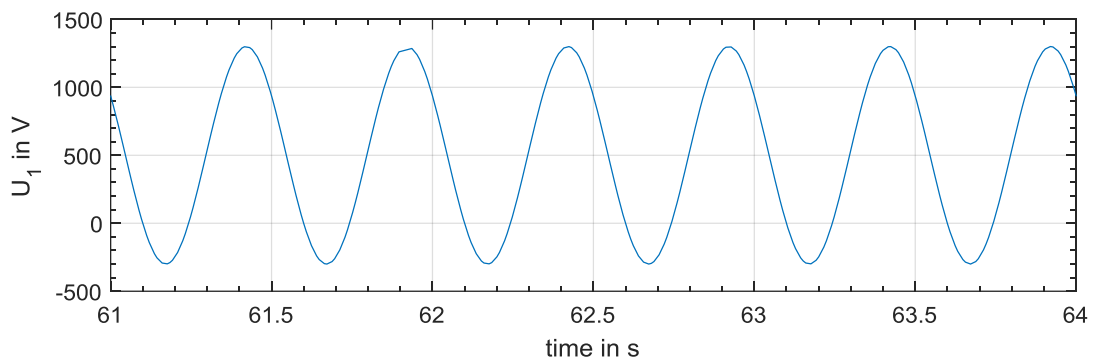


Figure 2.34. Input voltage U_1 for piezoelectric actuator MFC 1.

It can be noticed that there are good matches between the numerical and the experimental data at sensor location x_{s1} and x_{s2} , especially when the voltage increases. When the voltage decreases a delay in the sensor deflection x_{s1} and x_{s2} can be observed.

In the next step the polymer guiding rail is attached to the two-span beam. In the numerical model the height is changed to $h=2.83$ mm. Also the correction factor changes to $c_p=0.39$, which was again determined by minimizing the error between the experimental and the analytical deflection data. In Figure 2.35 the piezoelectric actuators 1 and 2 are fed with sinusoidal voltages, shown in Figure 2.36 . U_1 reaches the maximum actuation voltage for the piezoelectric actuators. The deflection at x_{s1} provides a very good match between the numerical and experimental data. At the second span at x_{s2} and x_{s3} a small mismatch can be noticed. Again this might be due to the specific design of the supports.

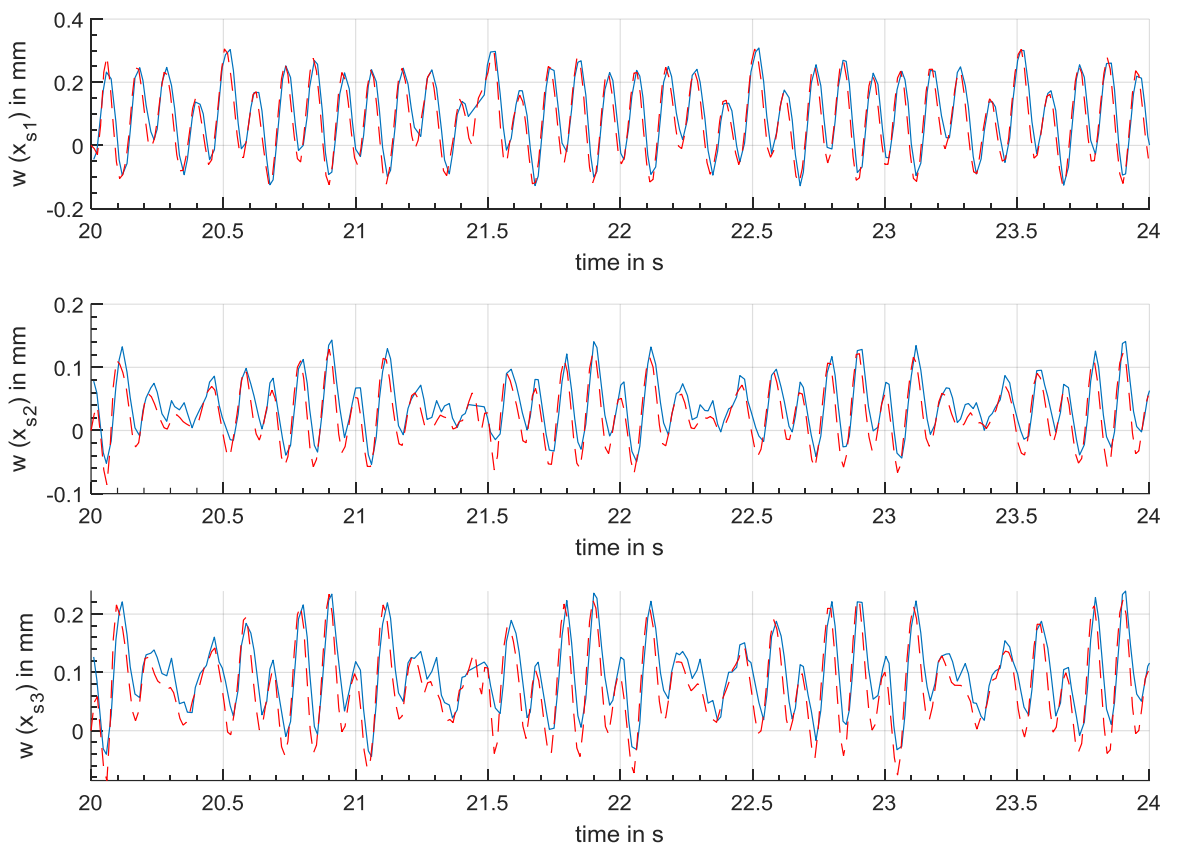


Figure 2.35. Time history of the deflections of the two-span continuous beam at sensor locations $x_{s1} - x_{s3}$, measurements (blue continuous) and numerical model (red dashed).

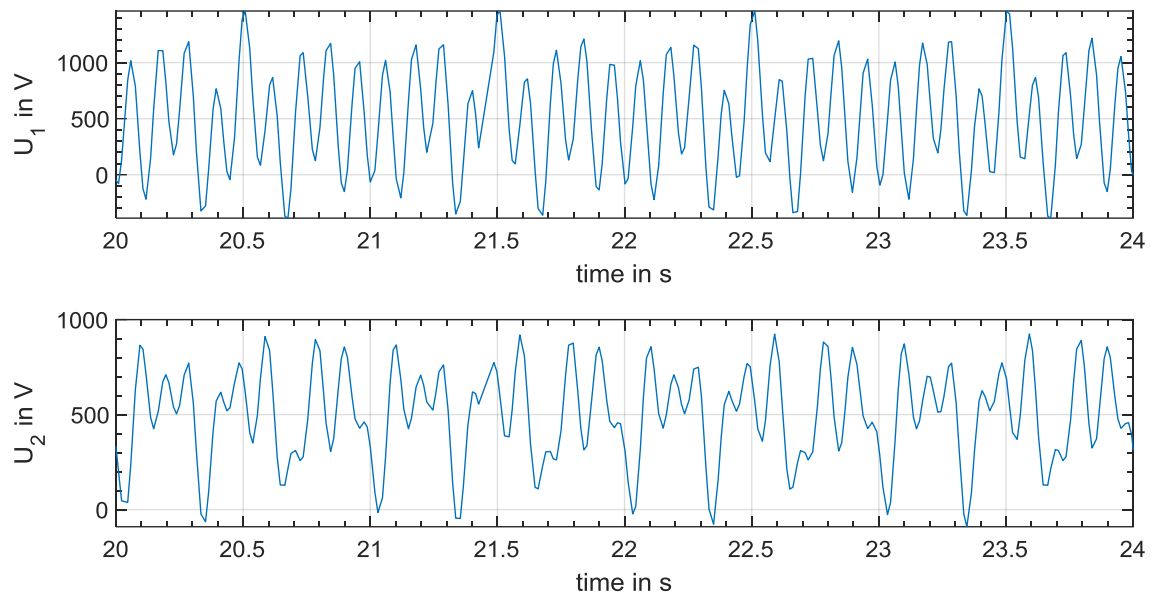


Figure 2.36. Time history of the input voltages U_1 (top) and U_2 (bottom).

2.5 Concluding Remarks

In this section, the numerical model of the simply supported beam actuated by moving masses was derived. If at least eight modes are used in the numerical model, a two-span continuous beam can be approximated with sufficiently high accuracy. The numerical single and the two-span beam models were validated against the displacement measurements of the respective experimental set-up. Different actuator models were studied. The dynamics of the electrodynamic shaker, as well as the interactions with the beam, proved to be complex. A simplified first order model can be applied to a certain extend. It offers the advantage of representing the shaker-beam model in the state-space representation. The MFC-actuator is modelled by applying moment at its edges to the beam. The shaker-beam model and the MFC-beam models were validated against experimental data. In the next chapter optimal control approaches will be studied relevant to the moving load problem.

3 Optimal Control Approaches Dedicated to the Moving Mass Problem

To control the moving load structure, in this chapter classical optimal control approaches suitable for time-varying structures are studied. This includes the finite-time optimal control in section 3.1. Here the algebraic Riccati equation is solved backwards for a given leaving time t_f . The step-by-step optimal control, presented in section 3.2, solves the Riccati equation at every time-step t with the varied system equations.

3.1 The Finite Time Optimal Control

When only one actuator is used, the time-varying plant with the states and control matrices presented in equation (2.36) can be written in state-space form as:

$$\dot{\mathbf{x}}(t) = \mathbf{A}(t)\mathbf{x}(t) + \mathbf{B}(t)u(t) \quad (3.1)$$

For the multiple-input multiple-output case (MIMO) the input $u(t)$ becomes a vector $\mathbf{u}(t)_{1 \times a}$, with a inputs. The aim of the controller is to minimize the deflection response at different locations along the beam. In order to achieve this, the performance objective can be formulated like a quadratic objective in deflection at sensor locations

$$J = \frac{1}{2} \int_{t_0}^{t_f} \mathbf{w}^T(x_{si}, t) \mathbf{Q} \mathbf{w}(x_{si}, t) dt = \frac{1}{2} \int_{t_0}^{t_f} \mathbf{x}^T(t) \mathbf{C}^T \mathbf{Q} \mathbf{C} \mathbf{x}(t) dt \quad (3.2)$$

subject to equation (3.2) and the control's saturation limits $|u(t)| \leq u_0$. In equation (3.3) matrix \mathbf{C} is the output matrix of the system described by (3.2) and consists of modal shape vectors $\boldsymbol{\psi}(x_{si})$.

This type of objective function was studied in [17] and it was shown that it leads to a two-boundary value problem which makes the control design problem mathematically challenging. Also, the synthesised control function is discontinuous. Such a control solution, even if it correctly describes the required control action, may be difficult to implement, as

the electromagnetic type of actuation chosen here cannot accurately describe a control function with discontinuities. For this reason, a quadratic objective function that also includes the control has been chosen. The quadratic performance index is defined as:

$$J = \frac{1}{2} \mathbf{x}^T(t_f) \mathbf{F} \mathbf{x}(t_f) + \frac{1}{2} \int_{t_0}^{t_f} [\mathbf{x}^T(t) \mathbf{Q} \mathbf{x}(t) + \mathbf{u}^T(t) \mathbf{R} \mathbf{u}(t)] dt \quad (3.3)$$

The emphasis on the deflection will be addressed by choosing a state weighting matrix \mathbf{Q} with higher values corresponding to the first states corresponding to the displacements and a significantly lower value for the terms corresponding to the velocities. The control limitation is assured by the selection of the control weighting parameter \mathbf{R} . The control $\mathbf{u}(t)$ is unconstrained. t_f is specified and the final state $\mathbf{x}(t_f)$ is constrained by the weighting matrix $\mathbf{F}(t_f)$. For a system with p states and r actuators, the matrices $\mathbf{F}(t_f)$ and $\mathbf{Q}(t)$ are $p \times p$ symmetric, positive semidefinite matrices and matrix $\mathbf{R}(t)$ is $r \times r$ symmetric, positive definite matrix. The solution can be found using the Pontryagin minimum principle [54]. The Hamiltonian is defined as

$$\begin{aligned} \mathcal{H}(\mathbf{x}(t), \mathbf{u}(t), \boldsymbol{\lambda}(t)) \\ = \frac{1}{2} \mathbf{x}'(t) \mathbf{Q} \mathbf{x}(t) + \frac{1}{2} \mathbf{u}'(t) \mathbf{R} \mathbf{u}(t) + \boldsymbol{\lambda}'(t) (\mathbf{A}_m(t) \mathbf{x}(t) \\ + \mathbf{B}_m(t) \mathbf{u}(t)) \end{aligned} \quad (3.4)$$

where $\boldsymbol{\lambda}(t)$ is defined as the costate vector. The necessary optimality condition can be expressed as

$$\mathcal{H}(\mathbf{x}^*(t), \mathbf{u}(t), \boldsymbol{\lambda}^*(t)) \geq \mathcal{H}(\mathbf{x}^*(t), \mathbf{u}^*(t), \boldsymbol{\lambda}^*(t)) \quad (3.5)$$

where the optimal values for the control $\mathbf{u}^*(t)$ and for the states $\mathbf{x}^*(t)$ are assumed. For the particular case when the Hamiltonian is pointwise differentiable, the optimal control $\mathbf{u}^*(t)$ can be obtained by using

$$\frac{\partial \mathcal{H}}{\partial \mathbf{u}} = 0 \rightarrow \mathbf{R}(t)\mathbf{u}^*(t) + \mathbf{B}^T(t)\boldsymbol{\lambda}^*(t) = 0 \quad (3.6)$$

with the relation $\boldsymbol{\lambda}^*(t) = \mathbf{P}(t)\mathbf{x}^*(t)$ to

$$\mathbf{u}^*(t) = -\mathbf{R}^{-1}(t)\mathbf{B}^T(t)\mathbf{P}(t)\mathbf{x}^*(t) = -\mathbf{k}(t)\mathbf{x}^*(t) \quad (3.7)$$

$\mathbf{k}(t) = -\mathbf{R}^{-1}(t)\mathbf{B}^T(t)\mathbf{P}(t)$ is called the Kalman gain and $\mathbf{P}(t)$, is a $p \times p$ symmetric, positive definite matrix (for all $t \in [t_0, t_f]$), and is the solution of the matrix differential Riccati equation

$$\dot{\mathbf{P}}(t) = \mathbf{P}(t)\mathbf{A}(t) - \mathbf{A}^T(t)\mathbf{P}(t) - \mathbf{Q}(t) + \mathbf{P}(t)\mathbf{B}(t)\mathbf{R}^{-1}(t)\mathbf{B}^T(t)\mathbf{P}(t) \quad (3.8)$$

The optimal state is the solution of

$$\dot{\mathbf{x}}^*(t) = [\mathbf{A}(t) - \mathbf{B}(t)\mathbf{R}^{-1}(t)\mathbf{B}^T(t)\mathbf{P}(t)]\mathbf{x}^*(t) = \mathbf{G}(t)\mathbf{x}(t) \quad (3.9)$$

The matrix differential equation (3.8) can be solved backwards with $t_{start}=t_f$ and the initial condition $\mathbf{P}(t = t_f) = \mathbf{F}(t_f)$. The optimal time-varying gain $\mathbf{k}(t)$ is calculated forward using the values of $\mathbf{P}(t)$. As long as the control system is treated in finite time there is no condition on stability or controllability for the closed-loop system $\mathbf{G}(t)$ [54]. Although p optimal states in $\mathbf{x}^*(t)$ are calculated, in theory the structure has an infinite number of states which can cause instability, called spill-over. Therefore, the parametric study has to prove the performance of the control system for a reasonable number of masses and speeds of the moving mass.

3.2 Step by Step Calculation of the Riccati Equation

A drawback of the previously presented method is that the algebraic Riccati equation (3.8) has to be solved backwards offline. An online adaptation to previously unknown changes of the load seems not possible or how it will be shown later only to a certain extent. An alternative algorithm solves the algebraic Riccati equation numerically at particular time

steps t_i . It imitates the infinite horizon linear quadratic problem solution for linear time-invariant systems.

$$\mathbf{A}_m^T(t_i)\mathbf{P}(t_i) + \mathbf{P}(t_i)\mathbf{A}_m(t_i) - \mathbf{P}(t_i)\mathbf{B}_m(t_i)\mathbf{R}^{-1}\mathbf{B}_m^T(t_i)\mathbf{P}(t_i) + \mathbf{Q} = 0 \quad (3.10)$$

The time-dependent gain vector calculates as

$$\mathbf{k}(t_i) = \mathbf{R}^{-1}\mathbf{B}_m(t_i)^T\mathbf{P}(t_i) \quad (3.11)$$

Because of the separation into time-steps the solution does not satisfy the optimality criteria [29]. This method was applied in [63], where reduction of the maximum deflection of 12% was achieved by the time-varying control for the simply supported beam structure presented in previous section. The modal shaker with its complex dynamics limited higher gains for a feedback control solution at this point and an open-loop control was applied to achieve a reduction of up to 43% for the time-variant control, where the input voltage history was calculated beforehand. The time-varying gains of the two proposed methods in equation (3.7) and equation (3.11) are identical for the studied test structure of the simply supported beam.

4 The State Estimation

The previously presented optimal control state feedback approaches assume the availability of all of the states $\mathbf{x}(t)$. In the case of the vibrations of continuous beam structures there are in theory an infinite number of modal coordinates which are physically not measurable. In addition, sensor measurements $\mathbf{y}(t)$ might be noisy. With the help of the classical state estimator presented in section 4.1, the states $\mathbf{x}(t)$ can be estimated from the noisy measurements \mathbf{y} . The noise can be extracted from the measurement \mathbf{y} for the use in a displacement feedback law.

If the moving load is treated as a disturbance, as it might be the case in vehicle-bridge interaction, states could be estimated by a method presented in section 4.2, where the states are estimated with the help of the mode shapes.

4.1 Optimal Full-State Estimation

Given the system with state disturbance \mathbf{w}_d and sensor disturbance \mathbf{w}_n

$$\dot{\mathbf{x}} = \mathbf{A}\mathbf{x} + \mathbf{B}\mathbf{u} + \mathbf{w}_d \quad (4.1)$$

$$\mathbf{y} = \mathbf{C}\mathbf{x} + \mathbf{D}\mathbf{u} + \mathbf{w}_n$$

The classical state estimator assumes a zero-mean Gaussian distribution for the both disturbances with known covariances.

$$\mathbb{E}(\mathbf{w}_d(t)\mathbf{w}_d(\tau)^T) = \mathbf{Q}\delta(t - \tau) \quad (4.2)$$

$$\mathbb{E}(\mathbf{w}_n(t)\mathbf{w}_n(\tau)^T) = \mathbf{R}\delta(t - \tau)$$

Where \mathbb{E} is the expected value and $\delta(t)$ is the Dirac delta function. The positive semi definite matrices \mathbf{R} and \mathbf{Q} contain the covariances of the disturbance and noise term. The measurement errors are assumed uncorrelated:

$$\mathbb{E}(\mathbf{w}_d(t)\mathbf{w}_n(\tau)^T) = \mathbf{0} \delta(t - \tau) \quad (4.3)$$

Full-state estimation is mathematically possible if the pair (\mathbf{A}, \mathbf{C}) is observable. The moving load disturbance does not behave in that way during travelling time. Because of that, using the classical state estimation approach, information about the load must be known and could be included in $\mathbf{B}\mathbf{u}$. In [102], the observer of a system is defined as

$$\dot{\hat{\mathbf{x}}}(t) = \mathbf{A}\hat{\mathbf{x}}(t) + \mathbf{B}\mathbf{u} + \mathbf{L}(y - \mathbf{C}\hat{\mathbf{x}}) \quad (4.4)$$

where $\hat{\mathbf{x}}$ is the estimate of the actual state. The observer gain \mathbf{L} is to be determined in the design procedure. This can be done by pole placement or by optimal full-state estimation [103]. In the latter \mathbf{L} is determined by

$$\mathbf{L} = \mathbf{P}\mathbf{C}^T\mathbf{R} \quad (4.5)$$

Where \mathbf{P} is the solution to the algebraic Riccati equation:

$$\mathbf{P}\mathbf{A}^T + \mathbf{A}\mathbf{P} - \mathbf{P}\mathbf{C}^T\mathbf{Q}^{-1}\mathbf{C}\mathbf{P} + \mathbf{Q} = \mathbf{0} \quad (4.6)$$

A duality of the state observer to the linear quadratic regulator is present [104]. In the full state observer design the estimated states are used in the state feedback control. The feedback law $\mathbf{u} = -\mathbf{K}\hat{\mathbf{x}}$ is substituted in equation (4.4) to obtain the compensator

$$\dot{\hat{\mathbf{x}}}(t) = (\mathbf{A} - \mathbf{B}\mathbf{K} - \mathbf{L}\mathbf{C})\hat{\mathbf{x}}(t) + \mathbf{L}y \quad (4.7)$$

$$\mathbf{u} = -\mathbf{K}\hat{\mathbf{x}}(t)$$

The full-state feedback and the observer can be designed independently [102].

4.2 State Estimation by Mode Shapes

The particular type of problem studied where the loads act like disturbances, which for times comparable with the time the load is on the structure cannot be considered random Gaussian processes, makes the use of an estimator difficult. The solution presented here assumes that the number of sensors equals the number of modes used for the numerical model. The state vector is estimated from the experimentally measured deflection vector $\mathbf{w}(t)_{n \times 1} = [w_1(x_{s1}, t) \dots w_n(x_{sn}, t)]^T$ and the velocity vector $\dot{\mathbf{w}}(t)_{n \times 1} = [\dot{w}_1(x_{s1}, t) \dots \dot{w}_n(x_{sn}, t)]^T$ at locations x_{sn} :

$$\begin{aligned}\mathbf{q}(t) &= \mathbf{\Psi}(x_{sn})^{-1} \mathbf{w}(t) \\ \dot{\mathbf{q}}(t) &= \mathbf{\Psi}(x_{sn})^{-1} \dot{\mathbf{w}}(t)\end{aligned}\tag{4.8}$$

In this equation $\mathbf{\Psi}(x_{sn})$ is the $n \times n$ non-singular matrix that contains the mode shapes calculated at sensor locations x_{sn} :

$$\mathbf{\Psi}(x_{sn})_{n \times n} = \begin{bmatrix} \psi_1(x_{s1}) & \psi_2(x_{s1}) & \dots & \psi_n(x_{s1}) \\ \psi_1(x_{s2}) & \psi_2(x_{s2}) & \dots & \psi_n(x_{s2}) \\ \vdots & \vdots & \ddots & \vdots \\ \psi_1(x_{sn}) & \psi_2(x_{sn}) & \dots & \psi_n(x_{sn}) \end{bmatrix}\tag{4.9}$$

When n sensors are used and n modes are estimated, the state-space vector can be determined as a unique solution of equations.

5 Case Study 1: Active Vibration Control of a Simply Supported Beam Acted upon by Moving Masses

The previously presented finite time optimal control approach was applied to control the simply supported beam, published in [28]. The estimation of the modes was accomplished by the mode shapes. These results and additional studies regarding estimation and an augmented optimal control, will be presented in the following section.

5.1 Experimental and Numerical Validation of the State Estimation Methods

From equation (4.8) and equation (4.9) it follows that, since three sensors are installed, three modal coordinates, q_i , ($i = 1,2,3$) can be calculated directly and by using the derivative three modal velocities \dot{q}_i , ($i = 1,2,3$). (Figure 5.1). A mass $m = 0.261$ kg is moving on the structure.

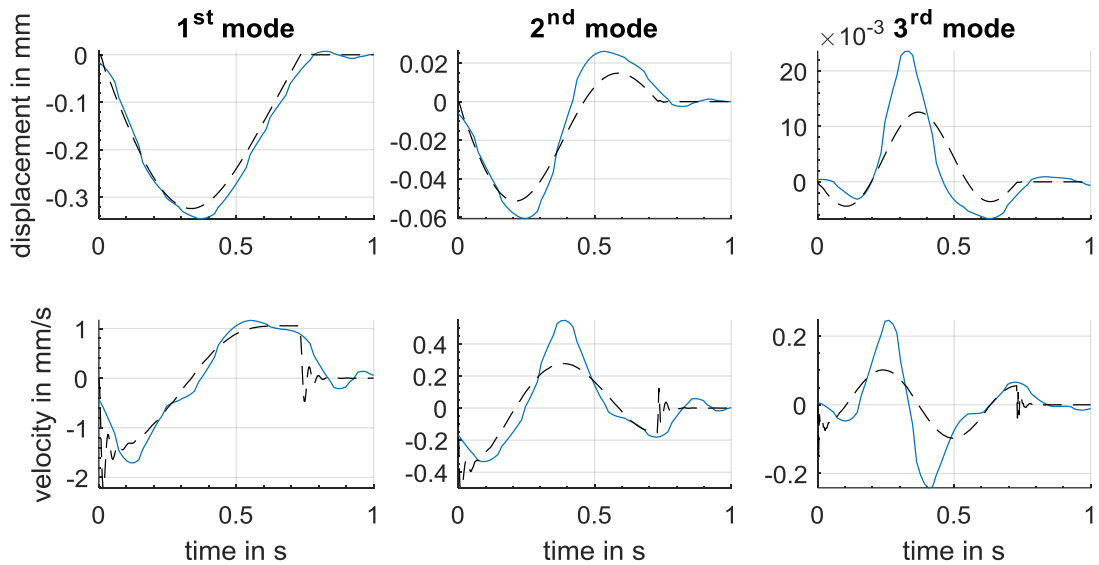


Figure 5.1. Comparison modal coordinates numerical model (black dashed) and the measured signal (blue continuous).

The first mode is dominant and shows the best agreement with the modal displacement estimated using experimental data. For the modal velocity, the first mode also shows the best match. A 10th order digital low-pass filter with a cut-off frequency $f_{3dB} = 10$ Hz, reduces the noise but it causes a slight delay.

The classical state observer presented in section 4.1 equation (4.4) will be validated experimentally for the open-loop system of the simply supported beam. For the offline calculation of the observer gain \mathbf{L} in equation (4.5) with the help of equation (4.6), due to the duality to the optimal control the Linear-Quadratic-Regulator algorithm in MATLAB can be used: $\mathbf{L}' = \text{dlqr}(\mathbf{A}', \mathbf{C}', \mathbf{Q}, \mathbf{R})$. The error and performance index are defined as $\mathbf{Q} = \text{diag}(1000, 100, 10, 0.1, 0.01, 0.01, 0)$ and $\mathbf{R} = 10^6$. Basically, when the error covariance \mathbf{R} is weighted higher than \mathbf{Q} , then the measurement $w(x_{s2})$ is trusted less, which results in a lower gain \mathbf{L} . Examining equation (4.4), this means that the system equation is trusted more than the sensor data. In the observer's system equation, the time-varying parts $\Delta\mathbf{M}$, $\Delta\mathbf{D}$, and $\Delta\mathbf{K}$ are neglected to guarantee small sampling times:

$$\mathbf{A} = \begin{bmatrix} \mathbf{0}_{n \times n} & \mathbf{I}_{n \times n} \\ -\mathbf{M}^{-1}\mathbf{K} & -\mathbf{M}^{-1}\mathbf{D} \end{bmatrix} \quad (5.1)$$

as also the input matrix \mathbf{B} has to be time-invariant, it is transformed to

$$\mathbf{B}_f = \begin{bmatrix} \mathbf{0}_{n \times n} & \mathbf{0}_{n \times n} \\ \mathbf{0}_{n \times n} & \mathbf{M}^{-1}\mathbf{I}_{n \times n} \end{bmatrix}, \quad \mathbf{u}_f(t) = \begin{bmatrix} \mathbf{0}_{n \times n} \\ -\boldsymbol{\psi}(vt)mg \end{bmatrix} \quad (5.2)$$

With $\mathbf{u}_f(t)$ now being the time varying input. For the implementation, the time-invariant system matrices are calculated and discretised offline in MATLAB and stored on the compactRIO controller. Figure 5.2 shows the modal coordinates extracted by this observer for mass $m = 0.509$ kg travelling with $v = 0.55$ m/s. The sampling time is 10 ms. It can be noticed that the model displacements have a very good alignment with the numerical model, whereas at the modal velocities only \dot{q}_1 can be calculated properly. Also an impulse is noticed when the mass leaves the structure.

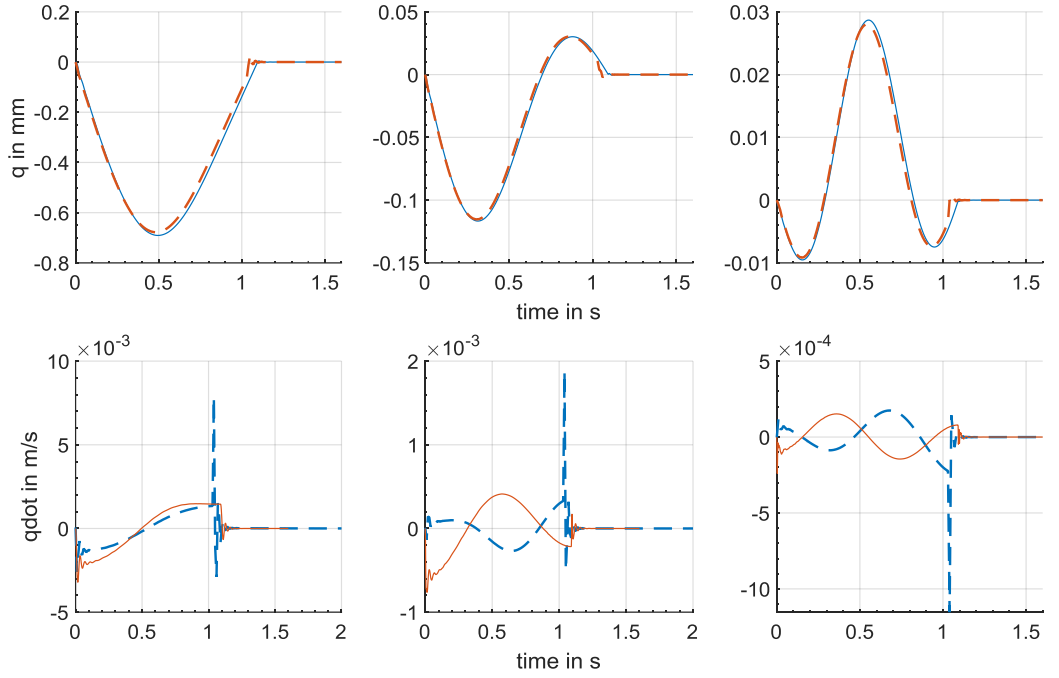


Figure 5.2. Comparison of the modal coordinates numerical model (red continuous) and the measured signal (blue dashed).

A numerical example for the full-state observer is presented next. The simply supported beam equipped with the electrodynamic shaker is considered. See section 2.2.3 for the model parameter. For simplicity the feedback gain \mathbf{K} is calculated for the time-invariant structure, see equation (5.7). The weighting matrices are defined as $\mathbf{R} = 9 \times 10^{-8}$ and $\mathbf{Q} = \text{diag}(1000, 100, 10, 0.1, 0.01, 0.01, 0)$. The beam mass system of equation (2.36) is discretised at every time step k .

$$\begin{aligned} \mathbf{x}(k+1) &= \mathbf{A}_m(k)\mathbf{x}(k) + \mathbf{B}_m(k)\mathbf{u}(k) + \mathbf{B}_f(k)\mathbf{u}_f + \mathbf{w} \\ \mathbf{y}(k) &= \mathbf{C}(k)(\mathbf{x}(k) + \mathbf{v}) \end{aligned} \quad (5.3)$$

where \mathbf{w} is the system noise vector and \mathbf{v} is the measurement noise vector, which is expected to be Gaussian. Also the observer is represented in discrete time as a time-invariant system to simulate the implementation on the controller as

$$\hat{\mathbf{x}}(k+1) = (\mathbf{A} - \mathbf{BK} - \mathbf{LC})\hat{\mathbf{x}}(k) + \mathbf{L}y + \mathbf{B}_f \mathbf{u}_f(k) \quad (5.4)$$

where \mathbf{B}_f and \mathbf{u}_f are similar to the matrices of equation (5.2) with an additional zero added for the inclusion of the shaker dynamic in \mathbf{A} .

$$\mathbf{B}_f = \begin{bmatrix} \mathbf{0}_{n \times n} & \mathbf{0}_{n \times n} & 0 \\ \mathbf{0}_{n \times n} & \mathbf{M}^{-1} \mathbf{I}_{n \times n} & 0 \\ 0 & 0 & 0 \end{bmatrix}, \quad \mathbf{u}_f(k) = \begin{bmatrix} \mathbf{0}_{n \times n} \\ -\Psi(v t_s k) m g \\ 0 \end{bmatrix} \quad (5.5)$$

As shown before in section 2.3 the dynamic amplification of the load might be small at small velocities and mass ratios. Hence a time-invariant observer might be sufficient. To update the time-variant system matrices $\mathbf{A}(k)$ at every time step, k would counteract the real-time ability but could be done offline in advance for certain times. Figure 5.3 summarizes the block chart of the time-varying system and the time-invariant observer control.

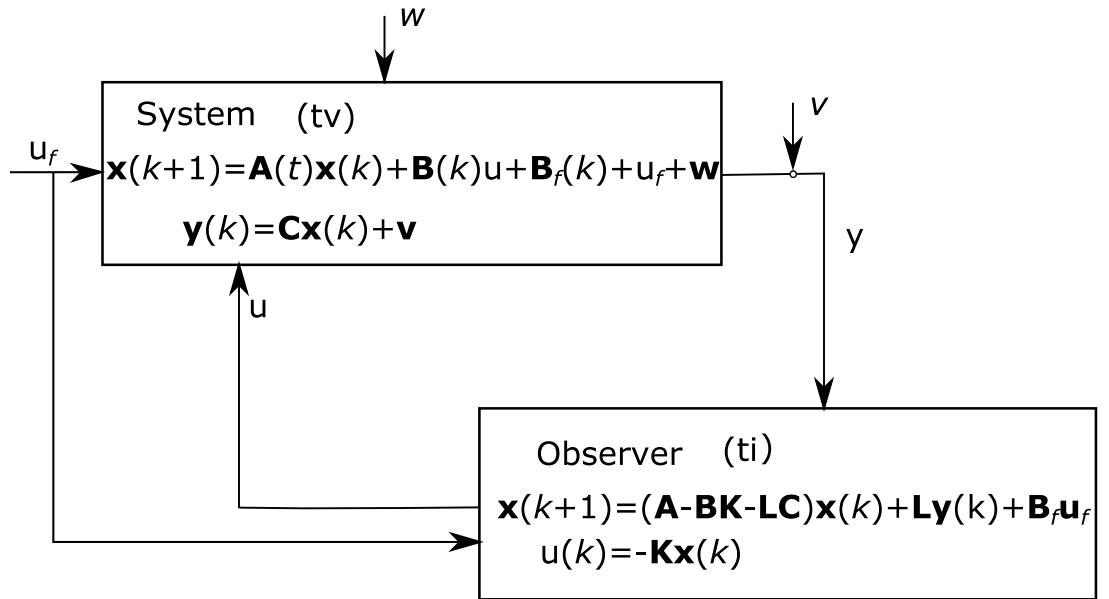


Figure 5.3. Block chart of the time-varying (tv) system with the full-state time-invariant (ti) observer control.

Additional measurement noise \mathbf{v} is added. From previous sensor data $w(x_{s1}) - w(x_{s3})$ error covariances $\mathbf{R}_n = [0.0365, 0.135, 0.0729] \times 10^{-10} m^2$ were determined. The added noise is defined by the normal distribution $v_i = N(0, \sqrt{R_{ni}})$, where R_{ni} is the i -th element

of \mathbf{R}_n . No system noise v is assumed so far. Figure 5.4 illustrates the mode shapes of the discrete time observer and compares it with the discrete time system states as well as with the states of the continuous system solved by the ODE solver in MATLAB. Note that also the state z can be observed.

This type of time invariant state observer is suitable for this low mass and low speed. It should be noted that a sampling time of 0.2 ms is simulated, which might not be possible to accomplish on the actual compactRio controller. However, in this way a very good match of the observer states (blue dot-dashed) towards the continuous time modelled states (green continuous) can be accomplished.

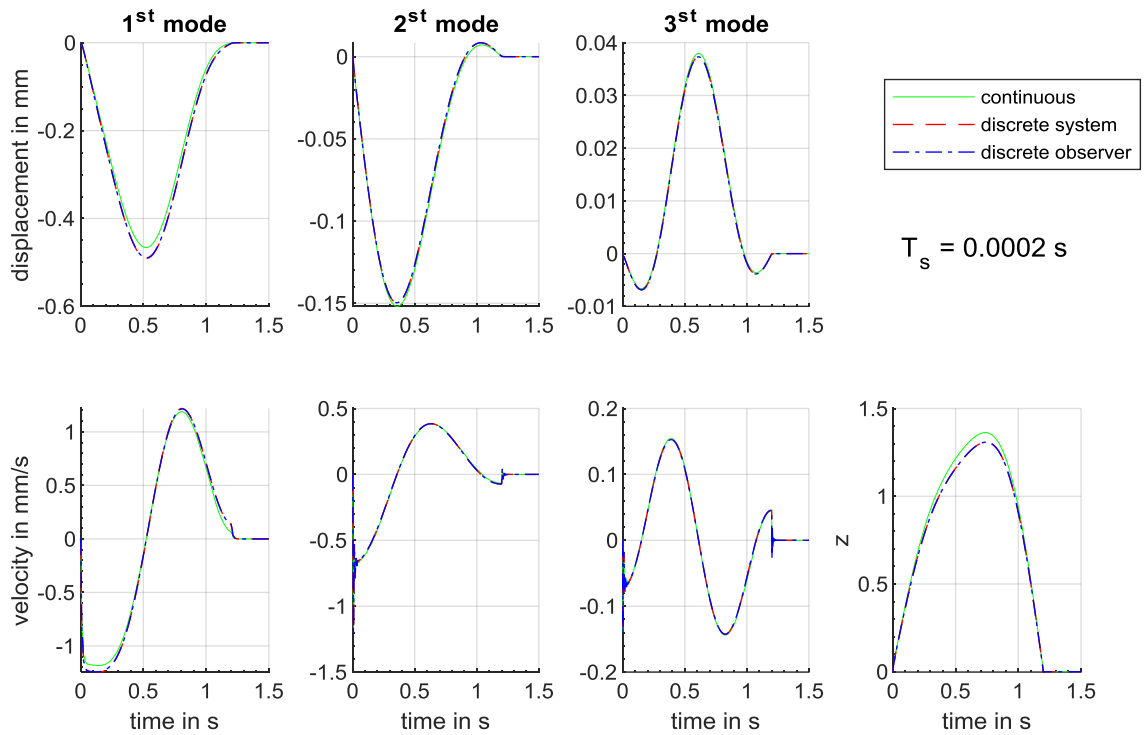


Figure 5.4. Mode shapes of the time-invariant controlled system simulated with the ode solver as a continuous system (green continuous), system states (red dashed), observer states (blue dash-dotted) mass $m = 0.501$ kg, speed $v = 0.5$ m/s.

Figure 5.5 displays the time histories of the deflection response $w(x_{s2})$ of the discrete observer, of the discrete time system and of the continuous uncontrolled structure. The observer filters the added measurement noise and able to reduce the deflection response by 27%.

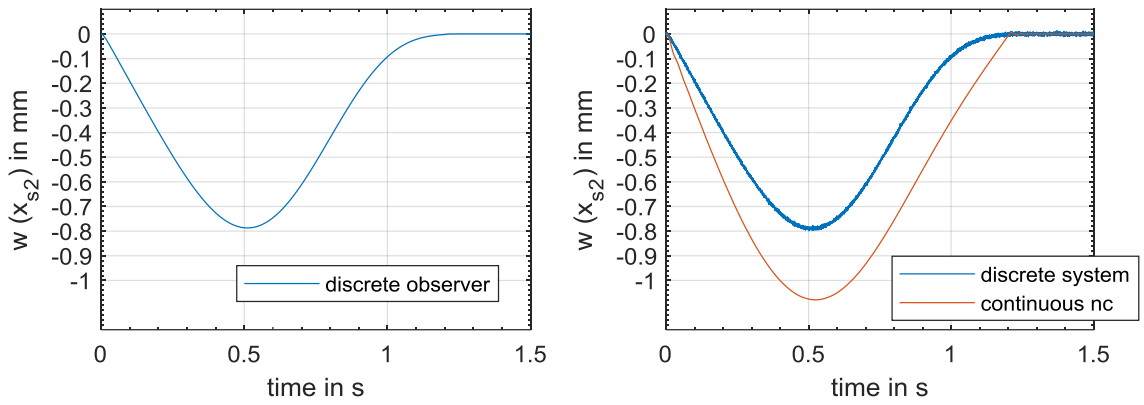


Figure 5.5. Deflection responses $w(x_{s2})$ of the controlled discrete system with added measurement noise (blue), the uncontrolled continuous structure (red) (right) and of the discrete observer (left).

For larger, actual implementable sampling time $T_s = 5$ ms it can be noticed in Figure 5.6 that the system mode shapes differ drastically from the continuous time system. However, the observer (blue dot-dashed) can observe the modal displacements, the first modal velocity and the z state of the discrete system (red-dashed) with high accuracy.

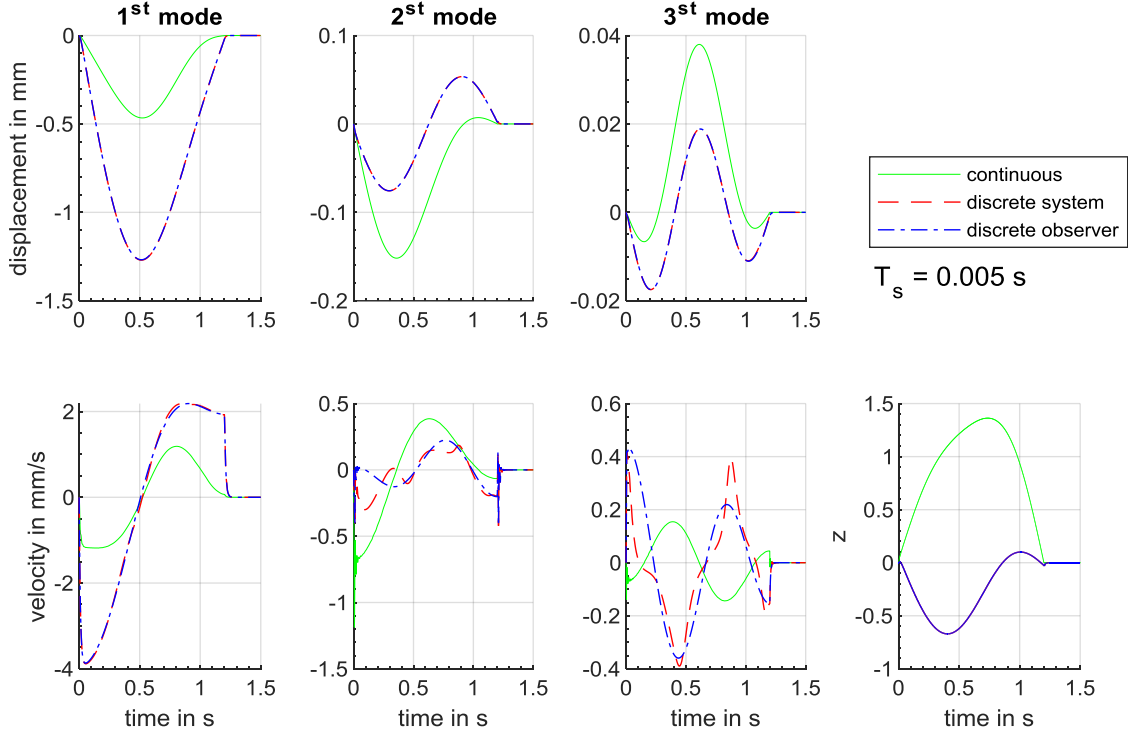


Figure 5.6. Comparison of the mode shapes of the continuously controlled system (green) with the discrete system modes (red dashed) and discrete time observer (blue dash-dotted) for the sampling time $T_s = 5$ ms.

The reason for this large discrepancy between the continuous system (green continuous) and the discrete system (red dashed) lies inside the discrete time optimal control algorithm. For the previous example with $T_s = 5$ ms it results in a gain vector of $\mathbf{K} = [-356.7 \ -6250 \ 2760.8 \ 22.83 \ 2.9 \ 0.13 \ 0.203]$. Keeping in mind that the first two modes have the highest influence the displacement response one can notice that $u = -\mathbf{K}\mathbf{x}$ leads to a negative input voltage which worsens the deflection response drastically, see Figure 5.7 right. For the case of $T_s = 0.2$ ms the gain vector is $\mathbf{K} = [3.09 \times 10^{12} \ 2.181 \times 10^{12} \ 3.45 \times 10^{11} \ -8.861 \times 10^7 \ -4.01 \times 10^7 \ 9.54 \times 10^{11} \ 16.46]$ clearly the first three elements have large positive values, resulting in positive input voltage for the actuator as seen in Figure 5.7 left.

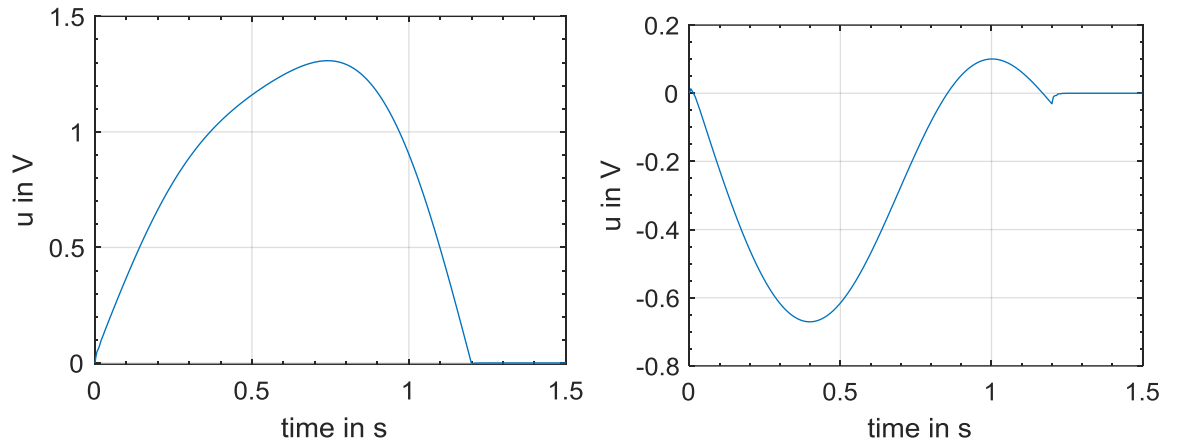


Figure 5.7. Input voltages u calculated by the discrete time observer for $T_s = 0.2$ ms (left) and $T_s = 5$ ms.

A continuous plant controlled by a discrete controller is called a sampled data system [105]. It is stated in [105–107] that the discrete regulator may lose controllability if the sampling periodicity interacts with the natural frequencies of the open-loop system \mathbf{A} , which has complex conjugate eigenvalues.

$$T_{\max} = \frac{\pi}{\omega_{\max}} = \frac{\pi}{\text{Im}[\lambda]_{\max}} \quad (5.6)$$

For the studied simply supported beam the first three Eigen frequencies are $\boldsymbol{\omega} = [24 \ 72 \ 159] \times 2\pi \text{ s}^{-1}$, where the i -th element of $\boldsymbol{\omega}$ is the i -th eigen frequency, which results in the

corresponding maximum sampling times vector $\mathbf{T}_{\max} = [0.02 \ 0.007 \ 0.0032]$ s. Though when using 3 modes the sampling time should be lower than 3.2 ms so that the optimal control can be designed. It also has to be mentioned that if only the first mode is utilised to calculate the optimal discrete time regulator with $T_s = 10$ ms this still results in a negative control voltage history. It might difficult to control the system even close to the maximum sampling times \mathbf{T}_{\max} [108].

Another influence on the feasibility of the solution is the location of the actuator, which is with $x_a = 0.5$ m not optimal. The first mode has its highest deflection in the middle of the beam at $x = 0.3$ m. If x_a is chosen to be $x_a = 0.25$ m, only the first two modes are used and $T_s = 10$ ms, $\mathbf{K} = [215.07 \ -1665.74 \ -0.53 \ 0.93 \ 0.015]$, which results in an input voltage illustrated in Figure 5.8 right.

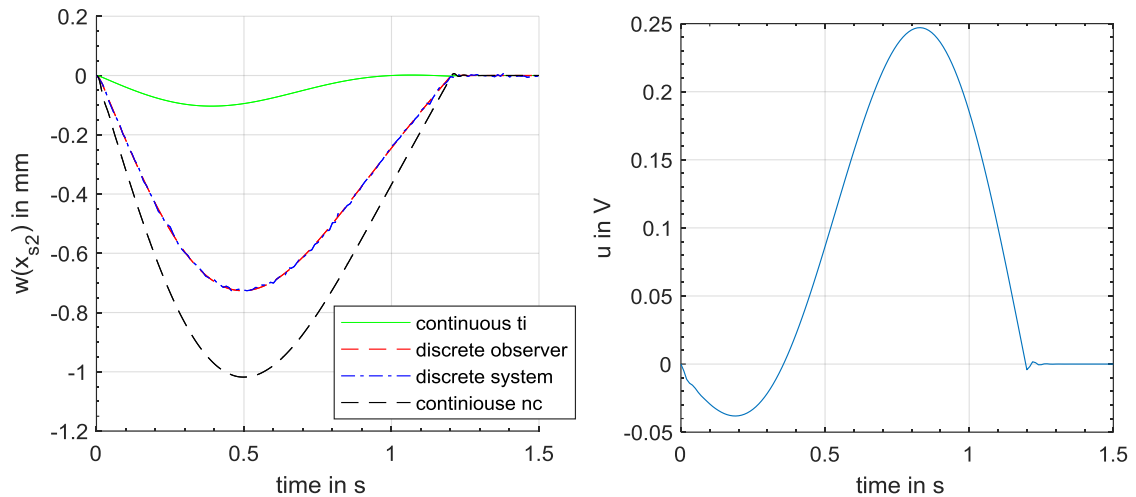


Figure 5.8. Comparison of the deflection history at $w(x_{s2})$ for the time-invariant continuous control (green continuous), for the discrete observer (red dashed), for the discrete system (blue dash-dotted) and the continuous uncontrolled structure (black dashed) (left), input voltage of the discrete time-invariant observer (right).

It can be noticed that the errors between the continuous modes and the discrete modes are still high in these configurations, see Figure 5.9. Further it can be seen that the state velocities of the discrete time-variant system and the time-invariant observer differ.

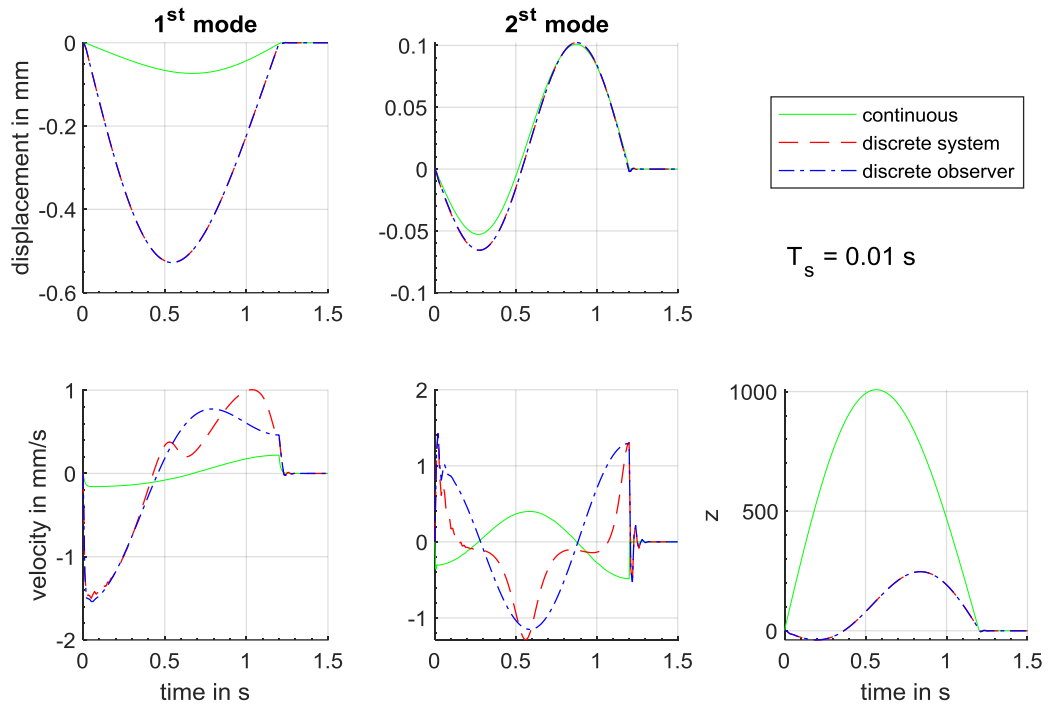


Figure 5.9. Modal coordinates of the continuous system (green continuous) and the discrete system (red dashed) and the observer (blue dot-dashed) for $T_s=10$ ms and $x_a = 0.25$ m.

Although the discrete time optimal regulator might not be a suitable method to control the sampled data system other techniques could be applied like pole placement or other hardware could be used with faster possible sampling times.

Up to this point the error due to discretisation is too high and a reliable control of the structure with $x_a = 0.5$ m cannot be accomplished by this full state observer technique and high sampling times of at least $T_s = 5$ ms. The error due to discretization is too high.

Because of the easier way to implement the estimation based on mode shapes and the possibility to implement the finite time optimal control, this technique will be utilised in the further study. It can be utilised for the feedback control and the states can be estimates without the knowledge of the load's mass and velocity. Also, the mode shapes obtained for the open loop system with the time-invariant observer look promising, the implementation of an integrated full-state feedback and observer for the time-varying system proved to be challenging.

5.2 Experimental Results for the Optimal Control Implementation

The following results of the finite-time optimal control for the simply supported beam were published in [28]. The optimal gains of the finite time-varying and time-invariant control are calculated numerically in MATLAB and stored on a CompactRIO embedded controller. With input from the laser displacement sensors (optoNCDT 1700 and optoNCDT 1610), the states are estimated in real time every 15 ms and the output voltage is calculated and sent to the power amplifier (Data Physics PA30E) for the actuation of the electrodynamic shaker (Data Physics V4).

For the time-invariant control, the constant gain is calculated, neglecting the time-varying parts in system equation (2.36).

$$\mathbf{A} = \begin{bmatrix} \mathbf{0}_{n \times n} & \mathbf{I}_{n \times n} & \mathbf{0}_{n \times 1} \\ -\mathbf{M}^{-1}\mathbf{K} & -\mathbf{M}^{-1}\mathbf{D} & \gamma\mathbf{M}^{-1}\boldsymbol{\psi}(x_a) \\ \mathbf{0}_{1 \times n} & \mathbf{0}_{1 \times n} & -\alpha \end{bmatrix}; \quad \mathbf{B} = \begin{bmatrix} \mathbf{0}_{n \times 1} \\ \mathbf{0}_{n \times 1} \\ \beta \end{bmatrix}; \quad (5.7)$$

The actuator is located at $x_a = 0.5$ m. The error and performance index are defined as $\mathbf{Q} = \text{diag}(1000, 100, 10, 0.1, 0.01, 0.01, 0)$ and $\mathbf{R} = 0.00009$ for the time-invariant control as well as for the time-varying control. The terminal cost matrix is defined as $\mathbf{F} = \mathbf{Q}$.

The displacement response of the supporting structure is mainly induced by the first mode. This knowledge was utilised by defining the error performance matrix \mathbf{Q} , setting higher weight toward the first modes.

The weight of the moving masses used in the experiments ranges from 0.261 kg to 0.509 kg. The masses are accelerated by a ramp and move over the simply supported beam structure at approximately constant speed. The value of the speeds used is between 0.3 ms^{-1} and 0.55 ms^{-1} . The actuator is located at $x_a = 0.5$ m, which is not the optimal position in terms of maximum deflection reduction making it even more necessary to employ the time-varying control solution [29]. The performance of the control methods is assessed by using the maximum absolute value of the displacement at the sensor location x_{si} .

Of the three available sensor locations $x_{s2} = 0.25$ m is chosen for further evaluation of the control methods. It displays the maximum deflection of the beam, as seen in Figure 2.7, as well as the deflection at the moving coordinate vt (Figure 5.10).

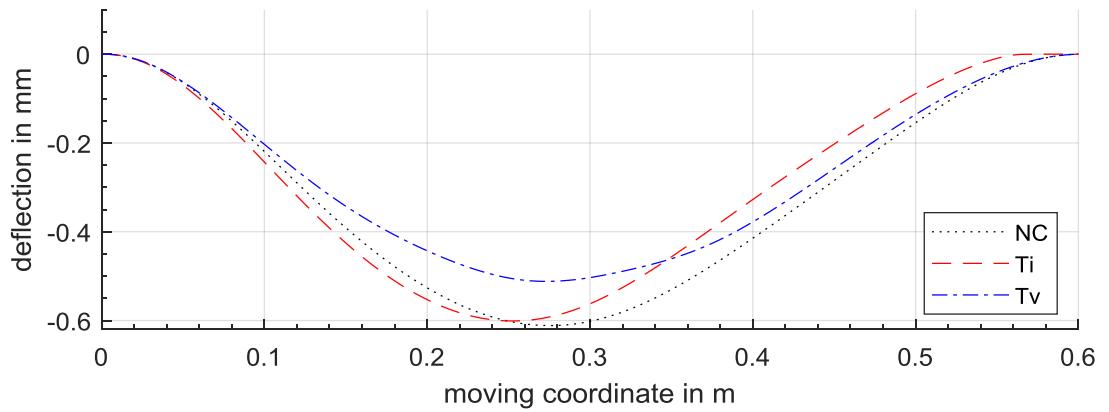


Figure 5.10. Numerical deflection of the moving coordinate vt of the mass $m = 0.5$ kg travelling with velocity $v = 0.3 \text{ ms}^{-1}$, no control (NC), time-invariant control (Ti) and time-varying system control (Tv).

Following Figure 5.1 it is clear that a full state feedback controller cannot be used given the lack of accuracy of the state estimation. Also, the controllability matrix of the system (15) is not full rank which indicates that not all of the states might be controllable as well. The best matches of the modal coordinates towards the numerical model are achieved for the estimated states $[q_1 \ q_2 \ \dot{q}_1]$, see Figure 5.1. For the convergence of the calculation of the finite time optimal control $\mathbf{u}(t)$ three modes are needed.

It has to be mentioned that already two modes can represent very accurately the deflection response of a one span beam where no electrodynamic shaker is added to the structure. The difference in the maximum response along the moving coordinate is 1.14% , see Figure 5.11.

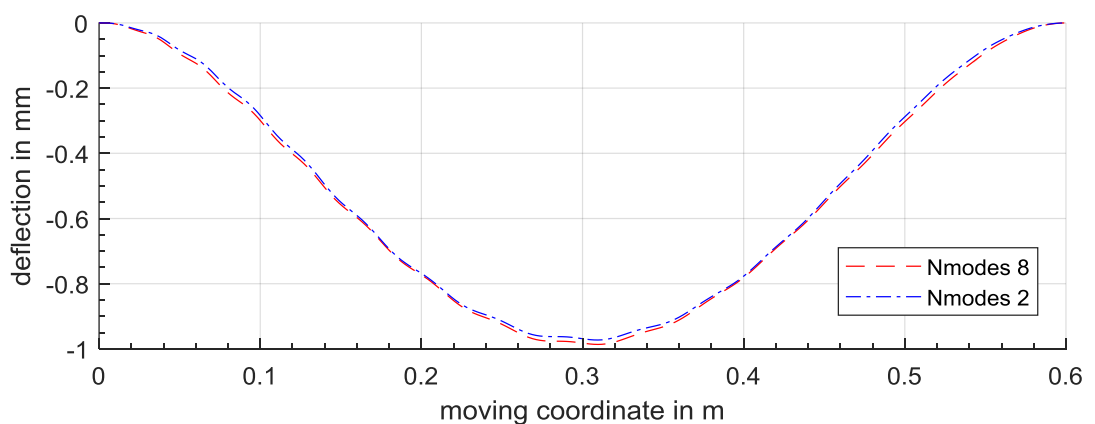


Figure 5.11. Time history of the deflection response of the simply supported beam, $m = 0.261$ kg, $v = 0.55 \text{ ms}^{-1}$.

If an electrodynamic shaker is added to the structure, more modes might be needed to represent the deflection response accurately. The actuator is modelled with a stiffness $k = 3600 \text{ Nm}$. With a very stiff actuator the beam behaves like a two-span beam, see section 2.1.1 For this kind of structure at least three modes are needed to represent the deflection response accurately. Figure 5.12 represents the deflection response along the moving coordinate for a mass $m = 0.261 \text{ kg}$ moving at a speed $v = 0.55 \text{ ms}^{-1}$.

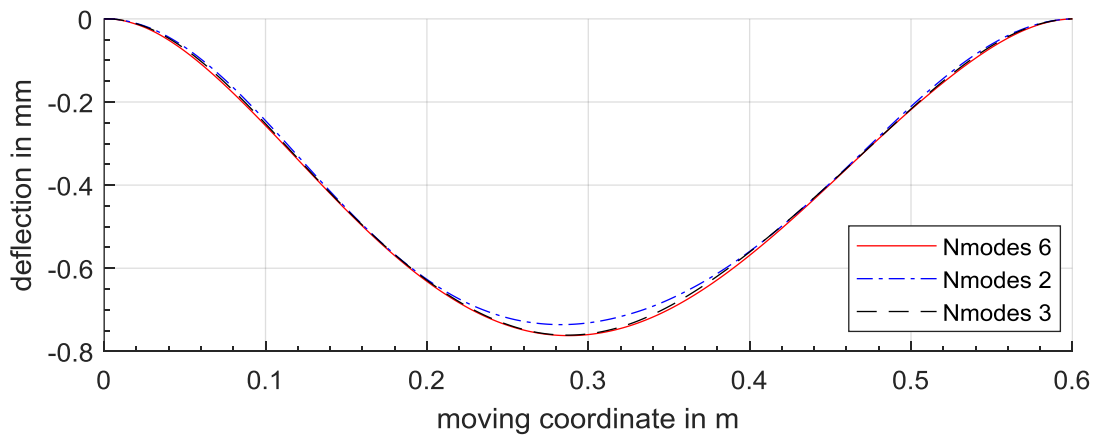


Figure 5.12. Deflection response mass $m = 0.261 \text{ kg}$ along the moving coordinate of the beam modelled with six modes (red continuous), two modes (blue dash-dotted) and three modes (black dashed).

The influence on the deflection reduction, using a reduced order controller, is considered for the mass $m = 0.261 \text{ kg}$ moving at a speed $v = 0.55 \text{ ms}^{-1}$. Three runs were taken per method. The value for the maximum displacement was averaged over the three runs. Figure 5.13 displays the experimental relative maximum deflection at sensor x_{s2} for the time-invariant control method (left) in comparison with the time-varying control method (right) using different combinations of controlled states. It can be observed that a time-invariant controller only using one state q_1 provides a reduction of the maximum deflection of about 15%. The deflection reduction decreases even more when using more states leading to even a slight increase when using all states, which might be due to inaccuracies of the mode estimation. In contrast, the time-varying control method is applicable for the states $[q_1 \ q_2 \ \dot{q}_1]$ as well, with a reduction of about 15%. Using only the first state results in the best deflection reduction at x_{s2} of about 20%. Although using further states results in a complete solution of

the problem, due to the lack of accuracy of the estimated states, the beam deflection is not improved. A different value of \mathbf{Q} with an even higher weight towards the first modal displacement and modal velocity might lead to a higher reduction of the deflection if more of the states are used.

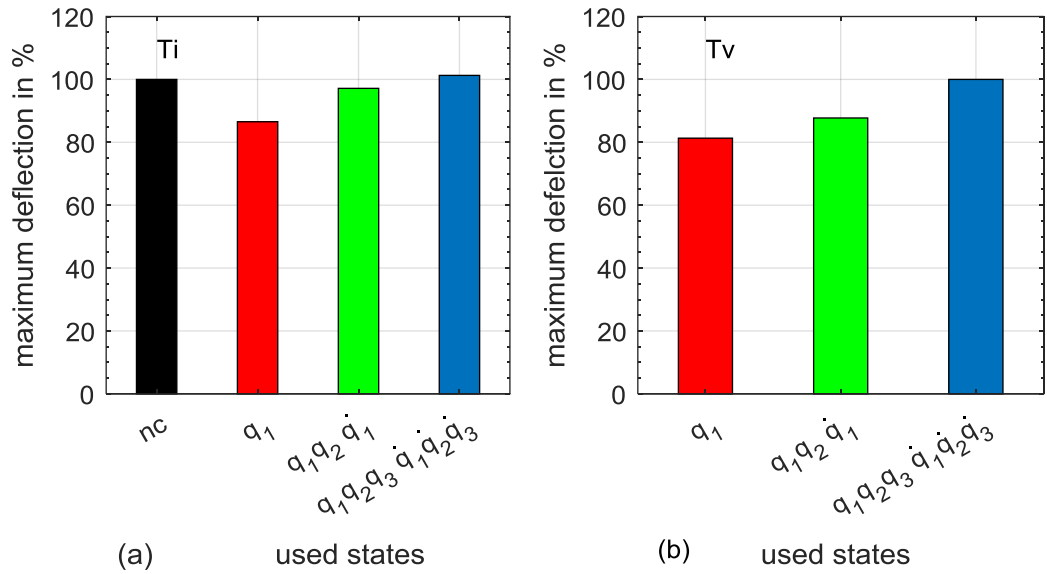


Figure 5.13. Relative experimental maximum deflection measured at x_{s2} normalised to the uncontrolled structure (nc) of the time-invariant control (Ti) (a) and the time-varying control (Tv) (b) from using one state to using all states.

Figure 5.14 illustrates the theoretical deflection at x_{s2} using different states with the two control approaches. In theory using states $q_1 q_2 \dot{q}_1$ with the time-varying control improves the deflection response at x_{s2} slightly better, compared to using only q_1 . Although using only q_1 with the tv control leads to the better results, see Figure 5.13 in the following investigation states $q_1 q_2 \dot{q}_1$ are used. In the beginning it was the aim to include the modal velocity \dot{q}_1 . Velocity feedback increases the damping in the system. In theory the use of the second mode q_2 improves the deflection response as well slightly, Figure 5.14. The discrepancy between the theoretical and the experimental results in this regard might have its origin in the inaccuracy of the estimation technique, see Figure 5.1. If all three modes are used, the need for the tv control becomes very clear. The ti control worsens the deflection at x_{s2} , see Figure 5.15. The deflection response only improves around the actuator location x_a .

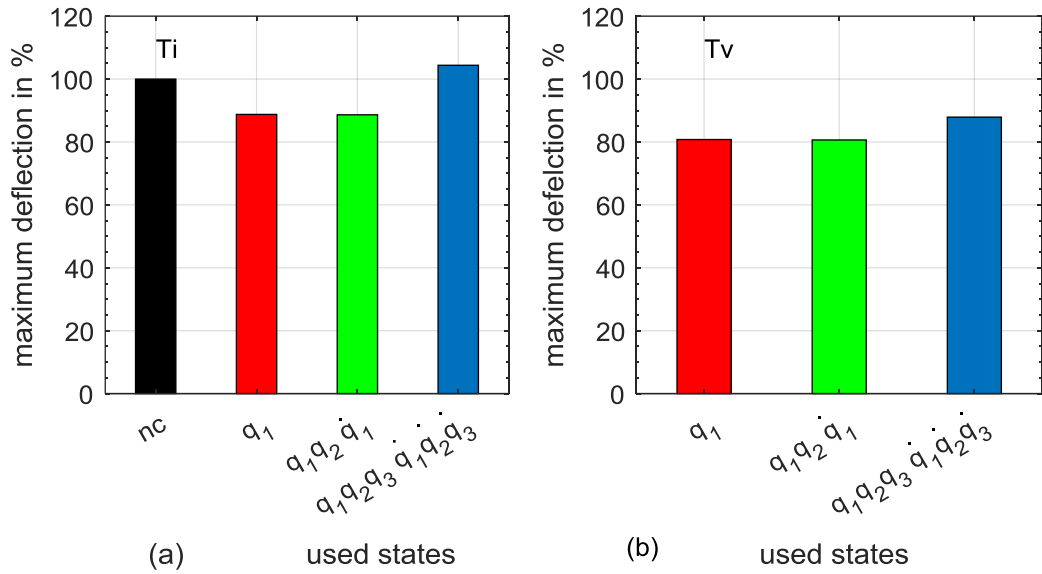


Figure 5.14. Theoretical relative maximum deflection measured at x_{s2} normalised to the uncontrolled structure (nc) of the time-invariant control (Ti) (a) and the time-varying control (Tv) (b) from using one state to using all states.

Although it might be better to use only state q_1 for the maximum reduction of the deflection, it was also shown that more modes can be included in the control approach, which might be beneficial for higher speed or at multi span beams.

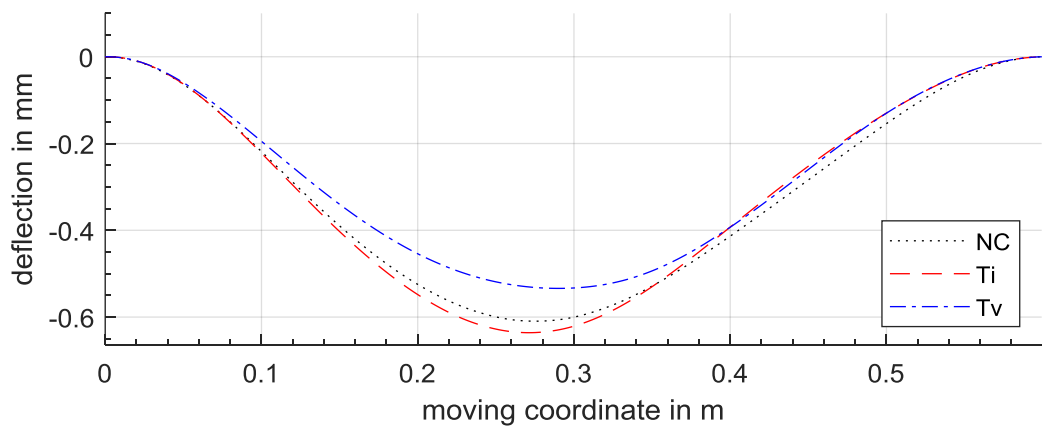


Figure 5.15. Deflection response mass $m = 0.261$ kg along the moving coordinate of the beam modelled with all three modes no control (black dotted), time-invariant (red dashed) and time-variant (blue dash-dotted).

Figure. 5.16 shows the time histories of the varying gains k_1 , k_2 and k_4 corresponding to the states $[q_1 \ q_2 \ \dot{q}_1]$. The tests were run for the masses $m = 0.261$ kg, $m = 0.371$ kg and $m = 0.509$ kg travelling at the speed $v = 0.3$ ms⁻¹. Towards the time of $t = 0.8$ s the travelling mass reaches the moving coordinate $vt = 0.24$ m where the beam has the highest deflection (see Figure 5.10).

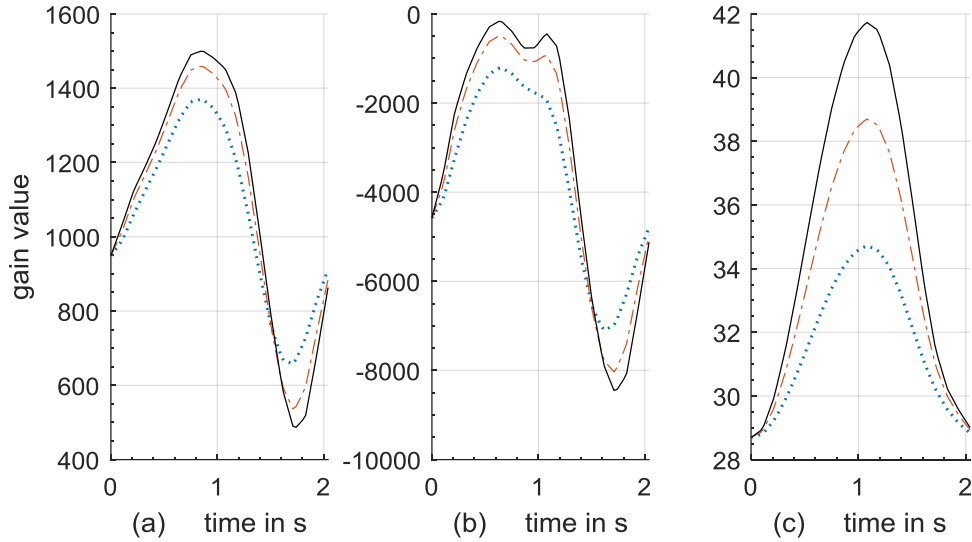


Figure. 5.16. Development of the time-varying gains $k_1(t)$ (a), $k_2(t)$ (b) and $k_4(t)$ (c) for the three different masses $m = 0.261$ kg (blue dotted), $m = 0.371$ kg (red dashed) to $m = 0.509$ kg (black continuous) at velocity $v = 0.3$ ms⁻¹.

Consequently, the gains k_1 and k_2 increase up to this time. With that, a higher actuation is achieved when the mass excites the beam most. Subsequently the gains decrease. When the mass passes by $x_a = 0.5$ m the gains k_1 and k_2 reach their minimum. The least amount of force is required to counteract the influence of the moving mass. In this way, an effective and stable control is achieved. In the following investigations the states $[q_1 \ q_2 \ \dot{q}_1]$ are used for control. This represents a fair compromise between completeness of the solution and reduction of the structural deflection.

To assess the stability of the time-varying system $(\mathbf{A}(t)-\mathbf{B}(t)\mathbf{k}(t))$, where the proposed reduced order controller is applied, its eigenvalues are calculated at certain time steps. Figure 5.17 illustrates the course of the first four resulting complex conjugate pole pairs. During the time the mass $m = 0.509$ kg travels with $v = 0.55$ ms⁻¹ over the beam the Eigenfrequencies of the modes change, the poles circle in the negative left half plane around the time-invariant poles (black crossed).

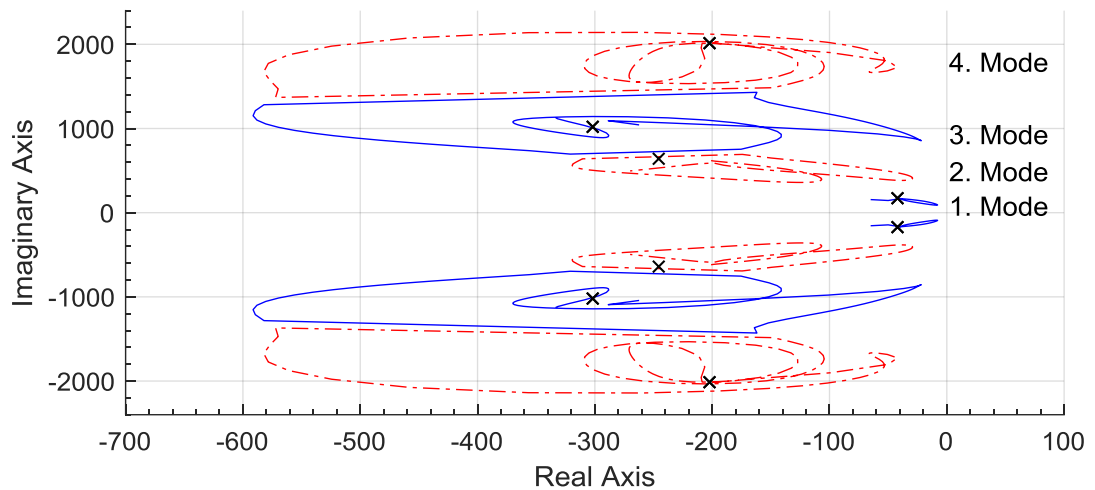


Figure 5.17. Time history of the poles of the time-varying controlled system, first and third mode (blue continuous), second and fourth mode (red dashed), poles of the time-invariant system (black crossed), $m = 0.5$ kg, $v = 0.55$ m/s.

Figure 5.18 shows the poles of the simulated system with the reduced order controller and a travelling mass $m = 0.509$ kg. For the increased travelling speed of 5.6 m/s one pole pair moves into the real half plane causing instability. At this margin the full state controller stays stable with all poles in the negative plane. Especially the first dominant pole pair moves less towards the imaginary axis. Higher velocities and weights also cause with the full-state control instability. Likewise increasing the mass over $m = 6.5$ kg with a low speed of 0.55 m/s lets some poles move into the real half plane. In this way the theoretical stability margins of the system can be simulated. The additional actuator pole located at -10000 on the real axes is not shown in the figures.

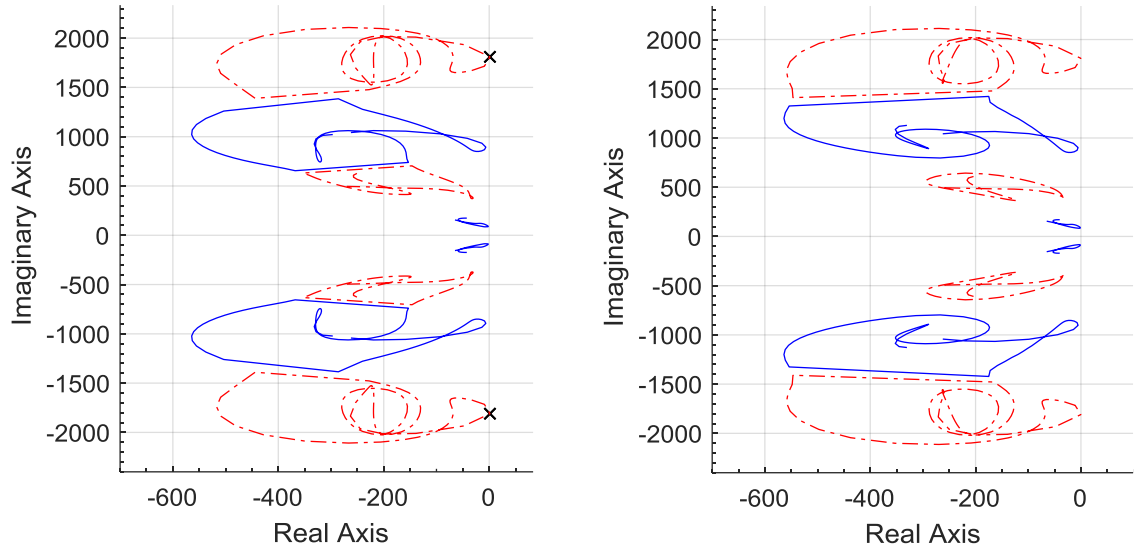


Figure 5.18. Comparison of the first four poles of the time-varying system with the reduced order controller (left) and with the full state controller (right) unstable poles (black asterisks), $m = 0.5$ kg, $v = 5.6$ m/s.

In order to assess the reduction of the maximum deflection at sensor location x_{s2} depending on the used control method three masses were tested at two speeds $v = 0.3$ ms⁻¹ and $v = 0.55$ ms⁻¹. Five runs for each mass were averaged for the calculation of maximum deflections. The relative maximum deflections in Table 5.1 show a small reduction for the time-invariant control of around 3% for all the masses. The time-varying control shows a better performance for all the tests with a deflection reduction from 12% for $m = 0.261$ kg to 17% for $m = 0.509$ kg, with a higher reduction for higher masses.

Figure 5.19 illustrates the results obtained for mass $m = 0.509$ kg with a travelling speed of $v = 0.3$ ms⁻¹. It also shows a good agreement between the numerically calculated results and the experimentally measured deflection $w(x_{s2})$. There is a small mismatch after the mass leaves the beam due to the not modelled back electro-magnetic force (Back EMF) of the electromagnetic shaker [94].

Table 5.1. Relative maximum deflection at x_{s2} for different masses travelling at $v = 0.3$ ms^{-1} in percent.

mass m in kg	no control	time-invariant	time-varying
0.261	100	96.9	88
0.371	100	97.7	85.7
0.509	100	96.6	83.2

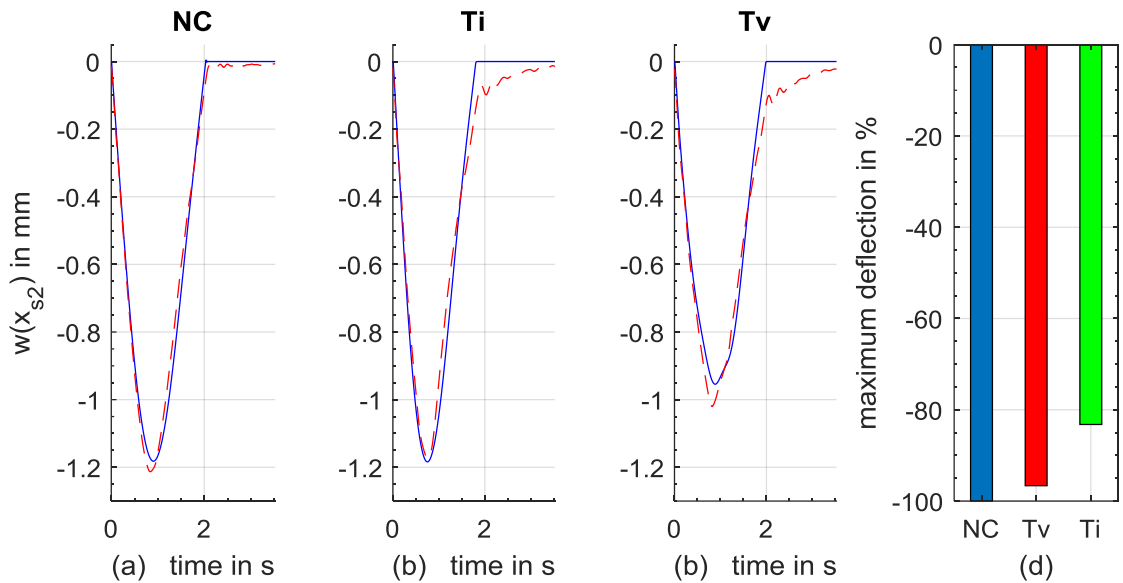


Figure 5.19. Mass $m = 0.509$ kg moving with $v = 0.3$ ms^{-1} , comparison of the displacement $w(x_{s2})$ for the numerically calculated data (blue continuous) and the experimentally measured data (red dashed), for the case without control (a), with the time-invariant control (b), with the time-varying control (c) and the values of the relative maximum deflection in percent (d).

Figure 5.20 illustrates the time history of the experimental control inputs $u(t)$ belonging to this example. It is noticed that the time-variant control has a high actuation especially in the first half of the travelling time whereas the time-invariant control is much less active in the first half. The voltage at the electrodynamic shaker is lower than the time history of the voltage at the compactRio. This might be due to back-EMF. After the mass has left even negative forces can be noticed which pull the beam down, see also Figure 5.19.

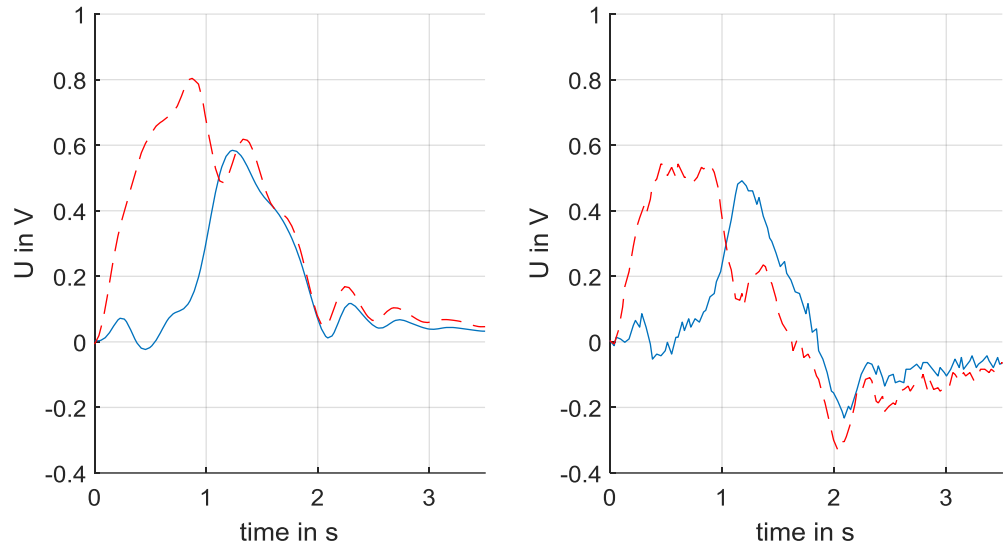


Figure 5.20. Time history of the experimentally measured control input at the compactRio (left) and at the electrodynamic shaker (right), time-invariant (blue continuous) and time varying (red dashed).

Table 5.2 shows the relative maximum deflections for three masses moving with a higher speed $v = 0.55 \text{ ms}^{-1}$. The invariant control reduces the maximum deflection only by 1% for mass $m = 0.261 \text{ kg}$ and by 8% for mass $m = 0.509 \text{ kg}$. In contrast, the time-varying control achieves a reduction of approximately 18% for mass $m = 0.509 \text{ kg}$. Again, it can be observed that the control is more effective for higher masses, as a higher deflection results in higher actuation. The results are similar for the two investigated velocities.

Table 5.2. Relative maximum deflection measured at x_{s2} for different masses travelling at $v = 0.55 \text{ ms}^{-1}$ in percent.

mass in kg	no control	time-invariant	time-varying
0.261	100	99.2	87.2
0.371	100	97.1	83
0.509	100	92	82.1

Figure 5.21 shows one example of the beam deflection at sensor location x_{s2} when mass $m = 0.261 \text{ kg}$ moves with velocity $v = 0.55 \text{ ms}^{-1}$. The measured deflections show a good match with the numerical model for all the tests with the only discrepancy observed after the mass leaves the structure due to back EMF of the electro-dynamic shaker. The time-varying

controller reaches a reduction of 13%. A stable control with reduction of the beam deflection is achieved for different masses travelling at different speeds.

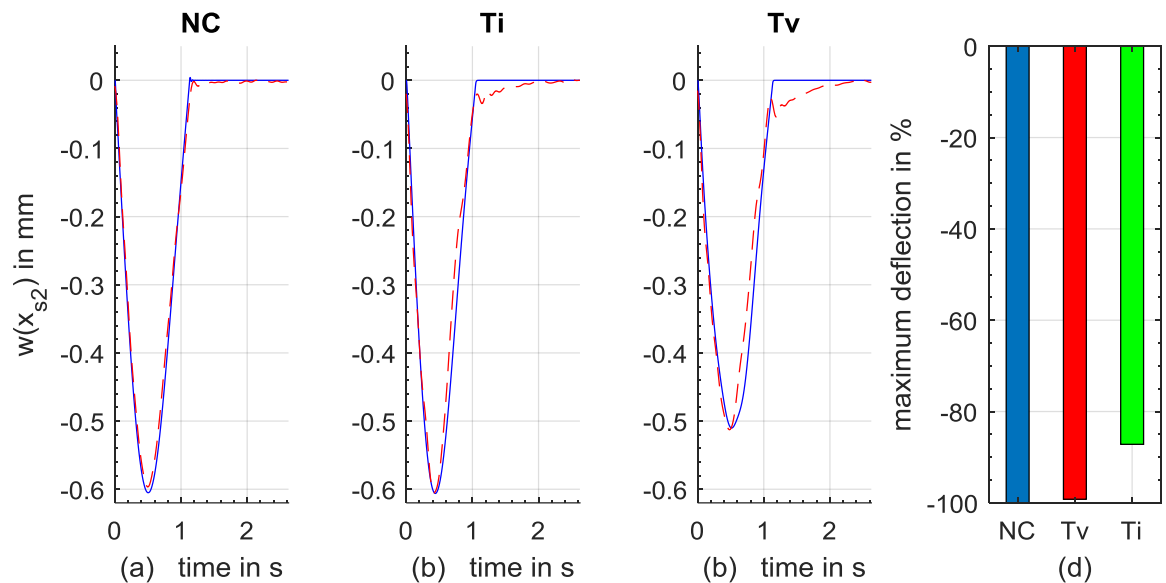


Figure 5.21. Mass $m = 0.261$ kg moving with $v = 0.55$ ms⁻¹, comparison of the displacement $w(x_{s2})$ for the numerically calculated data (blue continuous) and the experimentally measured data (red dashed), for the case without control (a), with the time-invariant control (b), with the time-varying control (c) and the values of the relative maximum deflection measured at x_{s2} in percent (d).

The reduction of the velocity might be difficult to achieve with this type of actuator. Figure 5.22 shows that the time-varying control does not lead to an increase of the positive velocity at sensor location $x(s_3)$, whereas for the time-invariant control a slight increase can be noticed. The negative velocity increases from -2 ms⁻¹ for the uncontrolled case to -2.6 ms⁻¹ for the time-invariant control and to -2.4 ms⁻¹ for the time-variant control. Additional oscillations can be noticed at all three cases compared to the numerical results. These differences could be due to the delay of the low-pass filter and the digital control system and the complex not modelled shaker dynamics.

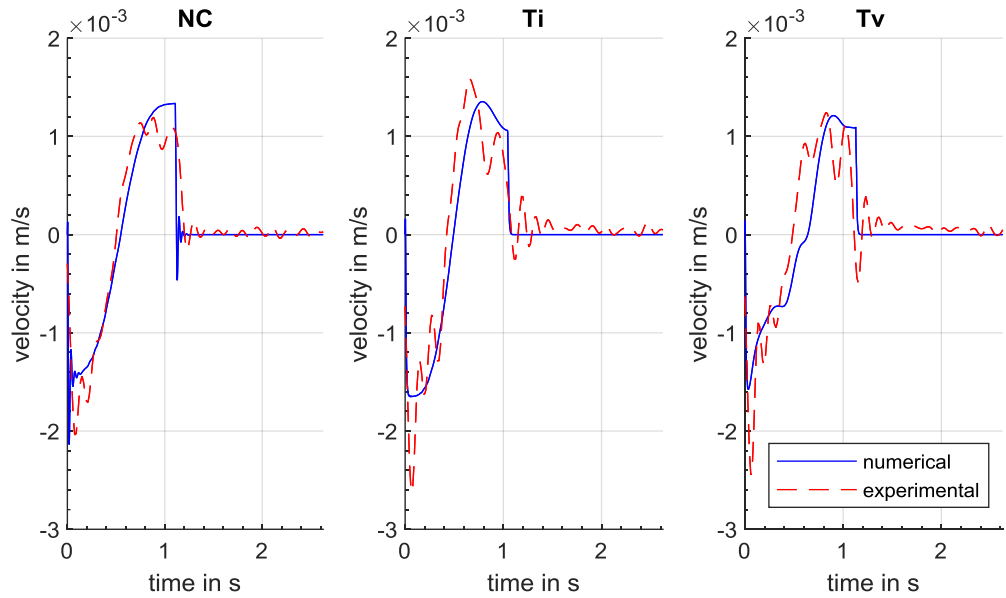


Figure 5.22. Mass $m = 0.261$ kg moving with $v = 0.55$ ms^{-1} , comparison of the velocity (v_{s3}) for the numerically calculated data (blue continuous) and the experimentally measured data (red dashed), for the case without control (a), with the time-invariant control (b), with the time-varying control (c).

5.3 Experimental Results for Variable Control Gain

Following the experimental tests, it becomes clear that the performance of the controller depends on the weight of the moving mass. This means that a control gain that was designed to achieve a good reduction for a heavy mass may provide a too high control effort for a smaller mass whereas a controller gain designed for a small mass may not be enough to provide a good reduction of the deflection for a heavier mass. Therefore, in terms of absolute deflection, the control effort required to achieve a prescribed absolute maximum deflection needs to change for the case when a small mass travels along the beam as compared to the case when a heavier mass acts upon the beam.

In this respect a gain scheduling of the control gain either as $\mathbf{k}(m)$ a function of mass or as $\mathbf{k}(m, v)$ a function depending on the mass m and speed v is tested. The masses used are $m_1 = 0.261$ kg, $m_2 = 0.322$ kg, $m_3 = 0.371$ kg and $m_4 = 0.509$ kg.

Figure 5.23 shows the effect of using the specific scheduled time-varying gains $\mathbf{k}(m_1)$, $\mathbf{k}(m_2)$, $\mathbf{k}(m_3)$ and $\mathbf{k}(m_4)$, calculated taking into account every mass, compared with the time-varying gain $\mathbf{k}(m_1)$ determined for mass m_1 and subsequently used for all masses. In this way the control switches to the specific control gain, therefore a heavier mass will have a higher control gain that will confine the deflection of the beam within a prescribed limit (in this case about 1 mm).

Figure 5.23 shows a gradual reduction of the deflection as the gain increases with the weight of the mass. With this approach, where the gains are scheduled taking into account the value of the mass, the relative maximum deflection is 10% lower compared to the unscheduled control using the gain of the first mass $\mathbf{k}(m_1)$ all over, see Figure 5.24. The performance of this method can be improved if the gains are determined taking into account the moving mass into the system equation as an augmented system, introduced in [29]. The gains can be scheduled based on deflection values in the first phase. On a real bridge-like structure, image processing or a scale can identify the actual load case of m and select the optimal gain for control.

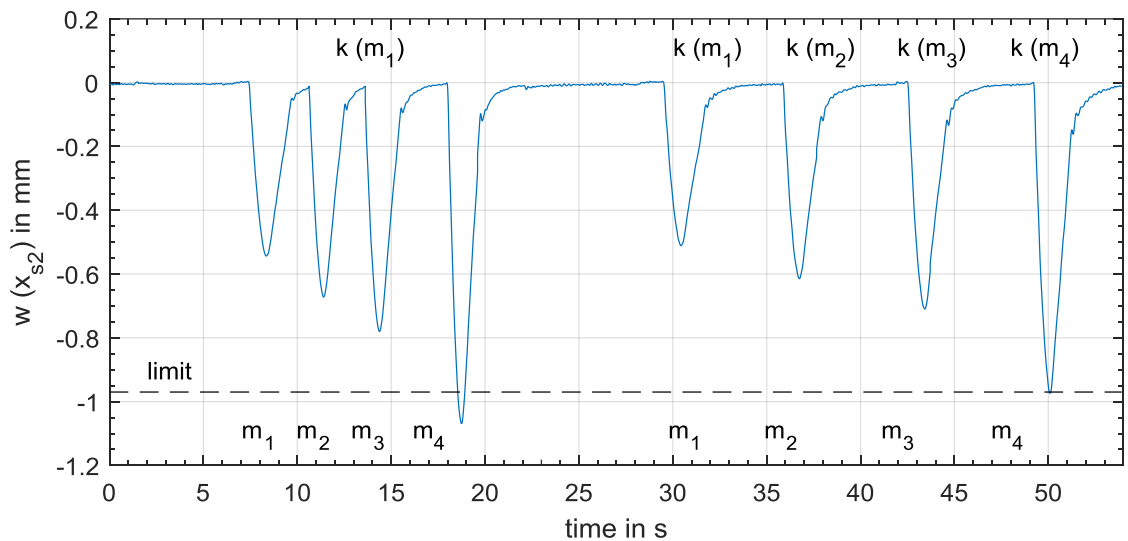


Figure 5.23. Effect of using time-varying gain $\mathbf{k}(m_1)$ (left) and scheduled for each mass specifically (right) $\mathbf{k}(m_1) - \mathbf{k}(m_4)$.

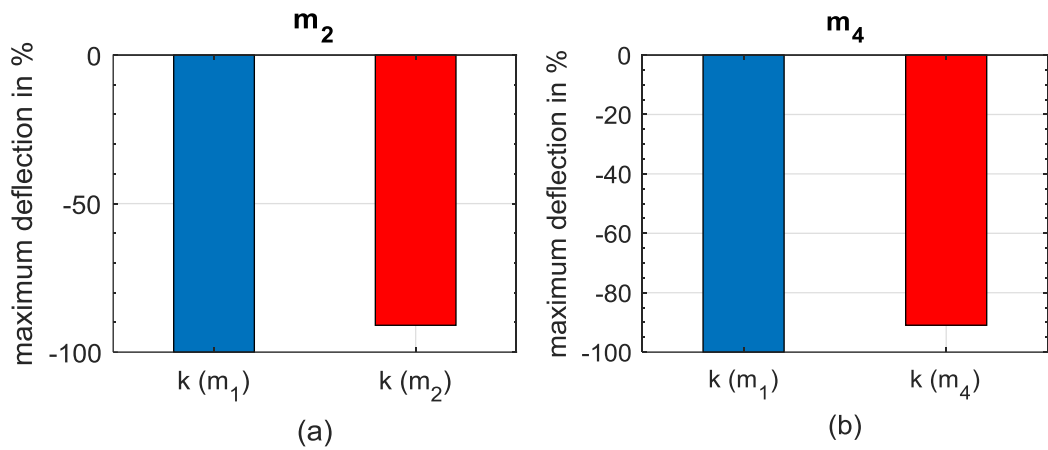


Figure 5.24. Relative maximum deflection for mass m_2 (a) and mass m_4 (b) using gain $k(m_1)$ (blue) in comparison to using the specific gains $k(m_2)$ or $k(m_4)$ (red).

Another important factor of the proposed control strategy is the ability to adapt to different velocities of the mass. The time-varying gain vector $\mathbf{k}(t,m)$ is calculated beforehand for a predetermined velocity at equal time steps and stored on the controller. By measuring the actual velocity in real time using two induction sensors before the mass enters the structure, the leaving time t_f can be determined exactly. With the given t_f the control action is stretched or compressed towards the given travelling time of the mass. The gain is then interpolated between the precalculated gain values for the actual position of the mass. Figure 5.25 illustrates the principle of the 1D interpolation in LabView, for the actual time t_{ob} , the leaving time t_f , number of elements x_f is the actual element x is calculated by $x = t_{ob} \frac{x_f}{t_f}$. With that x the interpolated k_i results. This procedure is accomplished in a loop for all elements of \mathbf{k} .

In Figure 5.26 it can be seen how the control needs to adapt to different speeds ranging from $v = 0.22 \text{ ms}^{-1}$ to $v = 0.95 \text{ ms}^{-1}$. The gain $k_1(m_4)$ calculated in real time coincides well with the numerically calculated gain.

In the previous section the finite time optimal control approach was validated experimentally. The gain scheduling control approach was studied which adopts the gain to the mass weight and speed. In the next section the moving mass will be included into the system equation to form an augmented system.

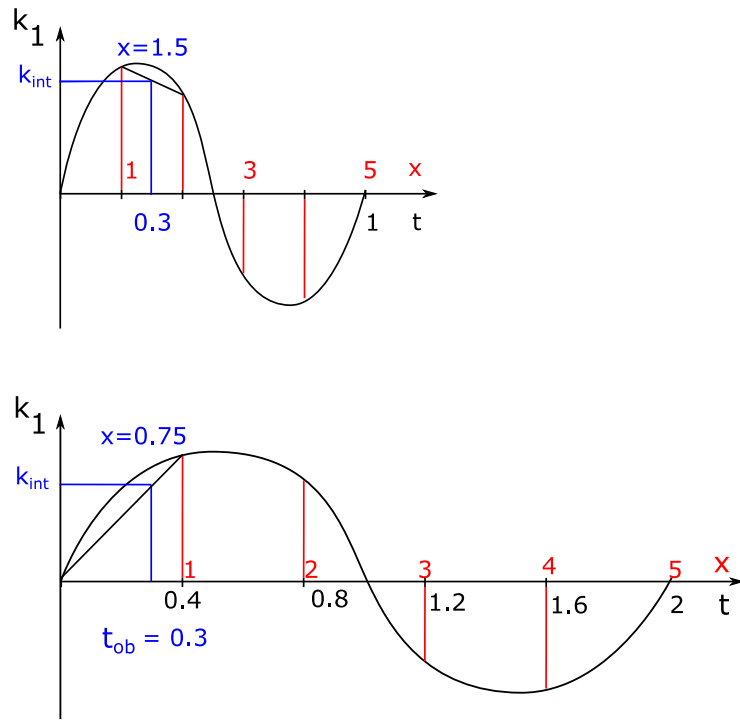


Figure 5.25. Principle of 1D interpolation in LabView.

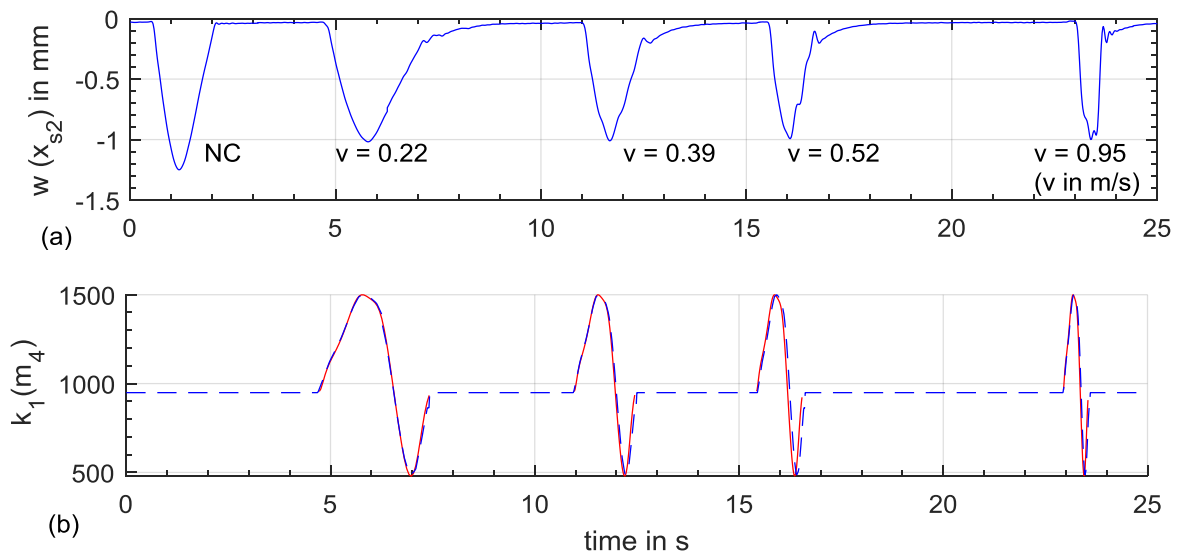


Figure 5.26. Deflection $w(x_{s2})$, no control action (NC) and with different speeds v (a); time-varying gain $k_1(m_4)$ (b) calculated in real-time (blue dashed) and numerically (red continuous).

5.4 Experimental Validation of the Optimal Control by an Augmented System

Up to this stage a particularity of the moving load problem was neglected. The modal force $mg\boldsymbol{\Psi}(vt)$ was not considered in the control synthesis. The disturbance matrix \mathbf{B}_f in (2.36) was not considered in the calculation of the optimal gain. Only the system matrix $\mathbf{A}(t)$ and the input matrix $\mathbf{B}(t)$ are part of the calculation of the Pythagorean in equation (3.8) and the optimal gain in equation (3.9). By including the disturbance matrix \mathbf{B}_f into the system matrix $\mathbf{A}(t)$ the augmented system matrix is formed as presented in [29]:

$$\mathbf{A}(t) = \begin{bmatrix} \mathbf{0}_{n \times n} & \mathbf{I}_{n \times n} & \mathbf{0}_{n \times 1} & \mathbf{0}_{n \times 1} \\ -(\mathbf{M} + \Delta\mathbf{M}(t))^{-1}(\mathbf{K} + \mathbf{K}_a + \Delta\mathbf{K}(t)) & -(\mathbf{M} + \Delta\mathbf{M}(t))^{-1}(\mathbf{D} + \mathbf{D}_a + \Delta\mathbf{D}(t)) & \gamma(\mathbf{M} + \Delta\mathbf{M}(t))^{-1}\boldsymbol{\Psi}(x_a) & -(\mathbf{M} + \Delta\mathbf{M}(t))^{-1}\boldsymbol{\Psi}(vt) \\ \mathbf{0}_{1 \times n} & \mathbf{0}_{1 \times n} & -\alpha & \mathbf{0} \\ \mathbf{0}_{1 \times n} & \mathbf{0}_{1 \times n} & \mathbf{0} & \mathbf{0} \end{bmatrix}$$

$$\mathbf{B}_m = \begin{bmatrix} \mathbf{0}_{n \times 1} \\ \mathbf{0}_{n \times 1} \\ \beta \\ \mathbf{0} \end{bmatrix}; \quad (5.8)$$

This form introduces a new state q_1 . The state variable changes herein to $[\mathbf{q}(t) \dot{\mathbf{q}}(t) z q_1]$ with the initial conditions $[\mathbf{q}(0) \dot{\mathbf{q}}(0) z(0) g \times m]$. In this way the disturbance of the load becomes part of the system. Depending on the mass an additional gain is calculated by the finite time optimal control approach.

In the following, this approach is validated experimentally. Five runs were taken per method. The average maximum deflections at x_{s2} at $v = 0.3 \text{ ms}^{-1}$ are listed in Table 5.3 for the previously presented time-varying method and the augmented time-varying control in comparison to the uncontrolled structure. The relative maximum deflection at x_{s2} ranges from 66.3% for $m_4 = 0,509 \text{ kg}$ to 67.12% for $m_1 = 0.261 \text{ kg}$ when using the augmented time-varying control. Table 5.4 lists the relative maximum deflection at x_{s2} for the control methods now for speed $v = 0.55 \text{ ms}^{-1}$. The maximum deflection is around 62% for all three masses for the augmented time-varying control. The maximum deflection is up to 20% lower compared to the original time-varying control.

Table 5.3. Relative maximum deflection at x_{s2} for different masses travelling at $v = 0.3$ ms^{-1} in percent for the uncontrolled system.

mass m in kg	no control	time-varying	tv augmented
0.261	100	88	67.12
0.371	100	85.7	67.85
0.509	100	83.2	66.29

Table 5.4. Relative maximum deflection at x_{s2} for different masses travelling at $v = 0.55$ ms^{-1} in percent.

mass m in kg	no control	time-varying	tv augmented
0.261	100	87.2	62.83
0.371	100	83	61.82
0.509	100	82.1	62.43

Figure 5.27 illustrates the time history of the deflection $w(x_{s2})$ numerically (red dashed) and experimentally obtained (blue continuous) for the augmented control (Aug) system compared with the time-varying control (Tv) and the case of an uncontrolled structure. Mass m_1 is moving on the structure with a low speed of $v = 0.3$ m/s. The maximum deflection of the augmented system is 33% percent lower compared to the uncontrolled structure.

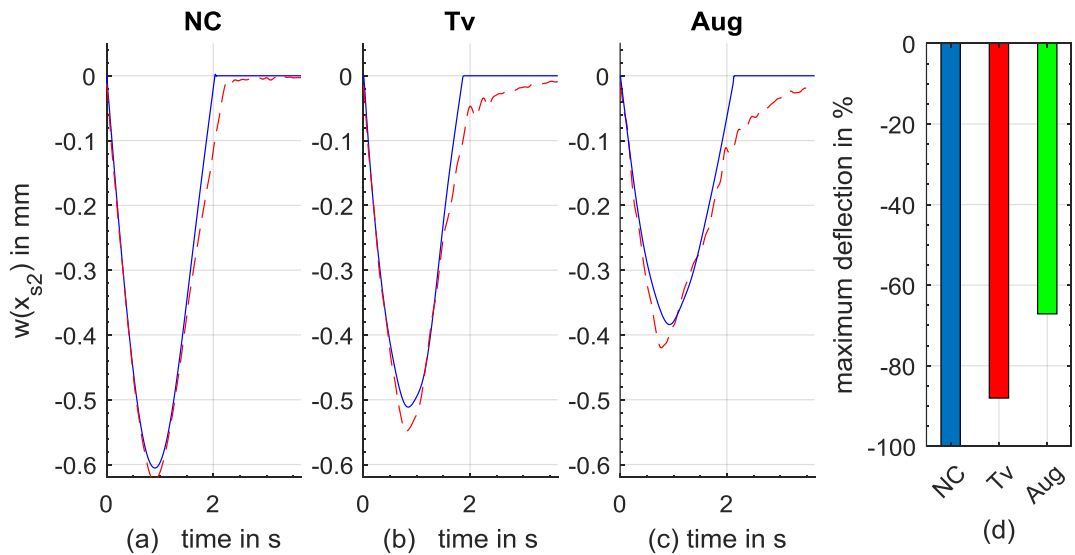


Figure 5.27. Mass $m_1 = 0.261$ kg moving with $v = 0.3$ ms⁻¹, comparison of the displacement $w(x_{s2})$ for the numerically calculated data (blue continuous) and the experimentally measured data (red dashed), for the case without control (a), with the time-variant control (b), with the time-varying augmented control (c) and the values of the relative maximum deflection measured at x_{s2} in percent (d).

Figure 5.28 compares the deflection response $w(x_{s2})$ in the augmented system with time-varying control and the uncontrolled structural response for the case of mass $m_4 = 0.509$ kg moving with a speed $v = 0.55$ m/s. The maximum deflection is reduced by 38%. The gain can be switched in the same manner as presented in section 5.3. The switching of the gains is done manually in the LabView front panel. Due to the augmented system a higher impact of the mass specific gains on deflection reduction can be noticed in Figure 5.29. The adaptation toward the speed can be done similarly in real-time as presented before.

The augmented control approach proved very efficient with a reduction of the maximum deflection of about 38%. The disturbance force gets included into the feedback as a state variable. This state variable is not prone to sensor noise, though the additional gain does not destabilize the system.

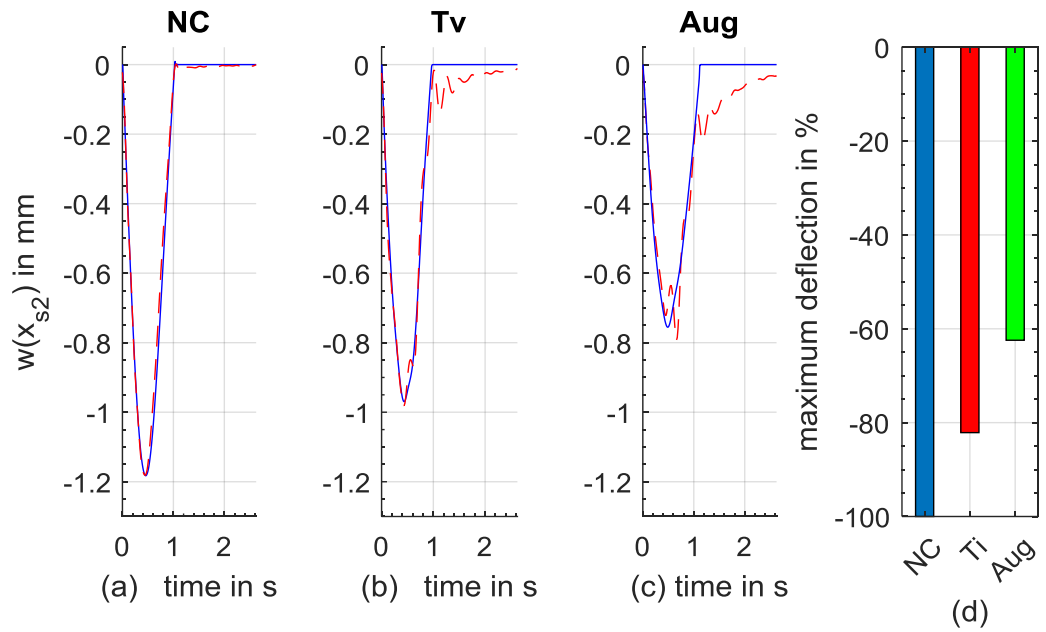


Figure 5.28. Mass $m_4 = 0.509$ kg moving with $v = 0.55$ ms^{-1} , comparison of the displacement $w(x_{s2})$ for the numerically calculated data (blue-continuous) and the experimentally measured data (red dashed), for the case without control (a), with the time-variant control (b), with the time-varying augmented control (c) and the values of the relative maximum deflection measured at x_{s2} in percent (d).

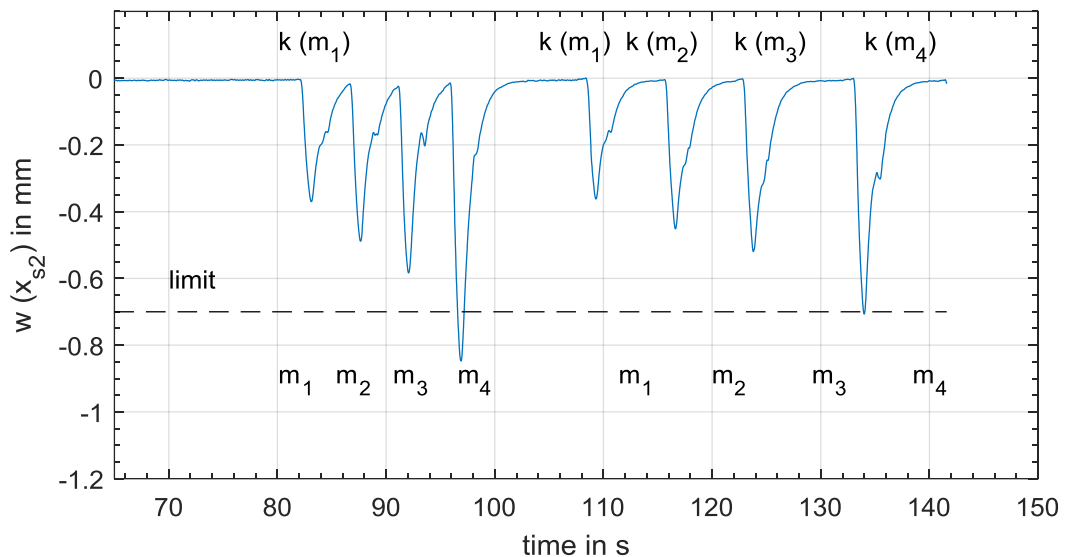


Figure 5.29. Effect of using time-varying gain $\mathbf{k}(m_i)$ (left) and scheduled for each mass specifically (right) $\mathbf{k}(m_1) - \mathbf{k}(m_4)$ for the augmented control.

5.5 Concluding Remarks

In chapter 5, the finite time optimal control approach was validated on a small-scale rig of a simply supported beam. When using state feedback control methods it is crucial to estimate the states with sufficiently high accuracy in the given sampling time. Especially the estimation method using the mode shapes proved efficient, whereas the full-state observer, especially the discrete optimal control approach failed because sufficient small sampling times were not reachable by the hardware.

The finite time optimal control approach was implemented successfully by using a reduced number of estimated states. Especially the augmented optimal control was able to accomplish the task of reducing the beam deflection. Further it is possible to schedule the precalculated gains to a specific speed in real-time as well as to a given mass. These can be a foundation for an application of a vibration control, which can react to specific load cases of a moving load structure.

In the next chapter a proportional feedback control is validated experimentally using MFC-actuators on a simply supported beam as well as on two-span continuous beam.

6 Case Study 2: Proportional Displacement Feedback Control

A straightforward control method is the proportional feedback control illustrated in Figure 6.1. The displacement $w(x_{si}, t)$ is measured at the location collocated to the actuator. Additionally, to smoothen the displacement signal a Butterworth filter of 10th order with a cut-off frequency of 10 Hz is applied. The input for the plant u is calculated by the product of the filtered displacement, the control gain k and the gain of the amplifier g_a , see equation (6.2).

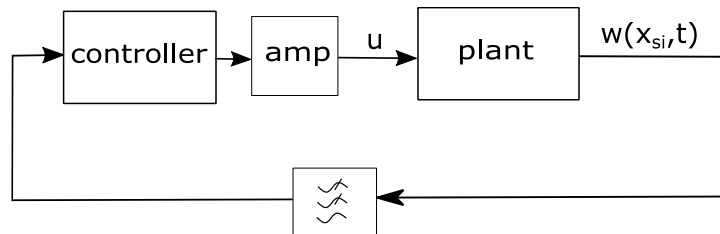


Figure 6.1. Block diagram of the displacement feedback control for the one-span beam.

Preumont emphasises in [42] the importance of a collocated sensor actuator pair. This leads to an alternating pole-zero pattern whereas non-collocated systems can lead to pole zero flipping. The property of collocation can guarantee stability for a wide range of single-input-single output control systems even if the systems are subject to large perturbations. This is because the root locus keeps its general shape and stays entirely within the left half plane. Generally the gain should be raised carefully to see experimentally, if the system becomes unstable. By that, reaching the gain margin, the system might become unstable only for a short period of time, when the mass is traveling on the structure and in is not excited in destructive resonance. Stability can also be tested for the time-invariant system with well-known methods. The open-loop system has theoretically a gain margin of $2.6783e+06$ and a phase margin of ∞ . Robustness with the influence of the moving mass will be tested with experimental tests.

The equation of motion of a simply supported beam controlled by an MFC- actuator is

$$(\mathbf{M} + \Delta\mathbf{M})\ddot{\mathbf{q}} + (\mathbf{K} + \Delta\mathbf{K})\mathbf{q} = u(t)M_p(-\boldsymbol{\psi}'(x_1) + \boldsymbol{\psi}'(x_2)) - N\boldsymbol{\psi}(vt) \quad (6.1)$$

The input $u(t)$ is calculated by

$$u(t) = -k g_a w(x, t) \quad (6.2)$$

where g_a is the gain of the amplifier. $w(x, t)$ is taken in mm.

An extension of the proportional displacement feedback is the cubic displacement feedback.

$$u(t) = -k g_a w(x, t)^3 \quad (6.3)$$

This feedback rule might be more effective for higher disturbances and can set the maximum deflection under a specified limit. For lower disturbances less control action is applied.

6.1 Simply Supported Beam Controlled by a Piezoelectric Actuator

The experimental set-up presented in section 0 is used and the linear displacement feedback control equation (6.2) and the cubic displacement feedback control equation (6.3) are utilised. The deflection $w(x_{s2})$ at sensor location $x_{s2} = 0.3$ m is taken and fed back to control the structure. A constant control gain $k = 2$ is utilised for both control approaches.

In order to assess the reduction of the maximum deflection at sensor location x_{s2} the four masses $m_1 - m_4$ were tested at speeds between $v = 0.3$ m/s and $v = 0.55$ m/s. The slightly different speeds between the runs might not have a very high influence on the deflection results. Previous results in Table 5.1 and Table 5.2 showed only a very slight difference between the speeds of $v = 0.3$ m/s and $v = 0.55$ m/s, for the maximum deflection. Nevertheless, higher vibrations for higher travelling speeds $v > 0.5$ m/s for m_4 can be noticed when the mass is leaving, see Figure 6.3.

Figure 6.2 illustrates the time history of displacement responses $w(x_{s2})$ for mass $m_1 = 0.261$ kg, comparing uncontrolled structure, the liner feedback control and the cubic feedback control. A good match between the numerical and the experimental data is accomplished. As expected, the cubic control is less efficient for this small mass. The maximum displacement is reduced by approx. 5% whereas the linear control reduces the maximum deflection by approx.. 10%.

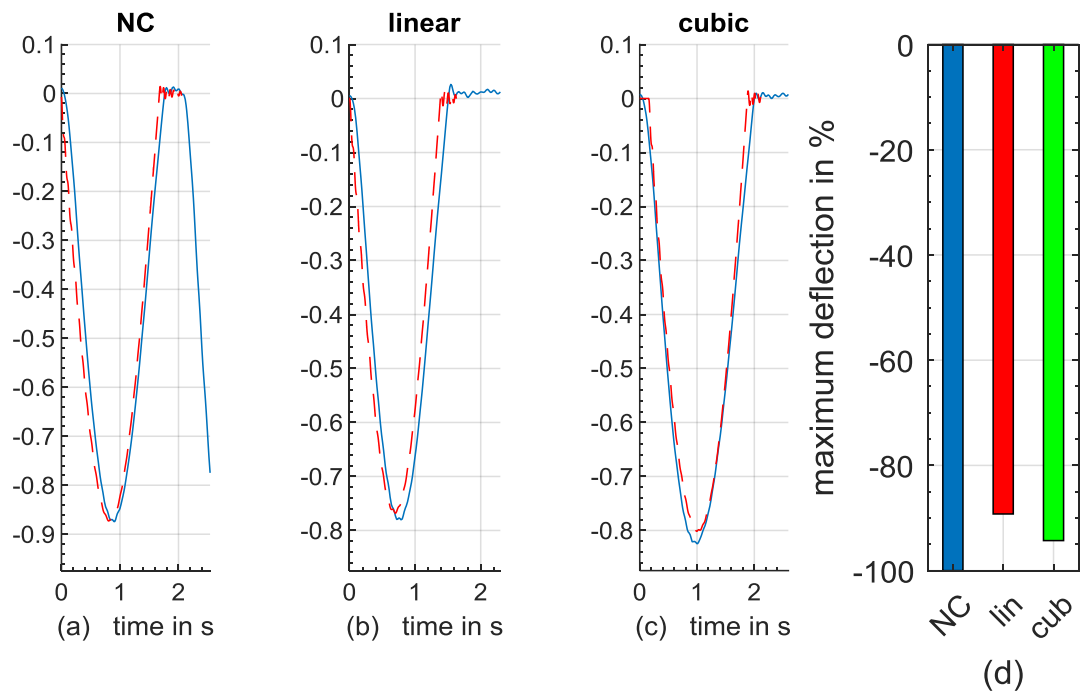


Figure 6.2. Mass $m_1 = 0.261$ kg moving on the structure, comparison of the displacement $w(x_{s2})$ for the experimentally measured data (blue continuous) and the numerically calculated data (red dashed), for the case without control (a), with the liner displacement feedback control (b) and the cubic displacement control (c).

Figure 6.3 shows a different picture for mass $m_4 = 0.509$ kg. At this higher mass the cubic control proves more efficient. The maximum deflection is reduced by approx. 18%, whereas the linear control accomplishes a reduction of the maximum deflection of 10%. The cubic control might not be able to reduce the vibrations after the mass is leaving, as the numerical data indicates. The structure vibrates at approximately 17 Hz. Note that in the experimental data these vibrations are filtered.

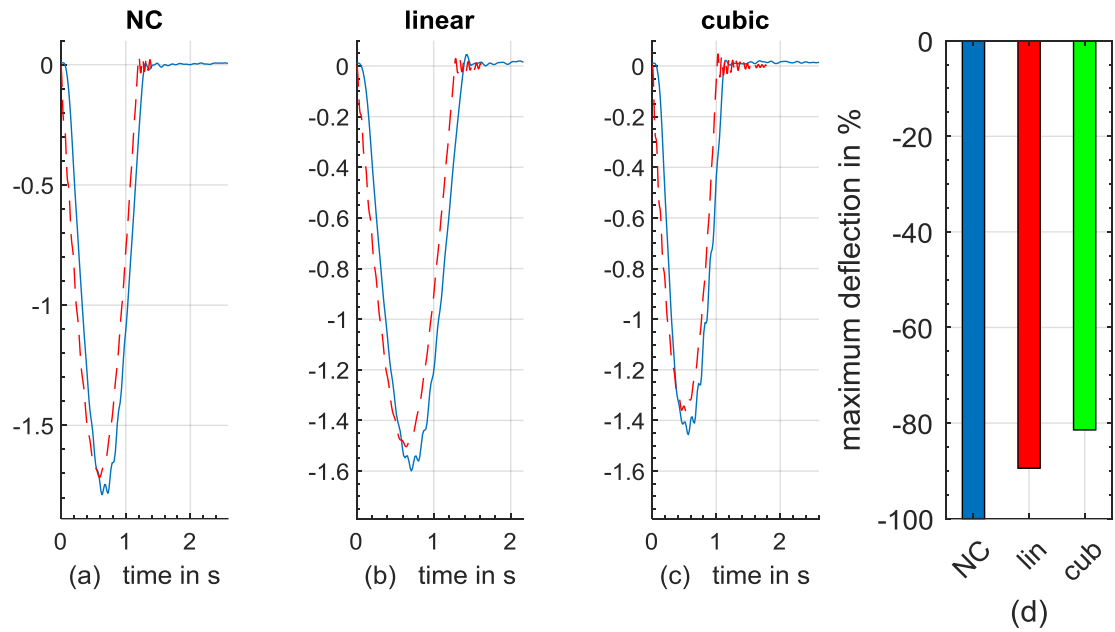


Figure 6.3. Mass $m_4 = 0.509$ kg moving on the structure, comparison of the displacement $w(x_{s2})$ for the experimentally measured data (blue continuous) and the numerically calculated data (red dashed), for the case without control (a), with the linear displacement feedback control (b) and the cubic displacement control (c).

It can be noticed that the structure tends to oscillate for the cubic control with m_4 at low speed $= 0.28 \text{ ms}^{-1}$, see Figure 6.4 right. Comparing the unfiltered displacement responses $w(x_{s1})$ and $w(x_{s3})$ with the filtered response $w(x_{s2})$ one can notice on one hand that the sensor noise is filtered. On the other hand, a delay is added to the system which might be the reason for possible instabilities. Also the digital computer adds delay to the system. The control cannot react fast enough to the vibrations with a frequency of approximately $f = 10$ Hz. As Stancioiu [41] shows, an additional lead compensator can increase the phase margins and stabilize the system. The proportional control decreases the damping of the poles slightly. A proportional derivative control might be more suited as the poles move towards increased damping. Simulations done with the help of the MATLAB SISO tool including the 10th order Butterworth low-pass filter show no improvement by using a PD or lead compensator. The oscillations could be reduced by reducing the cut-off frequency of the low-pass filter to $f_{3dB} = 5$ Hz.

Preumont [42] recommends using an analogue anti-aliasing filter before the analogue to digital converter of the controller to avoid aliasing. This should be considered in future studies. The utilised analogue-to-digital converter (ADC) module NI 9222 does not feature

an anti-aliasing filter. Other ADC modules have an anti-aliasing filter in-build. In contrast to the finite time optimal control the proportional control excited all the modes of the structure with the same proportional gain, which could cause instability as well. A more advanced control approach, like the previously presented finite time optimal control seems necessary.

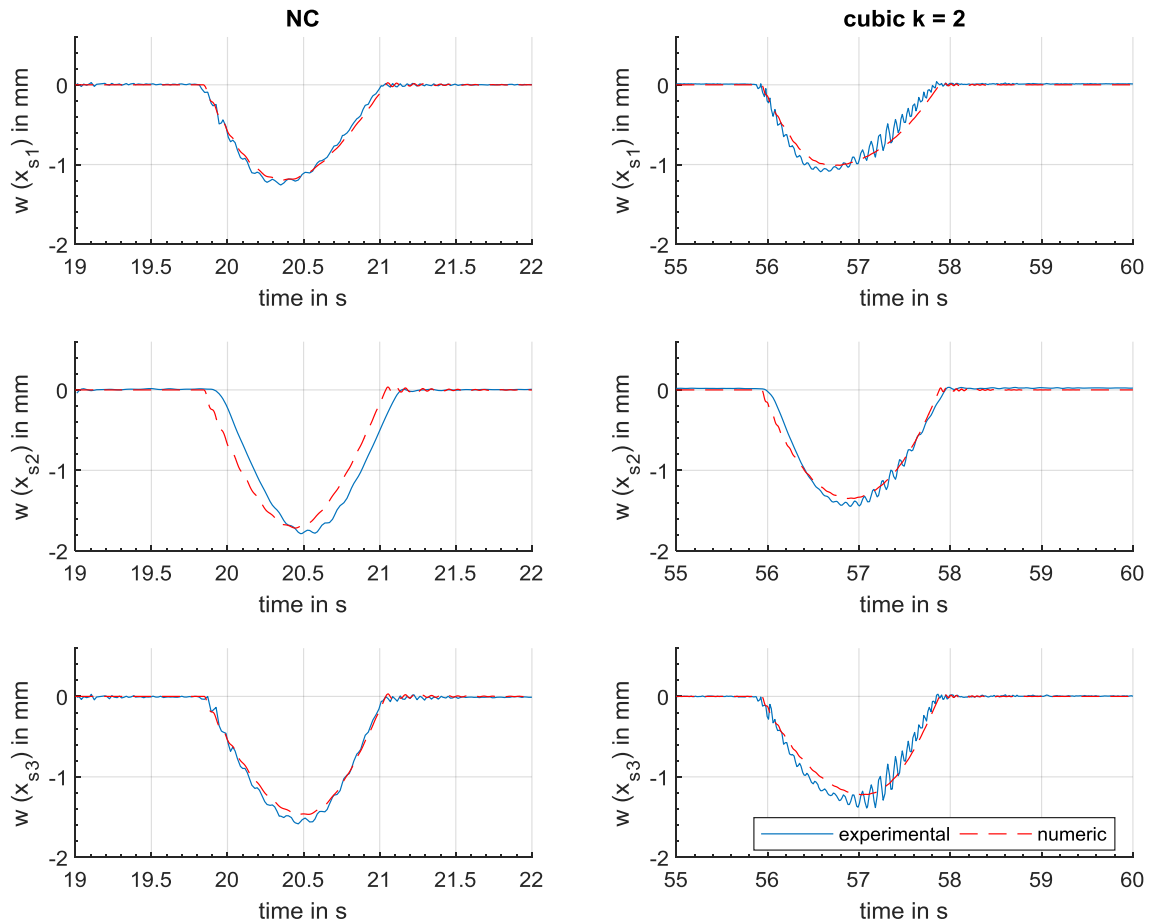


Figure 6.4. Time history of the displacement responses experimental (blue continuous) and numerical (red dashed) $w(x_{s1}) - w(x_{s3})$ comparing the uncontrolled structure with the cubic displacement rule controlled structure (right), mass m_4 , $k = 2$ at $v = 0.28 \text{ ms}^{-1}$.

The saturation limit of $u_{max} \leq 1500\text{V}$ was not reached, see Figure 6.5. Measurements of the input voltage $u(t)$ were taken from the compactRio controller and multiplied by the amplifier gain $g_a = 200$ for the purpose of illustration.

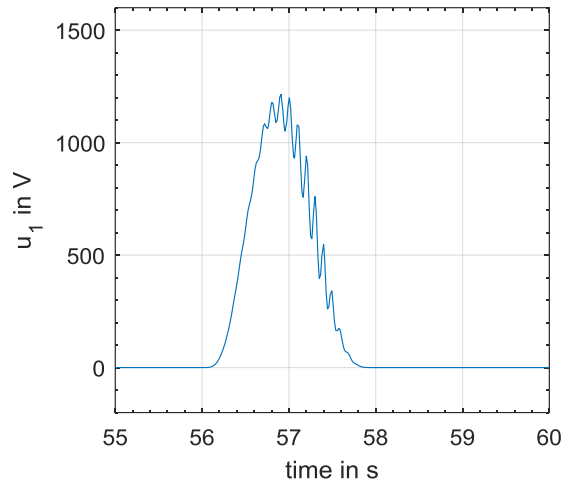


Figure 6.5. Control input $u_1(t)$ for the cubic control with $k = 2$ and m_4 .

Figure 6.6 summarises the relative deflection reduction at sensor location x_{s2} for the different masses $m_1 - m_4$ for the two control approaches and the applied gain $k=2$. The relatively constant reduction with the linear gain from 9% to 11% can be noticed. The cubic control approach constantly increases the relative displacement reduction from 5.5% to 18.5%. As shown in Figure 6.4 the result for m_4 for the cubic control should be viewed with caution as additional oscillations are added.

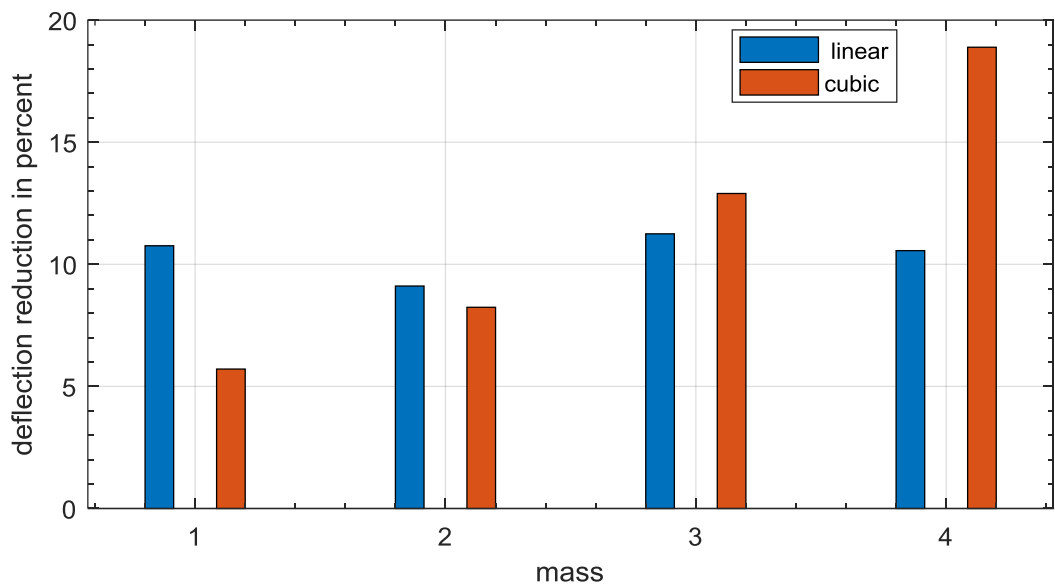


Figure 6.6. Comparison of the reduction of deflection for the linear control (blue) and for the cubic control (red) for masses $m_1 = 0.261$ kg, $m_2 = 0.322$ kg, $m_3 = 0.371$ kg and $m_4 = 0.509$ kg.

It can be noticed that the linear control is more effective for lower masses (m_1 and m_2). Whereas the cubic control is more effective at higher masses (m_3 and m_4). To limit the control effort for small masses and to have a more effective control for heavy masses a simple gain scheduling approach could be implemented, see Figure 6.7. One could think of a gain scheduling approach and use the linear control with $k = 2$ for masses up to $m = 0.345$ kg. The linear gain is then switched to $k = 3$ up to a mass of $m = 0.45$, where the gain is switched again to $k = 3.6$. The mass margins for switching were captured numerically. In this way a more efficient gain scheduling control could be accomplished. Figure 6.7 illustrates this procedure. Future studies could test this approach experimentally.

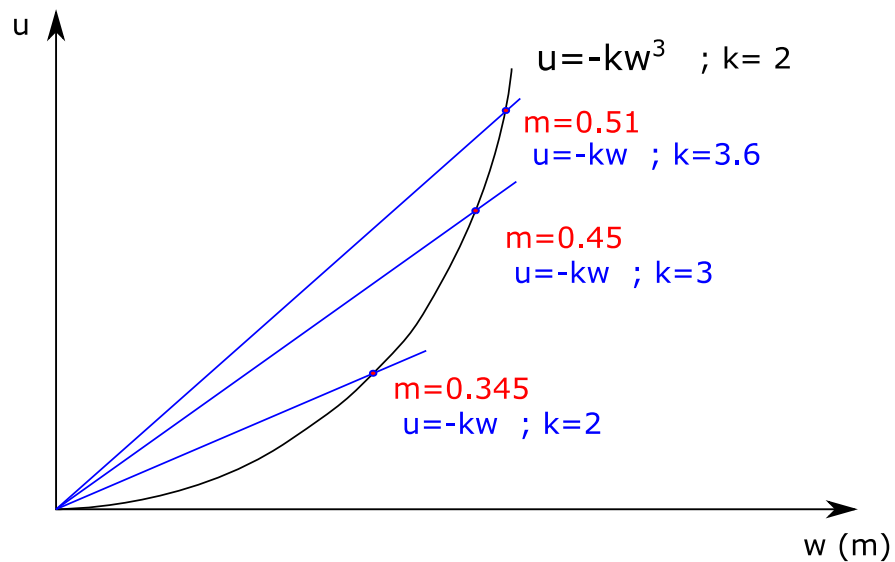


Figure 6.7. Gain scheduling approach for the linear displacement control (blue) and for the cubic displacement control (black).

In the previous section, it was also shown, that a straightforward displacement feedback control is able to reduce the structural maximum deflection of the simply supported beam by about 8 % to 13 %. For mass m_4 the limit to apply this approach was shown. A modal filter could be applied to actuate only the first mode of the structure.

6.2 Two-Span Continuous Beam Controlled by Piezoelectric Actuators

The cubic displacement feedback is implemented for the experimental setup of the two-span beam depicted in section 2.1.3 . The displacement sensors are now collocated to the MFC actuators at $x_{s1} = 0.3$ m and $x_{s3} = 0.9$ m. A third additional sensor measures the displacement at $x_{s2} = 0.45$ m. A low pass filter with $f_{3dB} = 20$ Hz is utilised at x_{s1} and x_{s3} . A constant gain $k = 2$ is applied in equation (6.3) to actuate the two piezoelectric actuators. Figure 6.8 illustrates the time history of the experimentally and numerically obtained displacement data sets $w(x_{s1}) - w(x_{s3})$ for the uncontrolled two-span beam (NC), the linear controlled structure and the by the cubic displacement rule controlled structure. A good match is achieved between the numerically derived and the experimentally derived data.

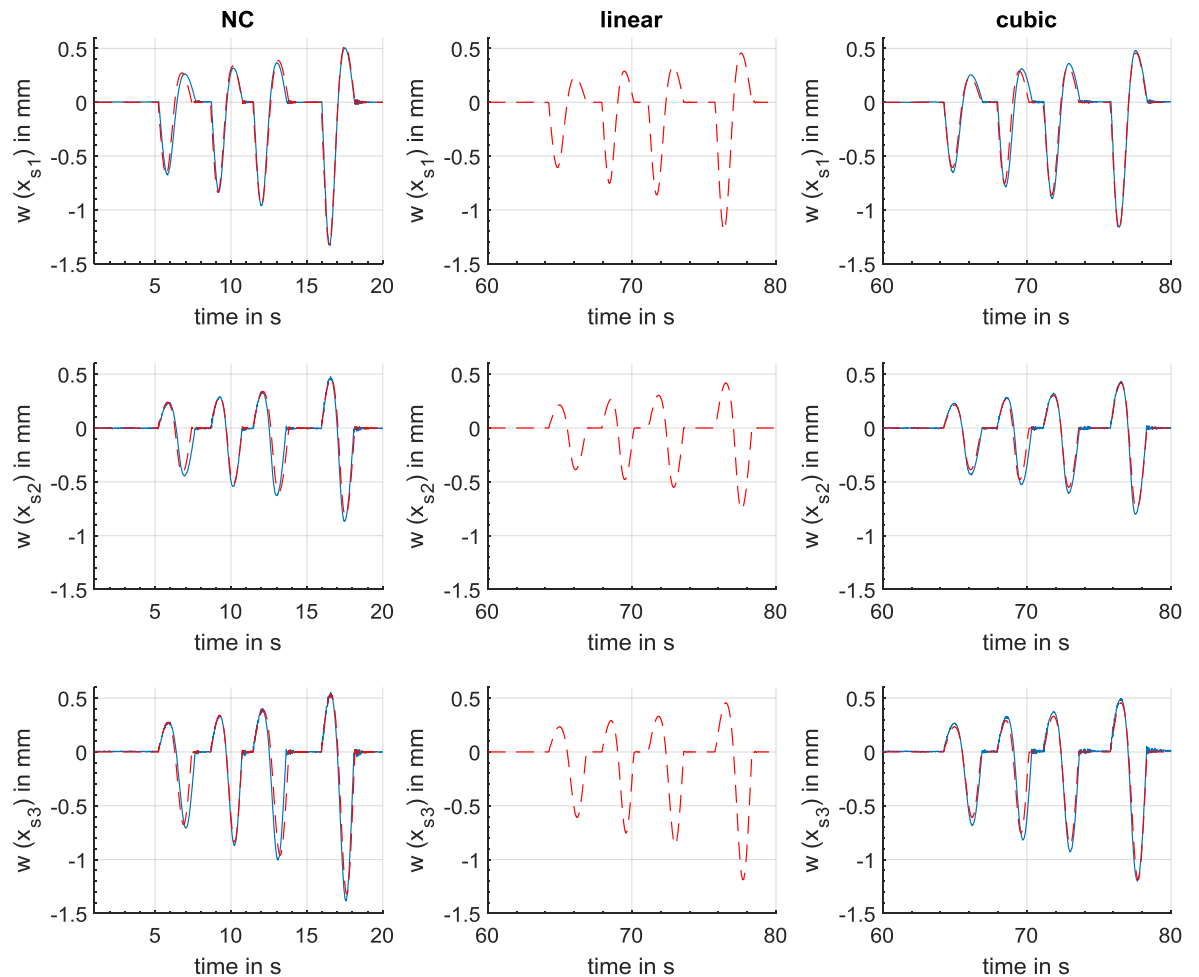


Figure 6.8. Time history of the deflection $w(x_{s1}) - w(x_{s3})$ of the uncontrolled two-span beam (left) and the controlled two-span beam (right), experimentally (blue continuous) and numerically (red dashed).

Table 6.1 illustrates the maximum deflection at $w(x_{s1})$ for the four masses $m_1 - m_4$ applying the different control approaches. Due to the cubic displacement feedback rule the control is more active at higher disturbances. In this way less control effort is needed for lower masses. When $w(x) \geq 1$ mm in equation (6.3), the cubic control results in higher control inputs and lower deflections compared to the linear control, which offers higher control inputs when $w(x) \leq 1$ mm.

For mass m_4 the maximum displacement is reduced by 12.84%. For mass m_1 the maximum displacement is reduced by 3.4%. The linear control reduces the maximum deflection for all masses by approx. 10%.

Table 6.1. Maximum experimental deflection at $w(x_{s1})$ open-loop (NC), cubic feedback, and difference dw between NC and cubic, theoretical linear control for reference.

	NC $w(x_{s1})$ in mm	cubic $w(x_{s1})$ in mm	dw in % $w(x_{s1})$	Linear (th) $w(x_{s1})$ in mm	dw in % $w(x_{s1})$
m_1	-0.676	-0.653	3.40	-0.605	10.51
m_2	-0.833	-0.782	6.12	-0.752	9.72
m_3	-0.959	-0.895	6.67	-0.8607	10.25
m_4	-1.331	-1.160	12.84	-1.196	10.14

Similar results are obtained for the maximum deflection at the second midspan $w(x_{s3})$ depicted in Table 6.2. Due to the higher deflection at the second span, the cubic control is slightly more effective with a relative reduction of the maximum deflection of 13.25% for m_4 compared to 12.84% at x_{s1} . Also, for masses m_2 and m_3 the relative reduction is slightly higher, with 6.5% for m_2 compared to 6.1% at x_{s1} and 8.02% for m_3 compared to 6.67 % at x_{s1} .

The results obtained numerically for the linear control approach show again that the linear control is more efficient (deflection reduction of 10%) for smaller masses. dw for the linear control is related to the theoretical results of the uncontrolled case. In Table 6.1 the theoretical maximum deflection for NC is not listed because it coincides with the experimental results.

Table 6.2. Maximum experimental (ex) and theoretical (th) deflections $w(x_{s3})$ open-loop (NC), cubic feedback and linear control, difference dw (ex) between NC (ex) and cubic (ex), difference dw (th) between NC (th) and linear control (th) for reference.

	NC (ex) $w(x_{s3})$ in mm	NC (th) $w(x_{s3})$ in mm	Cubic (ex) $w(x_{s3})$ in mm	dw (ex) in % $w(x_{s3})$	Linear (th) $w(x_{s3})$ in mm	dw (th) in % $w(x_{s3})$
m_1	-0.701	-0.669	-0.683	2.56	-0.607	9.26
m_2	-0.873	-0.836	-0.816	6.53	-0.755	9.67
m_3	-0.997	-0.959	-0.917	8.02	-0.864	9.91
m_4	-1.383	-1.320	-1.200	13.23	-1.188	10

The positive maximum deflections for NC and the cubic case are listed in Table 6.3. Relative reduction achieved for the cubic control ranges from 4.3% for m_3 to approx. 4.7% for masses m_1 and m_2 to 8.77% for mass m_4 .

Table 6.3. Maximum positive deflection at $w(x_{s3})$ open-loop (NC), cubic feedback, and difference dw

	NC $w(x_{s3})$	cubic $w(x_{s3})$	dw in % $w(x_{s3})$
m_1	0.277	0.264	4.69
m_2	0.338	0.322	4.73
m_3	0.394	0.377	4.31
m_4	0.536	0.489	8.77

Figure 6.9 displays the input voltages u_1 and u_2 for the piezoelectric actuators. The maximum positive control voltage is noticed for mass m_4 moving on the second span with $u_2 = 680$ V. The minimum control voltage is noticed for m_1 moving on the first span with $u_1 = 111$ V. The saturation limits of the actuators are defined as $-500 \text{ V} \leq u \leq 1500 \text{ V}$. It

becomes clear that a more efficient control could be achieved, when the control saturation limits can be taken into account in the control approach. The model predictive control approach, which takes into account the saturation limits will be presented in the next chapter.

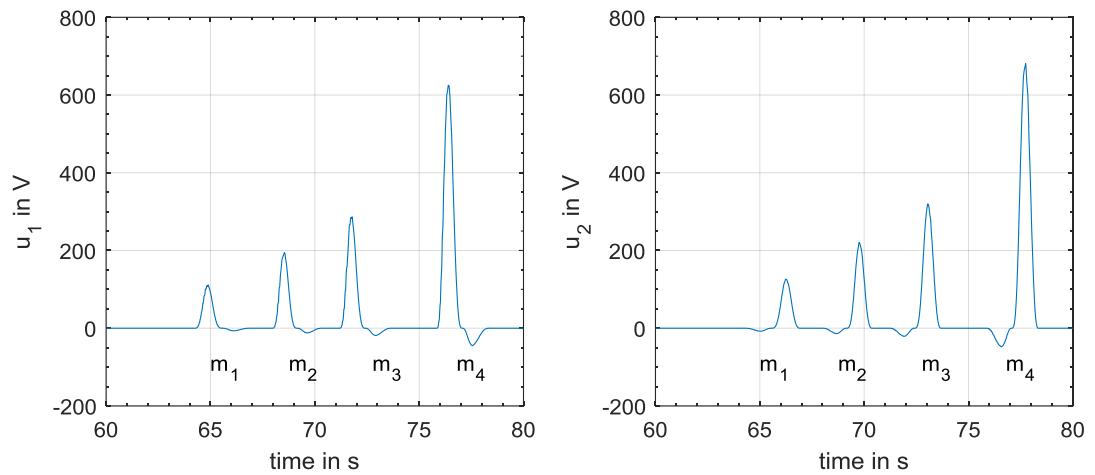


Figure 6.9. Experimental input values u_1 and u_2 for the piezoelectric actuators with the cubic displacement feedback control.

An experiment with a higher gain $k=3$ caused the system to become unstable. The displacement response at sensor location $w(x_{s1})$ is displayed in Figure 6.10. It can be noticed, that the control is able to control mass m_1 moving along the beam, but becomes unstable for mass $m_2=0.322$ kg and higher masses.

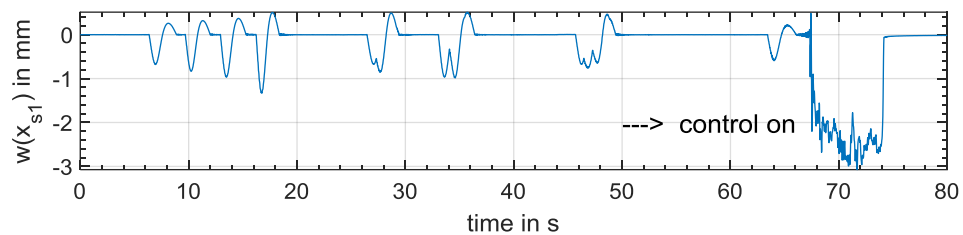


Figure 6.10. Time history of the deflection data $w(x_{s1})$ cubic displacement feedback control applied to the two span beam with $k=3$

Nevertheless, the simple way to implement the displacement feedback control makes it easy to control multiple masses moving on the beam with random speeds, Figure 6.11. The

maximal negative deflection is reduced by 10.5% at x_{s3} . The uncontrolled case was simulated numerically only, as it is difficult to launch the balls manually synchronously to achieve similar experimental results.

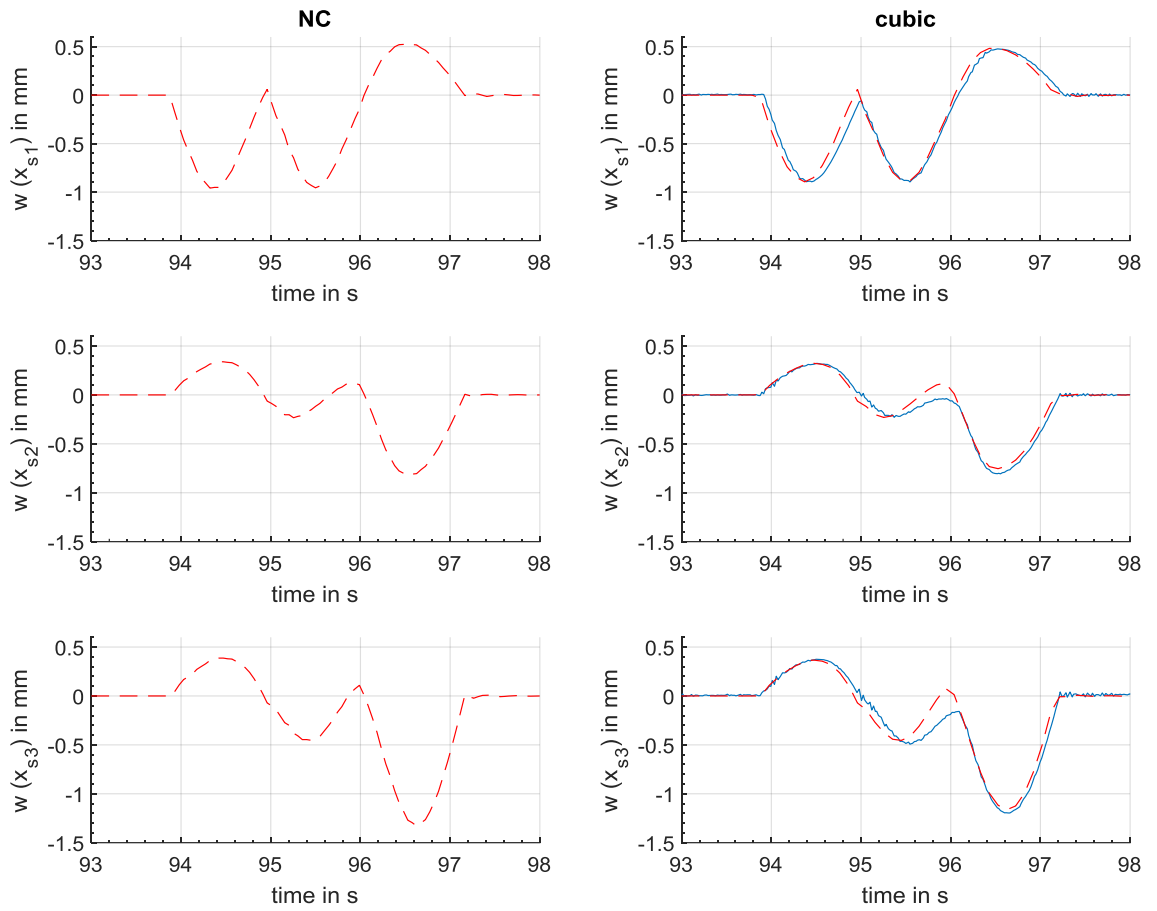


Figure 6.11. Deflection responses $w(x_{s1}) - w(x_{s3})$ of the uncontrolled structure (left) and the cubically controlled structure (right), numerically (red dashed) and experimentally (blue continuous) when two masses $m_3 = 0.371$ kg and $m_4 = 0.509$ kg travel on the beam.

7 Model Predictive Control for Moving Load Structures

The previous examples showed that with simple displacement feedback control the maximum input voltages of $-500 \text{ V} \leq U \leq 1500 \text{ V}$ cannot be reached without causing the system to become unstable. An control approach to include the saturation limits is the model predictive control. The main idea is to include future states of the system into the optimization procedure.

7.1 The Control Algorithm

For the receding horizon model predictive control approach an augmented discrete state space model is used [79]:

$$\overbrace{\begin{bmatrix} \Delta \mathbf{x}_m(k+1) \\ \mathbf{y}(k+1) \end{bmatrix}}^{\mathbf{x}(k+1)} = \overbrace{\begin{bmatrix} \mathbf{A}_m & \mathbf{0}_m^T \\ \mathbf{C}_m \mathbf{A}_m & \mathbf{I} \end{bmatrix}}^{\mathbf{A}} \overbrace{\begin{bmatrix} \Delta \mathbf{x}_m(k) \\ \mathbf{y}(k) \end{bmatrix}}^{\mathbf{x}(k)} + \overbrace{\begin{bmatrix} \mathbf{B}_m \\ \mathbf{C}_m \mathbf{B}_m \end{bmatrix}}^{\mathbf{B}} \Delta \mathbf{u}(k) \quad (7.1)$$

$$\mathbf{y}(k) = \overbrace{\begin{bmatrix} \mathbf{0}_m & (1 \dots 1) \end{bmatrix}}^{\mathbf{c}} \begin{bmatrix} \Delta \mathbf{x}_m(k) \\ \mathbf{y}(k) \end{bmatrix}$$

Where $\Delta \mathbf{x}_m$ is the difference of the state variables.

$$\begin{aligned} \Delta \mathbf{x}_m(k+1) &= \mathbf{x}_m(k+1) - \mathbf{x}_m(k); \quad \Delta \mathbf{x}_m(k) \\ &= \mathbf{x}_m(k) - \mathbf{x}_m(k-1) \end{aligned} \quad (7.2)$$

The future control trajectory vector $\Delta\mathbf{U}$ is donated by:

$$\Delta\mathbf{U} = [\Delta\mathbf{u}(k_i), \Delta\mathbf{u}(k_i + 1), \dots, \Delta\mathbf{u}(k_i + N_c - 1)]^T \quad (7.3)$$

Where N_c is called the control horizon, defining the number of future trajectory points. The prediction horizon N_p defines the number of future states $\mathbf{x}(k_i + m|k_i)$ calculated with the given state vector $\mathbf{x}(k_i)$ and the length of the optimization window. The future output variables $\mathbf{Y} = [\mathbf{y}(k_i + 1|k_i), \mathbf{y}(k_i + 2|k_i), \dots, \mathbf{y}(k_i + m|k_i), \dots, \mathbf{y}(k_i + N_p|k_i)]^T$ get calculated by

$$\mathbf{Y} = \mathbf{F}\mathbf{x}(k_i) + \Phi\Delta\mathbf{U} \quad (7.4)$$

where

$$\mathbf{F} = \begin{bmatrix} \mathbf{CA} \\ \mathbf{CA}^2 \\ \mathbf{CA}^3 \\ \vdots \\ \mathbf{CA}^{N_p} \end{bmatrix}; \quad \Phi = \begin{bmatrix} \mathbf{CB} & \mathbf{0} & \mathbf{0} & \dots & \mathbf{0} \\ \mathbf{CAB} & \mathbf{CB} & \mathbf{0} & \dots & \mathbf{0} \\ \mathbf{CA}^2\mathbf{B} & \mathbf{CAB} & \mathbf{CB} & \dots & \mathbf{0} \\ \vdots & \vdots & \vdots & \ddots & \vdots \\ \mathbf{CA}^{N_p-1}\mathbf{B} & \mathbf{CA}^{N_p-2}\mathbf{B} & \mathbf{CA}^{N_p-3}\mathbf{B} & \dots & \mathbf{CA}^{N_p-N_c}\mathbf{B} \end{bmatrix} \quad (7.5)$$

The cost function J that reflect the control objective, which is to minimize the output variables and the control input and is defined as

$$J = \mathbf{Y}^T\mathbf{Y} + \Delta\mathbf{U}^T\bar{\mathbf{R}}\Delta\mathbf{U} \quad (7.6)$$

Where $\bar{\mathbf{R}} = r_w\mathbf{I}_{N_c \times N_c}$ and r_w is utilised as a tuning parameter for the desired closed-loop performance. Inserting equation (7.4) in equation (7.6) leads to

$$J = (\mathbf{F}\mathbf{x}(k_i))^T (\mathbf{F}\mathbf{x}(k_i)) + 2\Delta\mathbf{U}^T\Phi^T\mathbf{F}\mathbf{x}(k_i) + \Delta\mathbf{U}^T(\Phi^T\Phi + \bar{\mathbf{R}})\Delta\mathbf{U} \quad (7.7)$$

Minimizing J by setting the first derivative to zero the new control vector $\Delta\mathbf{U}$ can be found:

$$\frac{\partial J}{\partial \Delta \mathbf{U}} = 2\mathbf{\Phi}^T \mathbf{F} \mathbf{x}(k_i) + 2(\mathbf{\Phi}^T \mathbf{\Phi} + \bar{\mathbf{R}}) \Delta \mathbf{U} = \mathbf{0} \quad (7.8)$$

$$\Delta \mathbf{U}(k_i) = (\mathbf{\Phi}^T \mathbf{\Phi} + \bar{\mathbf{R}})^{-1} \mathbf{\Phi}^T (-\mathbf{F} \mathbf{x}(k_i)), \quad (7.9)$$

Considering the time variation of the system, matrixes $\mathbf{F}(k_i)$ and $\mathbf{\Phi}(k_i)$ change at every time step k_i due to time variation of the system matrixes $\mathbf{A}(k_i)$, $\mathbf{B}(k_i)$ and $\mathbf{C}(k_i)$. The change of the control force is

$$\Delta \mathbf{U}(k_i) = (\mathbf{\Phi}(k_i)^T \mathbf{\Phi}(k_i) + \bar{\mathbf{R}})^{-1} \mathbf{\Phi}(k_i)^T (-\mathbf{F}(k_i) \mathbf{x}(k_i)), \quad (7.10)$$

7.2 Discrete Time Model Predictive Control with Constraints.

For the use of the piezoelectric actuator the input voltage has to be constrained, e.g. to $-2.5 \text{ V} \leq u(k) \leq 7.5 \text{ V}$. These are the minimum and maximum input voltages for the amplifier for MFC P1 actuators [101]. These constraints have to be considered in the optimization otherwise the closed loop performance could drastically deteriorate [79]. MPC control approach has an explicit constraint handling feature [87,109]. Constraints can be applied on the elements of $\Delta \mathbf{U}$ of MIMO systems. The constraints are expressed as

$$\mathbf{M} \mathbf{x} \leq \boldsymbol{\gamma} \quad (7.11)$$

The general objective function of a constraint problem is described as

$$J = \frac{1}{2} \mathbf{x}^T \mathbf{E} \mathbf{x} + \mathbf{x}^T \mathbf{F} \quad (7.12)$$

This is a quadratic programming problem. To be consistent with the literature the decision variable is defined by \mathbf{x} . To minimize the objective function subjected to equality constraints the Lagrange expression is introduced.

$$J = \frac{1}{2} \mathbf{x}^T \mathbf{E} \mathbf{x} + \mathbf{x}^T \mathbf{F} + \boldsymbol{\lambda}^T (\mathbf{M} \mathbf{x} - \boldsymbol{\gamma}) \quad (7.13)$$

The value of equation (7.13) is the same as of equation (7.12) if the constraint $\mathbf{M} \mathbf{x} = \boldsymbol{\gamma}$ is satisfied. Taking the first derivatives with respect to \mathbf{x} and $\boldsymbol{\lambda}$ and equate these to zero

$$\frac{\partial J}{\partial \mathbf{x}} = \mathbf{E} \mathbf{x} + \mathbf{F} + \mathbf{M}^T \boldsymbol{\lambda} = 0 \quad (7.14)$$

$$\frac{\partial J}{\partial \boldsymbol{\lambda}} = \mathbf{M} \mathbf{x} - \boldsymbol{\lambda} = 0 \quad (7.15)$$

one can calculate the solutions for \mathbf{x} and $\boldsymbol{\lambda}$:

$$\mathbf{x} = -\mathbf{E}^{-1} (\mathbf{M}^T \boldsymbol{\lambda} + \mathbf{F}) \quad (7.16)$$

$$\boldsymbol{\lambda} = -(\mathbf{M} \mathbf{E}^{-1} \mathbf{M}^T)^{-1} (\boldsymbol{\gamma} + \mathbf{M} \mathbf{E}^{-1} \mathbf{F}) \quad (7.17)$$

The number of inequality constraints in equation (7.11) could be larger than the number of decision variables. To obtain a feasible solution, by converging of the quadratic programming algorithm, the number of inequality constraints has to be less than or equal to the number of decision variables. An i th inequality is said to be active if $M_i x = \gamma_i$ and inactive if $M_i x < \gamma_i$. For an active constraint applies $\lambda_i \geq 0$. The idea of active set methods is to define a set of constraints that are active at each iteration step which is called the working set [79]. Solutions based on the decision variable (also called primal variable) belong to the primal method and are characterised by a high computational effort if the number of constraints is large. In the dual method, the solution is based on the Lagrange multiplier (called dual variable). It can be used to find constraints that are not active, which are then eliminated from the solution. This method leads to more simple programming procedure, the Hildreth's quadratic programming. Assuming there is an \mathbf{x} such that $\mathbf{M} \mathbf{x} < \boldsymbol{\gamma}$ the primal problem is equivalent to

$$\max_{\lambda \geq 0} \min_{\mathbf{x}} \left[\frac{1}{2} \mathbf{x}^T \mathbf{E} \mathbf{x} + \mathbf{x}^T \mathbf{F} + \boldsymbol{\lambda}^T (\mathbf{M} \mathbf{x} - \boldsymbol{\gamma}) \right] \quad (7.18)$$

The minimization over \mathbf{x} is unconstrained and is attained by equation (7.16), substituting this into (7.18) leads to the dual problem

$$\max_{\lambda \geq 0} -\frac{1}{2} \boldsymbol{\lambda}^T \mathbf{H} \boldsymbol{\lambda} + \boldsymbol{\lambda}^T \mathbf{K} - \frac{1}{2} \mathbf{F}^T \mathbf{E}^{-1} \mathbf{F} \quad (7.19)$$

Where the matrices \mathbf{H} and \mathbf{F} are given by

$$\mathbf{H} = \mathbf{M} \mathbf{E}^{-1} \mathbf{M}^T \quad (7.20)$$

$$\mathbf{K} = \boldsymbol{\gamma} + \mathbf{M} \mathbf{E}^{-1} \mathbf{F} \quad (7.21)$$

The Hildreth's quadratic programming procedure uses the dual method. Having a vector $\boldsymbol{\lambda} > 0$ the algorithm takes an element λ_i and minimizes the objective function. If therefore $\lambda_i < 0$ is required, $\lambda_i = 0$. Then the next component λ_{i+1} is considered. If one iteration is considered to be one cycle throughout the elements of the vector $\boldsymbol{\lambda}^m$ to $\boldsymbol{\lambda}^{m+1}$ the method can be explicitly expressed as [79]:

$$\lambda_i^{m+1} = \max(0, w_i^{m+1}) \quad (7.22)$$

with

$$w_i^{m+1} = -\frac{1}{h_{ii}} \left[k_i + \sum_{j=1}^{i-1} h_{ij} \lambda_j^{m+1} + \sum_{j=i+1}^n h_{ij} \lambda_j^m \right] \quad (7.23)$$

Where h_{ij} is the ij th element in the matrix \mathbf{H} (equation (7.20)) and k_i is the i th element in the vector \mathbf{K} (equation (7.21)). The converged $\boldsymbol{\lambda}^*$ vector contains either zero or positive values of the Lagrange multiplier. The decision variable can be calculated by equation (7.16).

From equation (7.9) the objective function for the MPC can be obtained as

$$J = 2\Delta\mathbf{U}^T\boldsymbol{\Phi}^T\mathbf{F}\mathbf{x}(k_i) + \Delta\mathbf{U}^T(\boldsymbol{\Phi}^T\boldsymbol{\Phi} + \bar{\mathbf{R}})\Delta\mathbf{U} \quad (7.24)$$

wherein the matrices \mathbf{E} and \mathbf{F} in equation (7.13) are apparent as

$$\mathbf{E} = 2(\boldsymbol{\Phi}^T\boldsymbol{\Phi} + \bar{\mathbf{R}}) \quad (7.25)$$

$$\mathbf{F} = 2\boldsymbol{\Phi}^T\mathbf{F}\mathbf{x}(k_i) \quad (7.26)$$

7.3 Numerical Examples of the Model Predictive Control for the Beam Structures Controlled by Piezoelectric Actuators

The previously presented MPC approach will be applied to the simply supported beam structure and to the two-span continuous beam structure validated in section.2.4.2 The augmented system presented in equation (5.8) is applied with $t = 0$. The N_c inequality equations for the one-span beam structure are defined as

$$\begin{aligned} u_{min}(k) &\leq u(k|k) \leq u_{max}(k) \\ u_{min}(k+1) &\leq u(k+1|k) \leq u_{max}(k+1) \\ &\vdots \\ u_{min}(k+N_c-1) &\leq u(k+N_c-1|k) \leq u_{max}(k+N_c-1) \end{aligned} \quad (7.27)$$

The inequality equations can be written in matrices as in relation to the decision variable $\Delta \mathbf{U}(k)$ as [79]:

$$\begin{bmatrix} 1 & 0 & 0 & \dots & 0 \\ 1 & 1 & 0 & \dots & 0 \\ \vdots & \vdots & \vdots & \ddots & \vdots \\ 1 & 1 & 1 & \dots & 1 \\ -1 & 0 & 0 & \dots & 0 \\ -1 & -1 & 0 & \dots & 0 \\ \vdots & \vdots & \vdots & \ddots & \vdots \\ -1 & -1 & -1 & \dots & -1 \end{bmatrix} \begin{bmatrix} \Delta u(k|k) \\ \Delta u(k+1|k) \\ \vdots \\ \Delta u(k+N_c|k) \end{bmatrix} \leq \begin{bmatrix} u_{max}(k) - u(k-1) \\ u_{max}(k+1) - u(k-1) \\ \vdots \\ u_{max}(k+N_c-1) - u(k-1) \\ -u_{min}(k) + u(k-1) \\ -u_{min}(k+1) + u(k-1) \\ \vdots \\ -u_{min}(k+N_c-1) + u(k-1) \end{bmatrix} \quad (7.28)$$

The following relationships between $\Delta u(k)$ and $u(k)$ are used herein

$$u(k|k) = \Delta u(k|k) + u(k|k-1)$$

$$\begin{aligned} u(k+1|k) &= \Delta u(k+1|k) + u(k|k) = \Delta u(k+1|k) + [\Delta u(k|k) + u(k|k-1)] \\ &\vdots \end{aligned} \quad (7.29)$$

$$\begin{aligned} u(k+N_c-1|k) &= \Delta u(k+N_c-1|k) + \Delta u(k+N_c-2|k) + \dots \\ &\quad + \Delta u(k+1|k) + \Delta u(k|k) + u(k-1) \end{aligned}$$

Equation (7.28) can be written in a compact form as

$$\mathbf{M}_{2aN_c \times N_c} \Delta \mathbf{U}_{2aN_i \times 1} \leq \mathbf{Y}_{2N_c \times 1} \quad (7.30)$$

where \mathbf{M} is the coefficient matrix and \mathbf{y} is the solution vector. Herein the multi-input case is considered, where a is the number of inputs. $\Delta \mathbf{u}(k|k)$, \mathbf{u} , \mathbf{u}_{max} , \mathbf{u}_{min} become vectors of $a \times 1$ dimension. Further restriction could be placed on the rate of control input change Δu , which could reduce unwanted oscillations, if Δu is too large.

7.3.1 Numerical Experiment on the Simply Supported Beam

The input voltage, which is fed into the amplifier, is constrained as $-2.5 \text{ V} \leq u \leq 7.5 \text{ V}$. A mass of $m = 0.509 \text{ kg}$ travels on the simply supported beam with a travelling speed of 1 ms^{-1} . The sampling time is $t_s = 0.01 \text{ s}$. The control weighting factor is defined as $r_w = 1 \times 10^{-11}$. The parameter r_w has a major influence on the control result of this study. It defines the strength of the control action. If $r_w = 0$ in the cost function (7.6), the optimization would not pay any attention on how large ΔU becomes and solely make the error $\mathbf{Y}^T \mathbf{Y}$ as small as possible [79]. For the control horizon and for the optimization horizon, values of $N_c = 4$ and $N_p = 6$ are chosen respectively. The response does not improve for higher N_p and N_c , but the computational load increases. With too short prediction and control horizons the predictive control system is not necessarily stable [79]. The calculations of \mathbf{F} and Φ are accomplished before the actual control iterations for the time-invariant structure. For this case there was no advantage in deflection reduction noticed when $\mathbf{F}(k)$ and $\Phi(k)$ are updated at every iteration step k . The sensor is located in the middle of the structure at $x_s = 0.3 \text{ m}$. It is assumed that the states of the system are available. No observer is implemented. The Hildreth's quadratic programming procedure described in equation (7.22) to equation (7.23) is applied.

Figure 7.1 (left) illustrates the deflection response for the constraint MPC control (red dashed) and compares it with the uncontrolled structure (blue continuous) when the mass is traversing it. The maximum deflection is reduced by 22%. No additional vibrations are added as it was the case for the experimental data obtained by the cubic feedback control (see Figure 6.4). But it should be noted that these additional vibrations were due to the experimental implementation, which is open for future studies for this MPC control approach. Also, the free vibration after the mass has left, is reduced successfully. With the chosen r_w close to 0 the control $U(t)$, Figure 7.1 (right), is able to react to the change of values in $w(x_s)$ with large ΔU values. The constraint maximum voltage of 7.5 V is reached after 0.04 s . The control is able to supply its maximum control action after a very short time.

In contrast the deflection response $w(x_s)$ and the control voltage $U(t)$ of an example with an altered larger value of $r_w = 1 \times 10^{-6}$ is illustrated in **Figure 7.2**. Herein the values of ΔU are smaller. The maximum voltage is reached after 0.32 s and the control is not able to counteract the free vibration after the mass is leaving the beam.

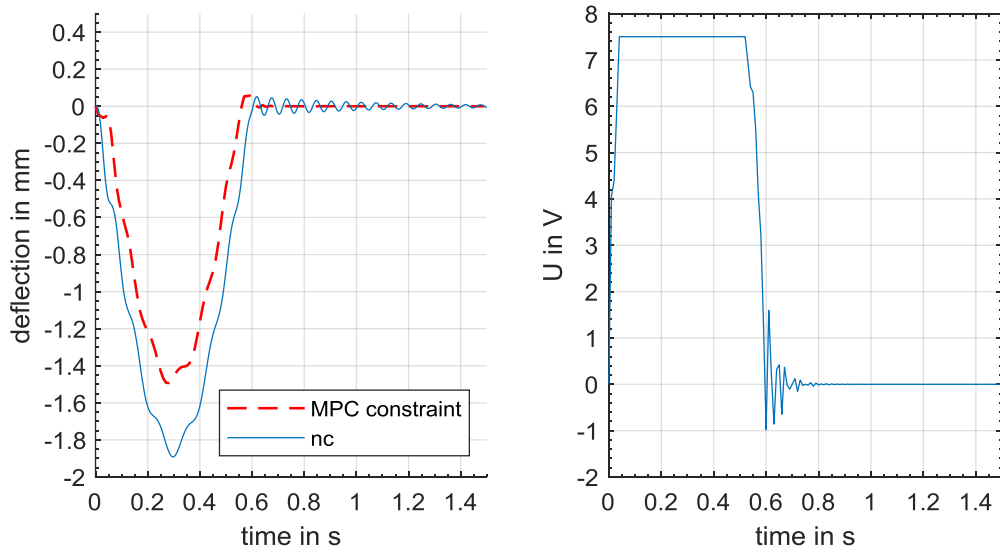


Figure 7.1. Time history of the deflection response $w(0.3\text{ m})$ of the beam structure with a mass of $m = 0.509\text{ kg}$ travelling with a speed of $v = 1\text{ m/s}$, $r_w = 1 \times 10^{-11}$, $N_p = 6$, $N_c = 4$,

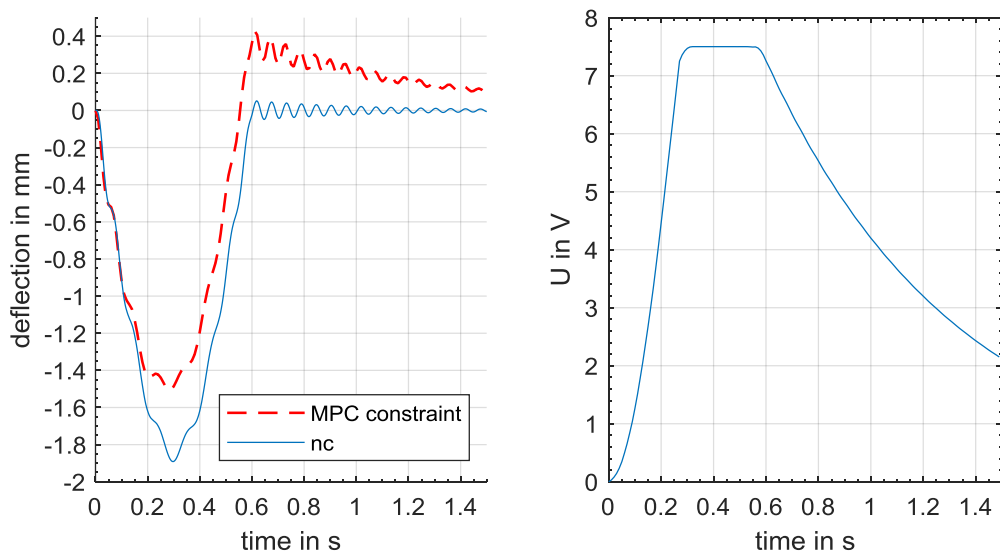


Figure 7.2. Time history of the deflection response $w(0.3\text{ m})$ (left) and of the control Voltage (right) of the MPC controlled simply supported beam, $N_p = 6$, $N_c = 4$, $r_w = 1 \times 10^{-6}$

Figure 7.3 (left) illustrates the deflection response $w(x_s = 0.3\text{ m})$ for the case when $N_c = 1$, $N_p = 6$ and $r_w = 1 \times 10^{-11}$. Compared to Figure 7.1 one can notice higher vibration during the traveling time. The control cannot react to the slight peak at 0.06 s. Another peak can be

noticed at 0.58 s. As it was stated before N_p and N_c should not be chosen too small to guarantee stability and control performance.

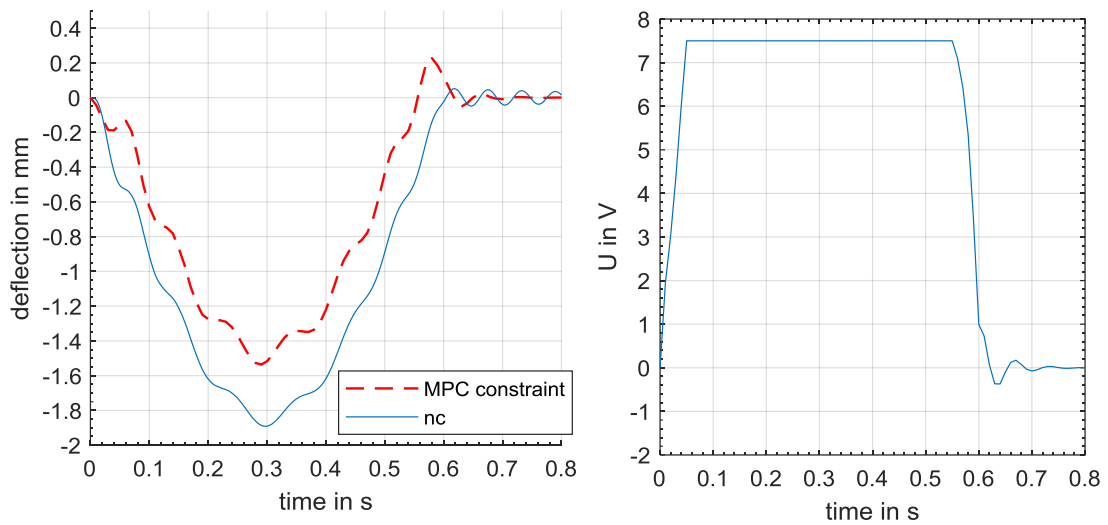


Figure 7.3. Time history of the deflection response w (0.3 m) (left) and of the control Voltage (right) of the MPC controlled simplysupported beam, $N_p = 6$, $N_c = 1$, $r_w = 1 \times 10^{-11}$

Figure 7.4 illustrates the runtime of each iteration step over the travelling time for the two previously presented cases, where the parameter N_c is altered. It can be noticed that when the constraint conditions are met at 0.04 s the runtime increases from 0.5 ms to 13.5 ms for the case with $N_p = 6$, $N_c = 4$. For the case with $N_c = 1$ this peak of the runtime is at 7 ms. Reducing of the control horizon N_c reduced the overall runtime. The runtime is measured between the calculation of ΔU (see equation (7.10)) and the Hildreth quadratic programming (see equation (7.23)) The simulation was accomplished on a computer with an Intel Core i5-3320M Processor with 16 GB Ram. The runtime is below the targeted 10 ms. It is likely that this runtime could not be reached with the CompactRio cRIO-9022 microcontroller, which has a 533 MHz CPU and 256 MB DRAM. If $\mathbf{F}(k)$ and $\Phi(k)$ are time-varying the runtime at 0.04 s increases to 13 ms.

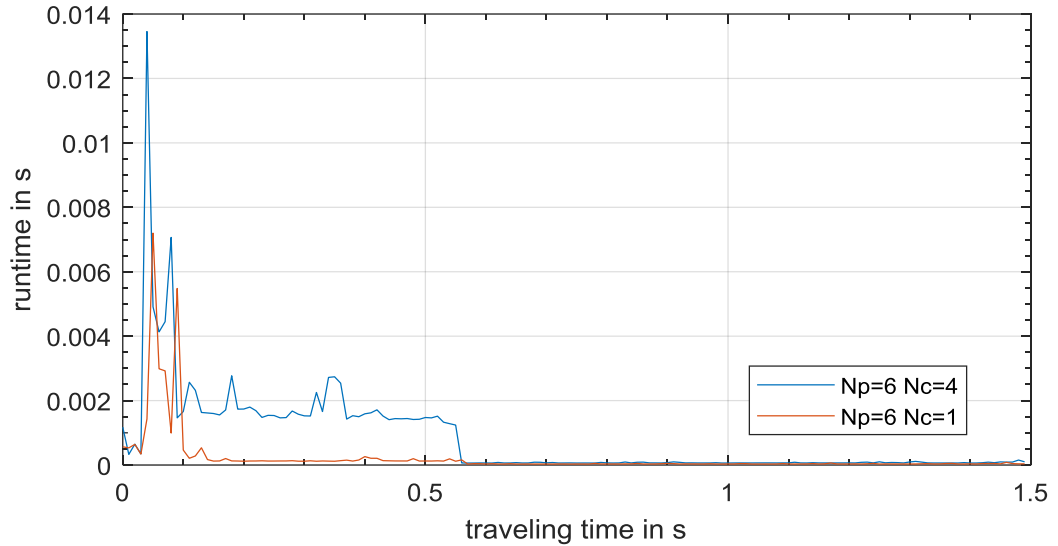


Figure 7.4. Runtime during the control loop over the travelling time.

7.3.2 Numerical Experiment on the Two-Span Continuous Beam Structure

In the following example the MIMO case of the two-span continuous beam structure is considered with mass $m = 0.509$ kg travelling on it. The structure was previously presented in section 2.1.3. Two MFC 8557 P1 actuators are placed in the middle of the test structure with a high $h = 2.83$ mm and a correction factor of $c = 0.39$. The sensors are located in the middle of each span at $x_{s1} = 0.3$ m and at $x_{s2} = 0.9$ m. The input voltages are constrained by $-2.5 \text{ V} \leq \mathbf{u} \leq 7.5 \text{ V}$. Again these are the allowed input voltages for the power amplifier. The MPC parameters are chosen to be $N_c = 3$, $N_p = 4$ and $t_s = 0.01$ s. Eight modes are used for the MPC control. Figure 7.5 depicts the displacement responses of the continuous two-span beam at its two mid-point locations $w(x_{s1})$ and $w(x_{s2})$. After 0.08s the saturation limit u_{max} of the first actuator is reached. u_{min} of the second actuator is reached after 0.09 s. See Figure 7.6, where the values of $\mathbf{u}(k)$ are illustrated. Once the mass moves onto the second span the control actions of u_1 and u_2 switch. The maximum deflection at $w(x_{s1})$ is reduced by 29% for the first half of travelling time and by 64% for the second half of travelling time. At the second mid-span location $w(x_{s2})$ the maximum deflection is reduced by 46% during the first half of travelling time and by 19% during the second half of travelling time.

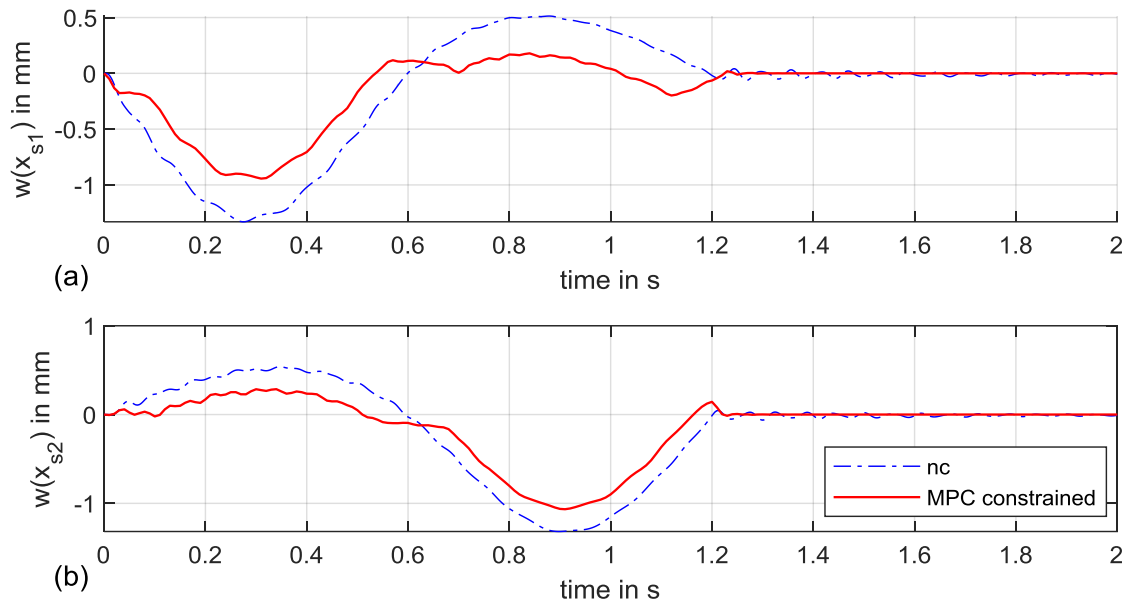


Figure 7.5. Time history the beam's deflection at the first mid-span location (a) and at the second mid-span (b) of the uncontrolled structure (blue-dashed) and of the MPC constrained controlled structure (red continuous).

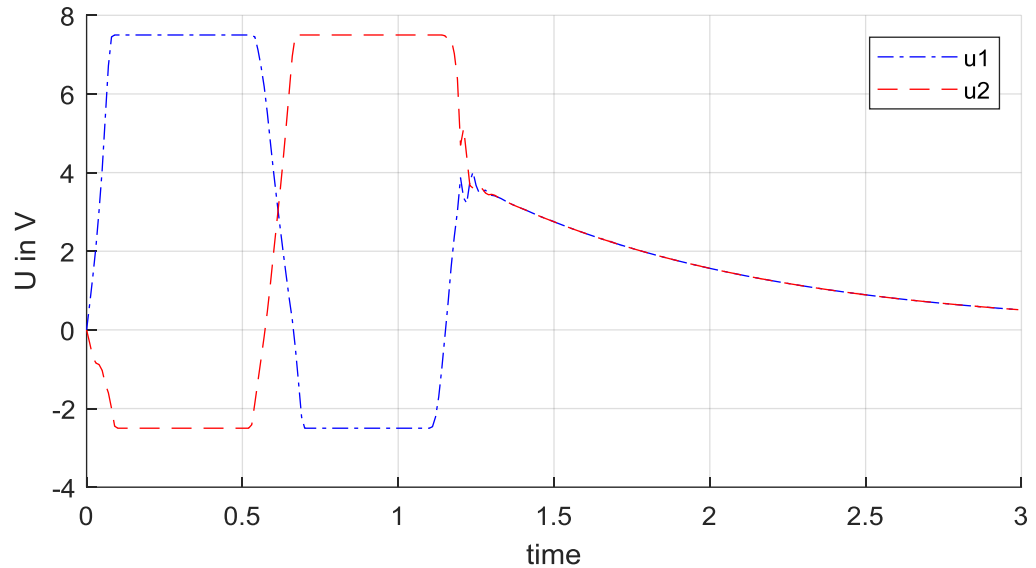


Figure 7.6. Time history of the control input variables u_1 and u_2 .

If the control and prediction horizon are chosen to be larger with $N_c=4$ and $N_p=6$ the vibrations in the structure can be reduced, see Figure 7.7. The reduction of the maximum deflection is with 54% slightly lower at the second half of travelling at $w(x_{s1})$.

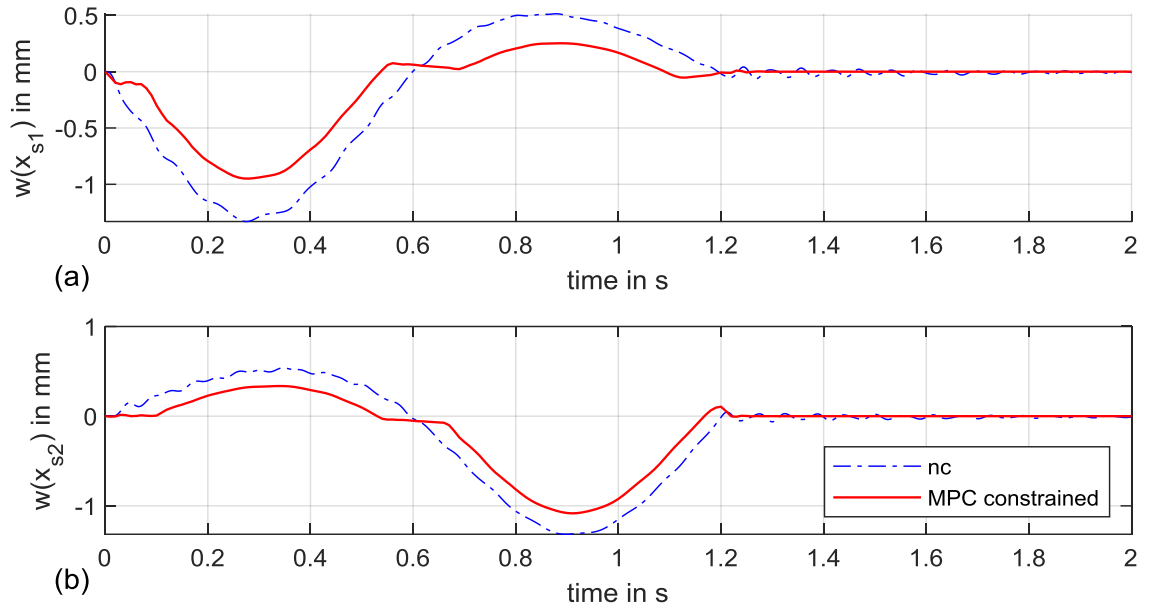


Figure 7.7. Deflection responses $w(x_{s1})$ and $w(x_{s2})$ for MPC control with $N_c = 4$ and $N_p = 6$.

With the number of modes used for the control reduced to three, $N_c = 1$ and $N_p = 2$ it is tried to reduce the runtime. These are the minimal parameters needed to have an effective control. The maximum runtime reduces from 21 ms to 16.5 ms, see Figure 7.8. With $N_p = 1$ the system would be exposed to unwanted oscillations.

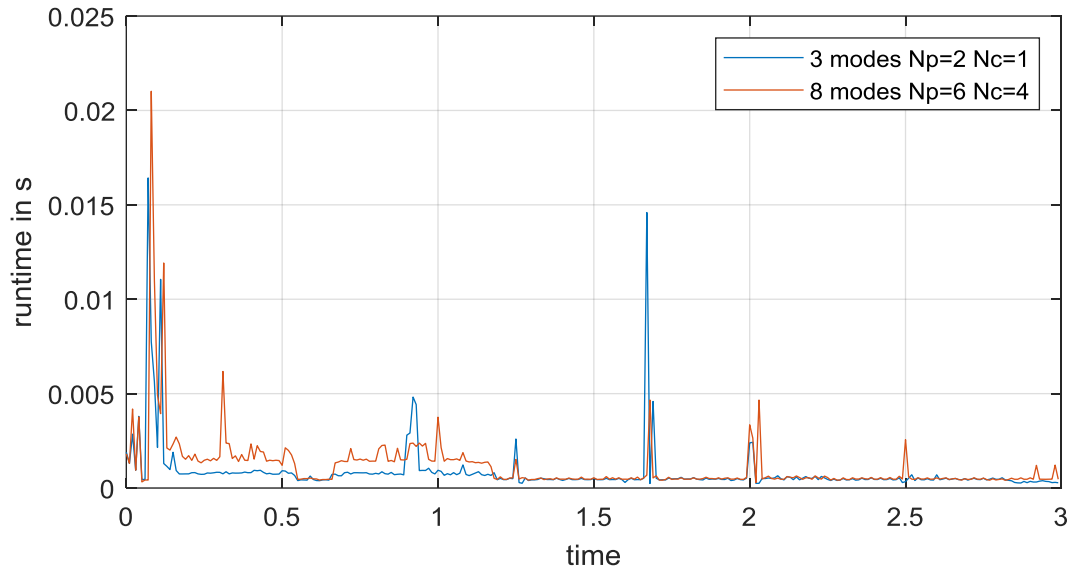


Figure 7.8. Comparison of the runtime of the constraint MPC control with $N_p = 6$ and $N_c = 4$, 8 modes used and the minimal MPC control with $N_p=2$ and $N_c=1$ and 3 modes used.

Figure 7.9 illustrates the deflection response of the structure $w(x_{s1})$ with the MPC control with 3 modes (red continuous). The calculated \mathbf{u} is fed into a model with 12 Modes, which is a more accurate representation of the actual structure. It can be noticed that the MPC control simulated with 3 modes is able to reduce the deflection response also for the structure, which should be modelled especially for the two-span beam with a higher number of modes, not smaller than 8.

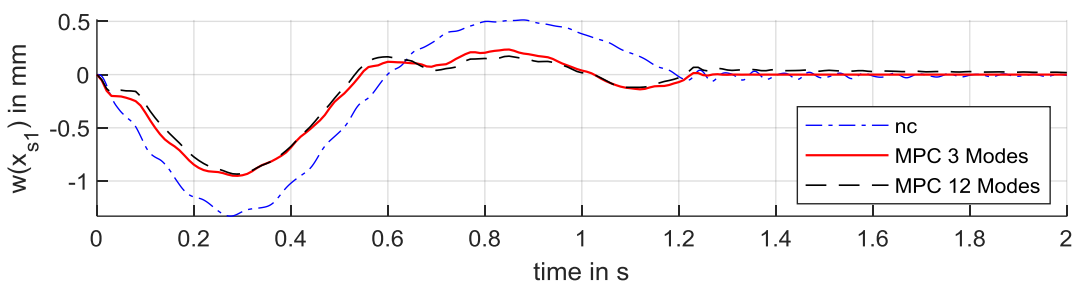


Figure 7.9. Deflection responses $w(x_{s1})$ for the uncontrolled structure (blue dash-dotted), of the MPC controlled structure with 3 modes (red continuous), and the 12 modes structure fed with \mathbf{u} of the 3 modes MPC (black dotted).

7.4 Concluding Remarks

Theoretically, an efficient control approach was accomplished for the one-span and two-span structure. The saturation limits of the actuators can be taken into account online. The control could also take into account the change of the system variables and update the control matrices $\mathbf{F}(k)$ and $\mathbf{\Phi}(k)$ accordingly. This might be of special interest when the structure is excited by a stream of random moving masses. As the control relies on the availability of the state variables, they have to be calculated through state estimation techniques presented in sections 4.1 and 4.2.

In [79] Wang introduces a set of orthonormal basis functions into the design process. The future incremental control trajectory $\Delta u(k_i + m), m = 0.1.2 \dots$ is expressed using a set of Laguerre functions. The problem of finding the future incremental control trajectory is converted into one of finding the set of optimal coefficients for the expansion. The Laguerre function offers simplicity for programming. With their use the runtime could be reduced for real-time applications. In [87] the Laguerre function approach is utilised by Oveisi et al. to actively control a lightly damped cantilever beam. A recursive least square algorithm is used to estimate the disturbance signal. The system model is constructed by a frequency domain subspace system identification. Classical dual-mode control system can guarantee stability. Classical infinite horizon LQR LQG controller guarantee stable closed-loop systems [80]. However, they can only be used for unconstrained systems. The dual-mode MPC uses first a predictive controller with constraints that brings the states to a terminal constraint set \mathbf{X}_0 , that contains the origin [79,110]. From there classical infinite horizon controller can be used to stabilize the system. The cost function for a dual mode problem can be written as [109,111]

$$J_k = \sum_{i=0}^{n-1} (\mathbf{x}_{(k+i)}^T \mathbf{Q} \mathbf{x}_{(k+i)} + \mathbf{u}_{(k+i)}^T \mathbf{R} \mathbf{u}_{(k+i)}) + \mathbf{x}_{(k+i)}^T \mathbf{P}_{f(k)} \mathbf{x}_{(k+i)} \quad (7.31)$$

It utilises free inputs for the first n steps and a fixed feedback controller afterwards. $\mathbf{P}_{f(k)}$ is the solution of the unconstrained, infinite horizon quadratic regulation problem [112]. For a nominal model this could be determined by a Lyapunov equation [112]. In [109] Takacs et al. computed $\mathbf{P}_{f(k)}$ online with the discrete-time algebraic Riccati equation due to parameter changes in the model.

Takács et al. applied an adaptive-predictive control to a cantilever beam using extended Kalman filtering to approximate the system states and the model parameter. The continuous beam was simplified by a 1 DOF system taking into account the first resonant frequency.

8 Conclusions and Future Work

The present study is one of the few that extended numerical investigations of the problem of controlling beam structures subjected to a set of moving masses. It presented and analysed the synthesis and experimental implementation of active control on two small-scale test structures. This comprised an original method of state estimation, a novel gain scheduling approach with adaptation of the optimal time-variant gain towards the load's speed and masses, first time implementation of an augmented control system. MFC actuators were modelled and experimentally validated for the moving mass control problem and for the first time the MPC control approach was numerically studied for the beam structures acted upon by moving masses.

Numerical models for the simply supported beam and the two-span continuous beams were derived in modal coordinates and validated successfully against experimental displacement data. Two mathematical models for the chosen electrodynamic actuator were presented. For frequencies up to 10 Hz a simplified first order model can be utilised, which can be included in the state space representation as a beam-shaker system. The beam-shaker system was validated successfully against experimental displacement data for the simply supported beam. For higher frequencies the numerical FRF of the transferred force over input voltage revealed a higher complexity, especially the resonance of the transferred force over input voltage at 27 Hz has to be treated with caution to avoid instabilities.

In chapter 3 optimal control approaches relevant for the time-varying moving mass problem were presented. In the optimal finite time control approach the algebraic Riccati equation can be solved backwards for a given final time. This method is preferred as it meets the condition of optimality.

Inherent problems which result from the experimental implementation of active control solutions of the moving mass problem were tackled. These are: 1. States of the system must be estimated as they are not directly measurable. 2. Implementations in discrete time come with discretization errors. Two state estimator techniques were studied in this regard in chapter 3.2. Although the classical discrete time observer represented the states accurately for the open-loop case, the discrete time observer-based feedback control was prone to discretization errors at the given sampling time and actuator position and even worsened the structural deflection response. Whereas estimation based on the mode shape vector proved

to be straightforward to implement and offers excellent real-time abilities. Because of that, the superior properties of this technique were applied successfully for the application of the finite time optimal control approach. Detailed experimental validation in that context was presented in chapter 5, where the reduced order control was applied to the electrodynamic shaker located close to one of the simply supported beam supports. The first order actuator model proved correct while contact is maintained, a small inaccuracy is observed when the mass leaves the beam. As expected, due to the time-varying nature of the control system, it was shown both experimentally and numerically that a control method based on a terminal-time optimal control solution provides better performance than a time invariant optimal controller. Especially the augmented system approach taking into account the moving load in the system equation proved very effective with a reduction of the maximum deflection of up to 38%. The possibility of using different moving masses travelling at different speeds also pointed toward a control solution that adapts the control effort, taking into account the type of load. Therefore, a simple gain scheduling solution that makes a better use of the control effort is presented and proves to be the basis of further work and developments of the method.

The numerical models of 33-mode MFC actuator attached to the test structures were presented in modal coordinates and validated successfully against experimental displacement data. 33-mode MFC actuators were applied for the first time to control a simply supported beam and a two-span beam acted upon moving masses. Although MFC actuators are currently not particularly made for the control of bridge structures due to their limited actuation force, these studies are also relevant for the application in control of general light structures like linear robots or aeroelastic structures subjected to transient loads.

Two control approaches were studied for the MFC controlled structures, straightforward displacement control and more sophisticated MPC control. Results of the Linear and nonlinear cubic displacement feedback controls implemented on the one-span and two-span test rig were presented in chapter 6. Each span was controlled by a collocated laser displacement sensor MFC-actuator pair. The cubic displacement rule proved more efficient for higher masses, where a maximum reduction of 18% was reached for the simply supported beam. At which the linear control reduces the maximum deflection more effectively for smaller masses with approx. 10% deflection reduction. This feedback controls offers the advantage of a straightforward way of implementation. In addition, a stream of multiple masses can be controlled easily. Hereby a reduction of the maximum deflection of 10% was

achieved. A drawback is that the actuator saturation limits could not be reached without undermining the system stability.

To include the saturation limits of the MFC-actuator the MPC control was studied numerically and for the first time in combination with the moving mass problem. With the help of quadratic programming, inequality constraints were considered in the optimization process. Theoretically the maximum deflection can be reduced by 22% for the one-span beam and by 29% when the mass travels on the first span of the two-span beam.

Table 8.1 summarizes the achieved performance, which is the reduction of the maximum deflection, for the different control approaches for the two test structures when mass $m = 0.509$ kg is traversing.

Table 8.1 Main results summerized for mass $m=0.509$ kg, comparing different control approaches

Control Method	Structure	Actuator	Reduction maximum deflection
Finite time optimal control	Simply supported beam	Electro Dynamic	18%
Finite time optimal control (augmented model)	Simply supported beam	Electro Dynamic	38%
Linear Displacement feedback	Simply supported beam	Piezoelectric MFC patch	11%
Cubic Displacement feedback	Simply supported beam		18%
Linear Displacement feedback	Two-span beam	Piezoelectric MFC patch	10 %
Cubic Displacement feedback	Two-span beam	Piezoelectric MFC patch	13 %

Model Predictive Control (numerical)	Simply supported beam	Piezoelectric MFC patch	22%
Model Predictive Control (numerical)	Two-span beam	Piezoelectric MFC patch	29 %

All in all, it can be said that this study successfully solved vital problems concerned with experimental implementation of active control of single and two-span moving mass beam structures.

Main contribution to knowledge

- Implementation of active control solutions on two small scale rigs. This includes the reduced order finite time control of a simply supported beam [28]
- The limitations of observer based feedback control for the moving mass problem where stated. The studied discrete linear quadratic regulator was prone to discretization errors. State estimation by mode shapes proved very efficient and capable of being implemented in real-time.
- For the first time MFC actuators were applied experimentally to the simply supported beam and the two-span continuous beam for active control of a moving mass structure. This was achieved by using direct displacement feedback, which was validated experimentally.
- Further the MPC approach was applied successfully for the first time to a moving load structure numerically. This complex control approach can handle control constraints online in the optimal control approach

Future work

It was shown that it is crucial for the application of active control approaches of moving load structures to estimates the states correctly. For the further application of active control approaches of slender structures subjected to transient loads crucial points are the state estimation and the real-time ability of control algorithms. With a changed actuator location and the pushing of the hardware limits also classical discrete observer techniques could deliver precise modal states. The practical application of the MPC approach requires powerful hardware capable of solving the quadratic programming problem in the required

sampling time. The approach seems very promising with its constraint handling abilities. Moreover, a stream of moving masses can be considered in future studies as the control input is calculated online.

Future experimental studies could include controlled cars with variable speeds, where the gains adapt in real-time. The presented finite-time optimal control approach was limited to one mass moving on the structure. It can also be applied for the case of multiple masses travelling on the structure but still the leaving times have to be known in advance for the gain calculation. For a real-time implementation of the problem of multiple masses travelling on the beam, it has to be solved how the variant gains calculated for each specific mass beforehand could be interpolated for the various multi mass cases. The displacement feedback control approaches presented proved capable of controlling the structure subjected to a stream of moving loads. However, stability and robustness issues have to be considered in more detail in the future. The study could be unscaled to a real moving mass structures. Robustness of the sensors and the actuators against environmental influences like wind and rain has to be proven to guarantee the safety and functionality of the system.

The present study was based on a simply supported Euler Bernoulli beam. For real applications the system model might be more difficult to derive. System identification methods could be applied like the Receptance Method [113,114] where a non-parametric system model is utilised for the control approach.

The general problem studied in this thesis is the control of flexible structures subjected to time varying loads. Apart from bridge-vehicle interactions this study could also be applied in a wide field of applications. For example in 3D printer heads [115], the vertical vibrations of the nozzle are influenced by different feed parameters. These vibrations influence the printing quality. Portal cranes or more specifically ship unloaders are another so far less studied example of a moving load structure [116]. The interaction between the lifting boom and the moving system can lead to high stresses, which have to be assessed as accurate as possible to determine its fatigue life. The problem is characterized by a high DAF of 1.5, which makes it necessary to include the inertia effect into the equations of motion [116]. Another important field of application is aeroelasticity, the interaction between aerodynamic loads and a non-rigid wing structure, which has a wide range of applications, e.g. active morphing of wings [23,117], flutter control [118,119] or aeroelastic loads of wind turbine blades [120]. Aerodynamic loads affect the stiffness and the damping in a similar way as

presented in this study, as they depend on the air speed and air density which might change in time [93].

Publications by the Author

a) Journal paper

- Sievert, L., Stancioiu, D., and Matthews, C., 2021, “Active Vibration Control of a Small-Scale Flexible Structure Subject to Moving-Loads and Experimental Validation,” *J. Vib. Acoust.*, **143**(6).

b) Conference papers

- Sievert, L. , Stancioiu, D., 2019, “Model-Based Time-Varying Predictive Vibration Control of a Beam Structure Subjected to Moving Masses ” , *ASIM Fachgruppentreffen (Conference of the Association for Simulation in the German Speaking Area)*, Braunschweig, Germany
- Sievert, L., Stancioiu, D., Matthews, C., Rothwell, G., and Jenkinson, I., 2019, “Numerical and Experimental Investigation of Time-Varying Vibration Control for Beam Subjected to Moving Masses,” *International Conference on Structural Engineering Dynamics, ICEDyn*, Viana do Castelo, Portugal.

9 Appendix

The Normal Mode of the Simply Supported Beam

The general solution for the normal mode or characteristic equation is given as

$$\psi(x) = C_1 \sin(\beta x) + C_2 \cos(\beta x) + C_3 \sinh(\beta x) + C_4 \cosh(\beta x) \quad (9.1)$$

Where C_1, C_2, C_3 and C_4 are constants, which can be found from the boundary conditions, which for the simply supported beam are

$$\psi(0) = 0 \quad (9.2)$$

$$\psi(L) = 0 \quad (9.3)$$

$$\psi''(0) = 0 \quad (9.4)$$

$$\psi''(L) = 0 \quad (9.5)$$

The second derivative of equation (9.1) is

$$\psi''(x) = -C_1 \sin(\beta x) - C_2 \cos(\beta x) + C_3 \sinh(\beta x) + C_4 \cosh(\beta x) \quad (9.6)$$

Using condition (9.2) in equation (9.1) gives $C_2 = -C_4$ and using condition (9.4) in equation (9.6) gives $C_2 = C_4$. As a result $C_2 = C_4 = 0$. Using condition (9.3) and (9.5) gives

$$\psi(L) = C_1 \sin(\beta L) + C_3 \sinh(\beta L) = 0 \quad (9.7)$$

$$\psi(L) = -C_1 \sin(\beta L) + C_3 \sinh(\beta L) = 0 \quad (9.8)$$

Substituting equation (9.7) in equation (9.8) $C_3 = 0$. The normal mode of a simply supported beam is

$$\psi(x) = C_1 \sin(\beta x) \quad (9.9)$$

Equation (9.7) and (9.8) is a homogeneous equation system. For the nontrivial solution for C_1 and C_3 the determinant of the coefficients must be equal to zero. This leads to

$$\sin(\beta L) = 0 \quad (9.10)$$

The root of equation (9.10) are given by

$$\beta_n L = j\pi, \quad \text{with } j = 1, 2, 3 \dots \quad (9.11)$$

; see [88,89].

Inserting equation (9.11) in equation (9.9) gives the normal mode for the simply supported beam

$$\psi(x) = \sin\left(\frac{j\pi x}{L}\right) \quad (9.12)$$

The natural frequencies of vibrations become

$$\omega_n = (\beta_n l)^2 \sqrt{\frac{EI}{\rho A l^4}} = (n\pi)^2 \sqrt{\frac{EI}{\rho A l^4}} \quad (9.13)$$

The Dirac Delta Function

The Dirac delta function (also called Dirac impulse function) is defined as [8]:

$$\delta(x) = \frac{dH(x)}{dx} \quad (9.14)$$

With $H(x)$ defined as the Heaviside function:

$$H(x) = \begin{cases} 0 & \text{for } x < 0 \\ 1 & \text{for } x \geq 0 \end{cases} \quad (9.15)$$

The following relations hold for the Dirac delta function (a, b, ξ denote constants and $f(x)$ is a continuous function in the interval (a, b))

$$\int_{-\infty}^{\infty} \delta(x) dx = 1 \quad (9.16)$$

$$\int_{-\infty}^{\infty} \delta(x - a) f(x) dx = f(a) \quad (9.17)$$

List of References

- [1] Stancioiu, D., James, S., Ouyang, H., and Mottershead, J. E., 2009, “Vibration of a Continuous Beam Excited by a Moving Mass and Experimental Validation,” *Journal of Physics: Conference Series*.
- [2] Ouyang, H., 2011, “Moving-Load Dynamic Problems: A Tutorial (with a Brief Overview),” *Mech. Syst. Signal Process.*, **25**(6), pp. 2039–2060.
- [3] Korkmaz, S., 2011, “A Review of Active Structural Control: Challenges for Engineering Informatics,” *Comput. Struct.*, **89**(23–24), pp. 2113–2132.
- [4] Marcheggiani, L., and Lenci, S., 2010, “On a Model for the Pedestrians-Induced Lateral Vibrations of Footbridges,” *Meccanica*, **45**(4), pp. 531–551.
- [5] Yang, J., Ouyang, H., Stancioiu, D., Cao, S., and He, X., 2018, “Dynamic Responses of a Four-Span Continuous Plate Structure Subjected to Moving Cars With Time-Varying Speeds,” *J. Vib. Acoust. Trans. ASME*, **140**(6), pp. 1–15.
- [6] Kong, E., Song, J. S., Kang, B. B., and Na, S., 2011, “Dynamic Response and Robust Control of Coupled Maglev Vehicle and Guideway System,” *J. Sound Vib.*, **330**(25), pp. 6237–6253.
- [7] Lee, K., Cho, Y., and Chung, J., 2012, “Dynamic Contact Analysis of a Tensioned Beam with a Moving Massspring System,” *J. Sound Vib.*, **331**(11), pp. 2520–2531.
- [8] Frýba, L., 1999, *Vibration of Solids and Structures under Moving Loads*, Thomas Telford Publishing, Prague.
- [9] Younesian, D., Kargarnovin, M. H., and Esmailzadeh, E., 2008, “Optimal Passive Vibration Control of Timoshenko Beams with Arbitrary Boundary Conditions Traversed by Moving Loads,” *Proc. Inst. Mech. Eng. Part K J. Multi-body Dyn.*, **222**(2), pp. 179–188.
- [10] Živanović, S., Pavic, A., and Reynolds, P., 2005, “Vibration Serviceability of Footbridges under Human-Induced Excitation: A Literature Review,” *J. Sound Vib.*, **279**(1–2), pp. 1–74.

- [11] Xiaomin Shi, and Cai, C. S., 2008, "Suppression of Vehicle-Induced Bridge Vibration Using Tuned Mass Damper," *J. Vib. Control*, **14**(7), pp. 1037–1054.
- [12] Pierson, H., Brevick, J., and Hubbard, K., 2013, "The Effect of Discrete Viscous Damping on the Transverse Vibration of Beams," *J. Sound Vib.*, **332**(18), pp. 4045–4053.
- [13] Debnath, N., Deb, S., and Dutta, A., 2016, "Multi-Modal Vibration Control of Truss Bridges with Tuned Mass Dampers under General Loading," *J. Vib. Control*, **22**(20), pp. 4121–4140.
- [14] Adam, C., Di Lorenzo, S., Failla, G., and Pirrotta, A., 2017, "On the Moving Load Problem in Beam Structures Equipped with Tuned Mass Dampers," *Meccanica*, **52**(13), pp. 3101–3115.
- [15] Brecher, C., Fey, M., Brockmann, B., and Chavan, P., 2018, "Multivariable Control of Active Vibration Compensation Modules of a Portal Milling Machine," *J. Vib. Control*, **24**(1), pp. 3–17.
- [16] Frischgesell, T., Popp, K., Reckmann, H., and Schütte, O., 1998, "Regelung Eines Elastischen Fahrwegs Unter Verwendung Eines Variablen Beobachters (Control of an Elastic Guideway by Use of a Variable Observer)," *Tech. Mech.*, **18**(1), pp. 45–55.
- [17] Reckmann, H., and Popp, K., 2000, "Deflection and Vibration Control of an Elastic Guideway Under a Moving Mass," *IFAC Proc. Vol.*, **33**(26), pp. 947–952.
- [18] Zhang, S. Q., Li, Y. X., and Schmidt, R., 2015, "Modeling and Simulation of Macro-Fiber Composite Layered Smart Structures," *Compos. Struct.*, **126**, pp. 89–100.
- [19] Ghandchi Tehrani, M., and Kalkowski, M. K., 2016, "Active Control of Parametrically Excited Systems," *J. Intell. Mater. Syst. Struct.*, **27**(9), pp. 1218–1230.
- [20] Sodano, H. A., Park, G., and Inman, D. J., 2004, "An Investigation into the Performance of Macro-Fiber Composites for Sensing and Structural Vibration Applications," *Mech. Syst. Signal Process.*, **18**(3), pp. 683–697.
- [21] Song, M. K., Noh, H. C., and Choi, C. K., 2003, "A New Three-Dimensional Finite Element Analysis Model of High-Speed Train-Bridge Interactions," *Eng. Struct.*, **25**(13), pp. 1611–1626.

- [22] Song, G., Sethi, V., and Li, H. N., 2006, "Vibration Control of Civil Structures Using Piezoceramic Smart Materials: A Review," *Eng. Struct.*, **28**(11), pp. 1513–1524.
- [23] Wang, X., Zhou, W., and Wu, Z., 2018, "Feedback Tracking Control for Dynamic Morphing of Piezocomposite Actuated Flexible Wings," *J. Sound Vib.*, **416**, pp. 17–28.
- [24] Prakash, S., Kumar, T. G. R., Raja, S., Dwarakanathan, D., Subramani, H., and Karthikeyan, C., 2016, "Active Vibration Control of a Full Scale Aircraft Wing Using a Recon Fi Gurable Controller," *J. Sound Vib.*, **361**, pp. 32–49.
- [25] Nikkhoo, A., 2014, "Investigating the Behavior of Smart Thin Beams with Piezoelectric Actuators under Dynamic Loads," *Mech. Syst. Signal Process.*, **45**(2), pp. 513–530.
- [26] Nikkhoo, A., Rofooei, F. R., and Shadnam, M. R., 2007, "Dynamic Behavior and Modal Control of Beams under Moving Mass," *J. Sound Vib.*, **306**, pp. 712–724.
- [27] Visweswara Rao, G., 2000, "Linear Dynamics of an Elastic Beam under Moving Loads," *J. Vib. Acoust. Trans. ASME*, **122**(3), pp. 281–289.
- [28] Sievert, L., Stancioiu, D., and Matthews, C., 2021, "Active Vibration Control of a Small-Scale Flexible Structure Subject to Moving-Loads and Experimental Validation," *J. Vib. Acoust.*, **143**(6).
- [29] Stancioiu, D., and Ouyang, H., 2016, "Optimal Vibration Control of Beams Subjected to a Mass Moving at Constant Speed," *J. Vib. Control*, **22**(14), pp. 3202–3217.
- [30] Shelley, S. J., Aktan, A. E., and Frederick, N., 1993, "Active Vibration Control of a 250 Foot Span Steel Truss Highway Bridge," *Proc. IEEE Conf. Control Appl.*, **1**, pp. 119–120.
- [31] Frýba, L., 1999, "Vibration of Solids and Structures under Moving Loads," Thomas Telford Publishing, Prague, pp. 51–56.
- [32] Bilello, C., Bergman, L. A., and Kuchma, D., 2004, "Experimental Investigation of a Small-Scale Bridge Model under a Moving Mass," *J. Struct. Eng.*, **130**(5), pp. 799–804.
- [33] Stăncioiu, D., and Ouyang, H., 2012, "Structural Modification Formula and Iterative

Design Method Using Multiple Tuned Mass Dampers for Structures Subjected to Moving Loads,” *Mech. Syst. Signal Process.*, **28**, pp. 542–560.

- [34] Yang, J., Ouyang, H., and Stancioiu, D., 2017, “Numerical Studies of Vibration of Four-Span Continuous Plate with Rails Excited by Moving Car with Experimental Validation,” *Int. J. Struct. Stab. Dyn.*, **17**(10).
- [35] Yang, J., 2017, “Theoretical and Laboratory Experimental Studies of Vehicle-Excited Bridge Vibration.”
- [36] Teng, Y., Teng, N., and Kou, X., 2008, “Vibration Analysis of Continuous Maglev Guideway Considering the Magnetic Levitation System,” *J. Shanghai Jiaotong Univ.*, **13**(2), pp. 211–215.
- [37] Stancioiu, D., Ouyang, H., Mottershead, J. E., and James, S., 2011, “Experimental Investigations of a Multi-Span Flexible Structure Subjected to Moving Masses,” *J. Sound Vib.*, **330**(9), pp. 2004–2016.
- [38] Stăncioiu, D., Ouyang, H., and Mottershead, J. E., 2009, “Vibration of a Continuous Beam with Multiple Elastic Supports Excited by a Moving Two-Axle System with Separation,” *Meccanica*, **44**(3), pp. 293–303.
- [39] Nikkhoo, A., 2014, “Investigating the Behavior of Smart Thin Beams with Piezoelectric Actuators under Dynamic Loads,” *Mech. Syst. Signal Process.*, **45**(2), pp. 513–530.
- [40] Stancioiu, D., and Ouyang, H., 2016, “Model-Based Active Control of a Continuous Structure Subjected to Moving Loads,” *J. Phys. Conf. Ser.*, **744**, p. 012001.
- [41] Stancioiu, D., and Yang, H. O. J., 2021, “Numerical and Experimental Investigations into Feedback Control of Continuous Beam Structures under Moving Loads,” *Arch. Appl. Mech.*, **91**(6), pp. 2641–2659.
- [42] Preumont, A., 2011, *Vibration Control of Active Structures*, Springer Netherlands, Dordrecht.
- [43] Balas, M. J., 1978, “Active Control of Flexible Systems,” *J. Optim. Theory Appl.*, **25**(3), pp. 415–436.
- [44] GOH, C. J., and CAUGHEY, T. K., 1985, “On the Stability Problem Caused by Finite

- Actuator Dynamics in the Collocated Control of Large Space Structures,” *Int. J. Control*, **41**(3), pp. 787–802.
- [45] Friswell, M. I., and Inman, D. J., 1999, “The Relationship between Positive Position Feedback and Output Feedback Controllers,” *Smart Mater. Struct.*, **8**(3), pp. 285–291.
- [46] Omid, E., and Mahmoodi, S. N., 2015, “Consensus Positive Position Feedback Control for Vibration Attenuation of Smart Structures.”
- [47] Shan, J., 2005, “Slewing and Vibration Control of a Single-Link Flexible Manipulator by Positive Position Feedback (PPF),” **15**, pp. 487–503.
- [48] Omid, E., McCarty, R., and Mahmoodi, S. N., 2014, “Implementation of Modified Positive Velocity Feedback Controller for Active Vibration Control in Smart Structures,” W.-H. Liao, ed., p. 90571N.
- [49] Mahmoodi, S. N., and Ahmadian, M., 2010, “Modified Acceleration Feedback for Active Vibration Control of Aerospace Structures.”
- [50] Sung, Y.-G., 2002, “Modelling and Control with Piezoactuators for a Simply Supported Beam under a Moving Mass,” *J. Sound Vib.*, **250**(4), pp. 617–626.
- [51] Deng, F., Rémond, D., and Gaudiller, L., 2011, “Self-Adaptive Modal Control for Time-Varying Structures,” *J. Sound Vib.*, **330**(14), pp. 3301–3315.
- [52] Deng, F., Rémond, D., and Gaudiller, L., 2010, “Modal Control Using Real-Time Identification for Time-Varying Structures,” *Mécanique Ind.*, **11**(6), pp. 513–520.
- [53] Rofooei, F. R., and Nikkhoo, A., 2009, “Application of Active Piezoelectric Patches in Controlling the Dynamic Response of a Thin Rectangular Plate under a Moving Mass,” *Int. J. Solids Struct.*, **46**(11–12), pp. 2429–2443.
- [54] Naidu, D. S., 2003, *Optimal Control Systems*, CRC Press, Boca Raton.
- [55] Pi, Y., and Ouyang, H., 2016, “Vibration Control of Beams Subjected to a Moving Mass Using a Successively Combined Control Method,” *Appl. Math. Model.*, **40**(5–6), pp. 4002–4015.
- [56] Caughey, T. K., 1985, “On the Stability Problem Caused by Finite Actuator Dynamics in the Collocated Control of Large Space Structures,” *Int. J. Control*, **41**(3), pp. 787–802.

- [57] Nima Mahmoodi, S., Ahmadian, M., and Inman, D. J., 2010, “Adaptive Modified Positive Position Feedback for Active Vibration Control of Structures,” *J. Intell. Mater. Syst. Struct.*, **21**(6), pp. 571–580.
- [58] Liu, X., Wang, Y., and Ren, X., 2020, “Optimal Vibration Control of Moving-Mass Beam Systems with Uncertainty,” *J. Low Freq. Noise, Vib. Act. Control*, **39**(3), pp. 803–817.
- [59] Shelley, S. J., Lee, K. L., Aksel, T., and Aktan, A. E., 1995, “Active-Control and Forced-Vibration Studies on Highway Bridge,” *J. Struct. Eng.*, **121**(9), pp. 1306–1312.
- [60] Bleicher, A., Schlaich, M., and Schauer, T., 2011, “Multimodal and Multivariable Active Vibration Control for a Footbridge - Model-Based Design and Experimental Validation,” *Proceedings of the 8th International Conference on Structural Dynamics, EURODYN 2011*, pp. 1525–1532.
- [61] Pisarski, D., 2018, “Optimal Control of Structures Subjected to Traveling Load,” *J. Vib. Control*, **24**(7), pp. 1283–1299.
- [62] Pisarski, D., and Myśliński, A., 2018, “Online Adaptive Semi-Active Vibration Damping of Slender Structures Subject to Moving Loads,” *MATEC Web Conf.*, **148**, pp. 05006-.
- [63] Sievert, L., Stancioiu, D., Matthews, C., Rothwell, G., and Jenkinson, I., 2019, “Numerical and Experimental Investigation of Time-Varying Vibration Control for Beam Subjected to Moving Masses,” *International Conference on Structural Engineering Dynamics, ICEDyn*, Viana do Castelo, Portugal.
- [64] Sloss, J. M., Adali, S., Sadek, I. S., and Bruch, J. C., 1988, “Displacement Feedback Control of Beams under Moving Loads,” *J. Sound Vib.*, **122**(3), pp. 457–464.
- [65] Abdeljaber, O., Avci, O., and Inman, D. J., 2016, “Active Vibration Control of Flexible Cantilever Plates Using Piezoelectric Materials and Artificial Neural Networks,” *J. Sound Vib.*, **363**, pp. 33–53.
- [66] Shahab, S., and Erturk, A., 2017, “Coupling of Experimentally Validated Electroelastic Dynamics and Mixing Rules Formulation for Macro-Fiber Composite Piezoelectric Structures,” *J. Intell. Mater. Syst. Struct.*, **28**(12), pp. 1575–1588.

- [67] Hagood, N., and Bent, A., 1993, “Development of Piezoelectric Fiber Composites for Structural Actuation,” *34th Structures, Structural Dynamics and Materials Conference*, American Institute of Aeronautics and Astronautics, Reston, Virginia, pp. 454–454.
- [68] Bent, A. A., and Hagood, N. W., 1997, “Piezoelectric Fiber Composites with Interdigitated Electrodes,” *J. Intell. Mater. Syst. Struct.*, **8**(11), pp. 903–919.
- [69] Wilkie, W. K., Bryant, R. G., High, J. W., Fox, R. L., Hellbaum, R. F., Jalink, Jr., A., Little, B. D., and Mirick, P. H., 2000, “Low-Cost Piezocomposite Actuator for Structural Control Applications,” *Smart Structures and Materials 2000: Industrial and Commercial Applications of Smart Structures Technologies*, J.H. Jacobs, ed., pp. 323–334.
- [70] Pu, Y., Zhou, H., and Meng, Z., 2019, “Multi-Channel Adaptive Active Vibration Control of Piezoelectric Smart Plate with Online Secondary Path Modelling Using PZT Patches,” *Mech. Syst. Signal Process.*, **120**, pp. 166–179.
- [71] Shin, C., Hong, C., and Bong, W., 2012, “Active Vibration Control of Beam Structures Using Acceleration Feedback Control with Piezoceramic Actuators,” *J. Sound Vib.*, **331**(6), pp. 1257–1269.
- [72] Trindade, M. A., Pagani, C. C., and Oliveira, L. P. R., 2015, “Semi-Modal Active Vibration Control of Plates Using Discrete Piezoelectric Modal Filters,” *J. Sound Vib.*, **351**, pp. 17–28.
- [73] Zhao, L., and Wu, Y. P., 2019, “Active Vibration Control of Rotating Beam with Moving Mass Using Piezoelectric Actuator,” *J. Vibroengineering*, **21**(5), pp. 1330–1341.
- [74] Kiral, Z., Malgaca, L., and Akdağ, M., 2008, “Active Control of Residual Vibrations of a Cantilever Smart Beam,” *Turkish J. Eng. Environ. Sci.*, **32**(1), pp. 51–57.
- [75] Eldalil, K. M. S., and Baz, A. M. S., 2009, “Dynamic Stability of Cylindrical Shells under Moving Loads by Applying Advanced Controlling Techniques—Part II: Using Piezo-Stack Control,” *Adv. Acoust. Vib.*, **2009**, pp. 1–7.
- [76] Eldalil, K. M. S., and Baz, A. M. S., 2009, “Dynamic Stability of Cylindrical Shells under Moving Loads by Applying Advanced Controlling Techniques Part I—Using

- Periodic Stiffeners,” *Adv. Acoust. Vib.*, **2009**(June 2014), pp. 1–17.
- [77] Takács, G., and Rohal’-Ilkiv, B., 2014, “Model Predictive Control Algorithms for Active Vibration Control: A Study on Timing, Performance and Implementation Properties,” *JVC/Journal Vib. Control*, **20**(13), pp. 2061–2080.
- [78] Maciejowski, J. M., 2001, *Predictive Control with Constraints*, Pearson Education, London.
- [79] Wang, L., 2009, *Model Predictive Control System Design and Implementation Using MATLAB®*, Springer London, London.
- [80] Camacho, E. F., and Bordons, C., 2007, *Model Predictive Control*, Springer London, London.
- [81] Lin, C., and Huang, Y., 2016, “Enhancing Vibration Suppression in a Periodically Excited Flexible Beam by Using a Repetitive Model Predictive Control Strategy,” (May 2014).
- [82] Bossi, L., Rottenbacher, C., Mimmi, G., and Magni, L., 2011, “Multivariable Predictive Control for Vibrating Structures: An Application,” *Control Eng. Pract.*, **19**(10), pp. 1087–1098.
- [83] Richelot, J., Guibe, J. B., and Budinger, V. P., 2004, “Active Control of a Clamped Beam Equipped with Piezoelectric Actuator and Sensor Using Generalized Predictive Control,” *IEEE Int. Symp. Ind. Electron.*, **1**, pp. 583–588.
- [84] Hassan, M., Dubay, R., Li, C., and Wang, R., 2007, “Active Vibration Control of a Flexible One-Link Manipulator Using a Multivariable Predictive Controller,” *Mechatronics*, **17**(6), pp. 311–323.
- [85] Wills, A. G., Bates, D., Member, S., Fleming, A. J., Ninness, B., Moheimani, S. O. R., and Member, S., 2008, “Model Predictive Control Applied to Constraint Handling in Active Noise and Vibration Control,” **16**(1), pp. 3–12.
- [86] Takács, G., Polóni, T., and Rohal, B., 2014, “Adaptive Model Predictive Vibration Control of a Cantilever Beam with Real-Time Parameter Estimation,” **2014**.
- [87] Oveisi, A., 2018, “Observer - Based Repetitive Model Predictive Control in Active Vibration Suppression,” (August 2017), pp. 1–23.

- [88] Rao, S. S., 2007, *Vibration of Continuous Systems*, John Wiley & Sons, Hoboken.
- [89] Rao, S. S., 2018, *Mechanical Vibrations Sixth Edition in SI Units*, Pearson Education, Harlow.
- [90] Nikkhoo, A., Amankhani, M., and Ghafari, H., 2014, "Vibration Suppression in Smart Thin Beams with Piezoelectric Actuators under a Moving Load / Mass Accounting for Large Deflections of the Base Structure," *7*(February), pp. 211–220.
- [91] Wu, J. S., and Lin, T. L., 1990, "Free Vibration Analysis of a Uniform Cantilever Beam with Point Masses by an Analytical-and-Numerical-Combined Method," *J. Sound Vib.*, **136**(2), pp. 201–213.
- [92] De Silva, C. W., 2000, *Vibration Fundamentals and Practice*, CRC Press, Boca Rota.
- [93] Ewans, D., *Encyclopedia of Vibration*, Academic Press Inc., San Diego.
- [94] Waters, T. P., 2019, "A Chirp Excitation for Focussing Flexural Waves," *J. Sound Vib.*, **439**, pp. 113–128.
- [95] Lang, G. F., 1997, "Electrodynamic Shaker Fundamentals," *S V Sound Vib.*, **31**(4), pp. 14–23.
- [96] Kyprianou, A., Mottershead, J. E., and Ouyang, H., 2005, "Structural Modification. Part 2: Assignment of Natural Frequencies and Antiresonances by an Added Beam," *J. Sound Vib.*, **284**(1–2), pp. 267–281.
- [97] Stanišić, M. M., 1985, "On a New Theory of the Dynamic Behavior of the Structures Carrying Moving Masses," *Ingenieur-Archiv*, **55**(3), pp. 176–185.
- [98] McConnell, K. G., and Varoto, P. S., 2008, *Vibration Testing: Theory and Practice*, Wiley, New York.
- [99] De Oliveira, L. P. R., Varoto, P. S., and Peres, M. A. S., 2011, "Shaker Structure Interaction: Overview and Updated Results," *18th Int. Congr. Sound Vib. 2011, ICSV 2011*, **3**(July), pp. 2516–2523.
- [100] Wang, Y., Wei, Q., Shi, J., and Long, X., 2010, "Resonance Characteristics of Two-Span Continuous Beam under Moving High Speed Trains," *Lat. Am. J. Solids Struct.*, **7**(2), pp. 185–199.

- [101] Smart-material, “Macro Fiber Composite - MFC Data Sheet” [Online]. Available: https://www.smart-material.com/media/Datasheets/MFC_V2.4-datasheet-web.pdf. [Accessed: 02-Oct-2021].
- [102] Dorf, R. C., and Bishop, R. H., 2011, *Modern Control Systems*, Prentice Hall, Upper Saddle River.
- [103] Brunton, S. L., and Kutz, J. N., 2019, *Data-Driven Science and Engineering: Machine Learning, Dynamical Systems, An*, Cambridge University Press.
- [104] Büchi, R., and Kottmann, M., 2010, “State Regulator with Observer” [Online]. Available: https://www.researchgate.net/profile/Mohamed_Mourad_Lafifi/post/initial_condition_for_observer/attachment/5dd92817cfe4a777d4f3b1fa/AS%3A828380303851520%401574512663125/download/State+Regulator+with+Observer.pdf. [Accessed: 02-Oct-2021].
- [105] Levis, A. H., Schlueter, R. A., and Athans, M., 1971, “On the Behaviour of Optimal Linear Sampled-Data Regulators!,” *Int. J. Control*, **13**(2), pp. 343–361.
- [106] Kalman, R. E., Ho, Y. C., and Narendra, K. S., 1963, *Contributions to Differential Equations. Vol. 1.*, New York Interscience Publishers.
- [107] Chen, T., and Francis, B. A., 1995, *Optimal Sampled-Data Control Systems*, Springer London, London.
- [108] Ackermann, J., 1985, *Sampled-Data Control Systems*, Springer Berlin Heidelberg, Berlin, Heidelberg.
- [109] Takács, G., Polóni, T., and Rohal’-Ilkiv, B., 2014, “Adaptive Model Predictive Vibration Control of a Cantilever Beam with Real-Time Parameter Estimation,” *Shock Vib.*, **2014**, pp. 1–15.
- [110] Mayne, D. Q., Rawlings, J. B., Rao, C. V., and Scokaert, P. O. M., 2000, “Constrained Model Predictive Control: Stability and Optimality,” *Automatica*, **36**(6), pp. 789–814.
- [111] Scokaert, P. O. M., and Rawlings, J. B., 1996, “Infinite Horizon Linear Quadratic Control with Constraints,” *IFAC Proc. Vol.*, **29**(1), pp. 5905–5910.
- [112] Rossiter, J. A., 2017, *Model-Based Predictive Control*, CRC Press.

- [113] Tehrani, M. G., and Mottershead, J. E., 2012, *An Overview of the Receptance Method in Active Vibration Control*, IFAC.
- [114] Mottershead, J. E., Tehrani, M. G., James, S., and Ram, Y. M., 2008, “Active Vibration Suppression by Pole-Zero Placement Using Measured Receptances,” *J. Sound Vib.*, **311**(3–5), pp. 1391–1408.
- [115] Li, Z., Zhang, D., Shao, L., and Han, S., 2019, “Experimental Investigation Using Vibration Testing Method to Optimize Feed Parameters of Color Mixing Nozzle for Fused Deposition Modeling Color 3D Printer,” *Adv. Mech. Eng.*, **11**(12), pp. 1–12.
- [116] Milana, G., Banisoleiman, K., and González, A., 2021, “An Investigation into the Moving Load Problem for the Lifting Boom of a Ship Unloader,” *Eng. Struct.*, **234**(June 2020).
- [117] Silvestre, J., Donadon, V., Silva, G. C., Santos, O. S., Silva, R. G. A., Versiani, T. D. S. S., Gonzalez, P. J., and Bertolin, R. M., 2018, “Active and Passive Control for Acceleration Reduction of an Aeroelastic Typical Wing Section.”
- [118] Jiffri, S., Fichera, S., and Mottershead, J. E., “Experimental Nonlinear Control for Flutter Suppression in a Nonlinear Aeroelastic System.”
- [119] Mokrani, B., Palazzo, F., Mottershead, J. E., and Fichera, S., 2019, “Multiple-Input Multiple-Output Experimental Aeroelastic Control Using a Receptance-Based Method,” *AIAA J.*, **57**(7), pp. 3066–3077.
- [120] Hansen, C., 2014, “Aeroelastic Load Simulation of a 3 MW Two Bladed Wind Turbine,” Hochschule für Angewandte Wissenschaften Hamburg.